CRANFIELD UNIVERSITY

Robert Sawko

Mathematical and Computational Methods of non-Newtonian, Multiphase Flows

School of Engineering

PhD Thesis

Academic year 2011/2012

Supervisor:
Prof. Chris Thompson

In partial fulfillment of the requirements for the degree of
Philosophiae Doctor (PhD)

Abstract

The research presented in this thesis is concerned with the development of numerical techniques and mathematical models for non-Newtonian fluids and two-phase flows in pipes and channels.

Single phase, turbulent flow calculations of non-Newtonian fluids were performed initially. Based on the literature a revised approach to wall modelling is proposed and implemented. The approach uses analytical and experimental analyses of the turbulent boundary layer structure. A comparison with the standard approach is presented.

The interaction between turbulence and non-Newtonian behaviour is studied by examining the rate of strain induced by fluctuating components of velocity. The statistical analysis of published DNS data is performed. Finally, a model is proposed where the turbulent rate of strain is determined from turbulence quantities used by the Reynolds-averaged Navier–Stokes model and used in the calculation of molecular viscosity.

For two-phase flow, the solution procedure using periodic boundary conditions was developed under an assumption of a flat interface. The numerical technique was verified by comparing to an analytical result obtained for laminar flow in a channel. An extension to three dimensional flow is performed.

With periodic boundary conditions standard turbulence models are applied to two-phase stratified flow. Several models and their corrections for two-phase flow are assessed and a new model is proposed. The numerical studies were carried out primiarily in the open-source code OpenFOAM, but initial attempts were made in commercial packages such as STAR-CD and FLUENT. Experimental data collected from the literature are used to verify the results showing good agreement in pressure drops and phase fractions.

Acknowledgements

It is a pleasant duty to express gratitude to all those who have contributed to the completion of the presented work. I would like to acknowledge the work of my supervisor Professor Chris Thompson who offered many stimulating discussions and introduced me to this fascinating field. It is also my privilege to acknowledge Professor Ray Chhabra, Doctor Fernando Pinho, Doctor Robert Poole and Doctor Murray Rudman for supplying me with experimental data and for many comments. Many thanks to Doctor Dag Biberg for providing his own code, consultancy and many useful hints and to Doctor Mustapha Gourma for his critical remarks. I am also immensely grateful to Sarah Jones for offering an engineering perspective in numerous discussions and for invaluable assistance in language matters. Last, but definitely not least I would like to thank my closest family for their constant support.

Contents

List of Figures

LIST OF FIGURES

List of Tables

List of Symbols

Abbreviations

CFD Computational fluid dynamics

CICSAM Compressive interface capturing scheme for arbitrary meshes

DNS Direct numerical simulations

FDM Finite difference method

FEM Finite element method

FVM Finite volume method

GNF Generalised Newtonian fluids

HRIC High resolution interface capturing

LES Large eddy simulation

NVD Normalised value diagram

PCG Preconditioned conjugate gradient

PDF Probability density function

PISO Pressure-implicit split-operators method

RANS Reynolds-averaged Navier–Stokes

SIMPLE Semi-implicit method for pressure-linked equations

STACS Switching technique for advection and capturing of surfaces

URF Under-relaxation factor

VOF Volume of fluid

Greek Symbols

ϵ Turbulence dissipation [m^2/s^3]

Γ Scalar diffusivity coefficient

μ Molecular viscosity [Pa s]

μ_t Eddy viscosity [Pa s]

ν Kinematic viscosity [m^2/s]

ν_t Eddy kinematic viscosity [m^2/s]

ω Specific dissipation [s^{-1}]

ϕ Scalar quantity

ρ Denisty [kg^2/m^3]

τ_i Interface shear stress [Pa]

τ_w Wall shear stress [Pa]

ε_{ijk} Levi-Civita symbol

ζ_i Vorticity component [1/s]

Roman Symbols

S_{ij} Mean rate of strain [1/s]

s_{ij} Fluctuating rate of strain [1/s]

$\hat{s}_{ij}$ Instantaneous rate of strain [1/s]

U_{sg} Superficial gas velocity [m/s]

U_{sl} Superficial liquid velocity [m/s]

$\mathbf{d}$	Distance between centres of two cells
$\mathbf{S}$	Surface area vector
$\mathbf{x}$	Spatial position vector
a_{ij}	Matrix coefficient
R	Source term or in the context of the Biberg model the ratio of shear stresses
S_ϕ	Source term
U_i	the i'th coordinate of the velocity vector $\mathbf{U}$. In the context of turbulent flow the symbol denotes mean velocity.
u_i	the i'th coordinate of the fluctuating component of velocity m/s
V	Volume
x_i	the i'th coordinate of the position vector $\mathbf{x}$

Subscripts

$\mathbf{Q}_f$	$\mathbf{Q}$ at a face
$\mathbf{Q}_N$	$\mathbf{Q}$ of a neighbouring cell
$\mathbf{Q}_P$	$\mathbf{Q}$ of a cell

Chapter 1

Introduction

With the progress of science and technology, the study of flows with more than one phase receives increasing attention among practitioners. Currently, there are many branches of industry where multi-component flows are commonplace. The natural world also abounds in phenomena that are inherently multiphase giving an incentive and opportunities to study multiphase fluid dynamics. Equipment such as coolant systems, long pipelines and separators interact with at least two component flow. The optimal design, maintenance and control of these devices require a better understanding of the complex flow phenomena that are involved. Therefore, the development of current predictive techniques must include the modelling of multiple phases and the interactions that occur between them.

Experimental studies and the resulting empirical correlations are still the most common approaches in investigations of multiphase flows and the design processes. In some cases these techniques proved to be successful but in general multiphase flows encompass many complex mechanisms of mass, momentum and heat transfer that take place inside and between phases e.g. turbulence, surface tension, buoyancy. This, in turn, gives rise to many non-dimensional numbers parameterising the flow and the lack of universally established scaling laws makes it difficult to design efficient and meaningful experiments. An additional difficulty is intrusiveness of most measurement devices. The empirical correlations that come from these experiments are usually of limited applicability.

Moreover, empirical correlations are usually of a global character whereas fluid flows often exhibit transient or local phenomena that can significantly affect the bulk quantities. The local distribution of volume phase fractions can lead to many different flow

regimes such as dispersed flows, stratified flows or slug flows. All of these regimes will have their own distinguishing features. Also, separation or inversion of phases might occur within the time frame of interest. Separation is often induced by design in process engineering in order to isolate the components of the flow that are later subject to further processing. Phase inversion is a phenomenon when the dispersed phase becomes continuous and vice versa. This effect occurs at high dispersed phase volume fractions and is known to produce high effective viscosity in the bulk fluid. None of the current methodologies is able to predict accurately this onset of inversion over a wide range of conditions.

This behaviour of the bulk quantities such as effective viscosity resembles the behaviour of non-Newtonian fluids. These are fluids which exhibit a non-linear relation between stress and the rate of deformation. Originally, they were studied in single phase flows with small polymer additives, but the term may also apply to multi-component flows such as crude oils or emulsions. This has to be viewed as a modelling assumption that allows us to look at two phases as a single phase but with a non-trivial stress-to-strain relation. Employing this approach can lead to enhanced, experiment-based correlations for multiphase flow, but suffers from the same deficiencies as outlined above.

Computational fluid dynamics (CFD) is an alternative technique which uses computer simulations in the study of fluid flows. It is a very versatile tool and with the progress of computational methods as well as the development of hardware and associated software it is becoming ubiquitous in many branches of science and industry. CFD can address local and transient phenomena and thereby overcomes some of the difficulties addressed above. Still, it often requires a significant amount of computational resources and modelling assumptions about the underlying physics. The latter may become advantageous in some cases since it simplifies the flow case but still retains the transient and local information that is the key output of CFD. This is why combining non-Newtonian and two-phase flow modelling may lead to models that improve accuracy while remaining computationally feasible.

This introduction is divided as follows. In Section 1.1 a general overview of CFD and modelling in CFD is given. An emphasis is put on turbulence modelling and the level of detail. Next, in Section 1.2 a historical perspective on the study of non-Newtonian flow is given. Section 1.3 describes the most important multiphase governing equation formulations. In Section 1.4 some example applications are listed. Sections 1.5 and 1.6

give the initial objectives and the contributions of this study. Section 1.7 serves as an outline for the remaining part of this thesis.

1.1 Modelling in computational fluid dynamics

CFD is an important tool in the study of complex flows. It relies on the numerical solution of the partial differential equations that govern the motion of the fluids. Until recent CFD was mostly applied to single phase flow. This proved surprisingly difficult due to the high computational requirements when dealing with turbulent flow. Nevertheless, the progress in numerical techniques, modelling and computer hardware allowed the incorporation of CFD as an industry standard in the development of many products. Multiphase CFD attempts to build on this success by extending the current techniques.

Many challenges have to be overcome. Firstly, there is still much uncertainty in the formulation of the governing equations that capture the essential physics of the flow in question. Currently there is no universal approach and different multiphase flows will require a different set of equations. Furthermore the equations might pose additional numerical difficulties such as in stability or excessive numerical diffusion.

Single phase CFD encountered significant problems when dealing with turbulence. The source of these problems is the energy cascade that can be described as large scale motions giving rise to small scale motions. The small scale motion in turn affect the large scale structures, giving rise to a multi-scale phenomenon. The computational resources required to capture this energy cascade grow rapidly with the Reynolds number of the flow.

Direct numerical simulation (DNS) addresses the problem by resolving all the motions that contribute to the energy spectrum of the fluid. This approach requires the implementation of high accuracy numerical schemes leading also to high computational effort. For scientific purposes DNS is a preferred method if it can be applied since it is equivalent to experimental data but it benefits from the non-intrusiveness of the measurement technique. For engineering applications the results are usually not directly applicable and additional post-processing is required in order to obtain bulk quantities or quantities averaged over time.

On the other end of the spectrum we have the Reynolds-averaged Navier–Stokes (RANS) equations framework. This approach expresses the governing equations in terms of first and second order statistical quantities i.e. mean flow and variance (second central moment). The results from this approach must be understood as an ensemble average of a collection of experiments. In practice, since the whole turbulent energy spectrum is modelled, the modelling assumptions might give a completely distorted picture of the flow. Nevertheless, this approach usually produces results that are directly applicable for engineering purposes and in comparison with other approaches it has the lowest computational requirements. It became a standard in industrial applications where large or complex geometries are involved.

Large eddy simulation (LES) tries to combine the best of both worlds by only modelling a portion of the energy spectrum (usually $\leq 20\%$). This makes the various statistical assumptions more applicable since it is known that turbulent structures at small scales are independent of the large scale motions and exhibit properties like isotropy or homogeneity. Despite the progress in LES, these calculations still require significant computational times and common models of turbulence have to be altered when inter-phase effects become important.

1.2 Non-Newtonian flows

Chhabra (2006) discerns three stages in the development of fluid mechanics. At the first stage, studies were focused on ideal fluids i.e. fluids without viscosity, compressibility, elasticity and with all the remaining material properties kept constant. Those kind of fluids are purely imaginary concepts[1] and were used mainly for the purpose of analysis. Despite the seemingly crude approximations, inviscid and incompressible theories led to ground-breaking results in many areas of science and engineering (e.g. accurate prediction of lift force, which paradoxically is a viscous effect).

The next step was to introduce viscous effects. This was pioneered by Ludwig Prandtl who assumed that viscosity becomes important only in the boundary layer, formed in the direct vicinity of a solid surface. Hence, the flow domain was decomposed into region of ideal fluid (far from the surface) and a viscous fluid (close to the surface). This approach is the basis for classical fluid dynamics.

[1] Except for some unusual situations like superfluidity.

Finally, the third stage, which is still an active area of research, addresses the departure from Newton's linear law of viscosity. Its importance was appreciated at the beginning of the last century as many industrial materials could not be accurately described with this simple relation. Two sources of non-Newtonian behaviour can be distinguished. On a microscopic level, it is the molecular structure of fluid particles. Spherical and roughly spherical particles produce a Newtonian behaviour whilst the addition of long chains of particles might cause Newton's approximation to become invalid. On a macroscopic level, mixtures such as emulsions or slurries may become Non-Newtonian despite the fact that the components are Newtonian. The discipline which deals with flow of matter is called rheology.

Doraiswamy (2002) gave a very precise date for the foundation of the science of rheology as the 29 April 1929, which is the date of the Third Plasticity Symposium and the formation of the first permanent organisation keeping watch over the emerging discipline. Among the participants of the Society of Rheology we can mention Eugene Bingham, Winslow Herschel, Wolfgang Ostwald, Markus Reiner and Ludwig Prandtl. Doraiswamy (2002) also reviews the roots of fluid dynamics and surveys with regard to rheology to eventually present modern issues in this discipline. According to this survey problems of elastic solids were studied in the 17th century by Hooke, Young and Cauchy. The empirical law of viscosity was given by Newton in 1687 but it took almost two centuries to incorporate viscosity in to the governing equations by Claude-Louis Navier and George Gabriel Stokes. The conjunction of the two empirical laws of viscosity and elasticity led in mid 19th century to linear viscoelasticity and a Maxwell model. In the 20th century Arthur Metzner was one of the first to introduce generalized Newtonian fluids in industrial applications on a wide scale and popularised these concepts outside of scientific society.

A more mathematical view of non-Newtonian fluids is due to James Oldroyd who introduced convected derivatives and constitutive law admissibility conditions. This allowed a more qualitative understanding of fluid behaviour although it was at the expense of quantitative accuracy.

Toms (1949) description of drag reduction in polymers has been a source of increased interest in non-Newtonian turbulence. To this day it is still an area of active research including experimental studies, DNS and modelling of these fluids.

1.3 Computational multiphase fluid dynamics

Multiphase computational fluid dynamics deals with the formulation and solutions of fluid flow equations where the flow under investigation has more than one component. Three models have gained particular recognition and are commonly used in academic and industrial applications: volume of fluid (VOF), Eulerian–Lagrangian and Eulerian–Eulerian formulations. All of these models possess different benefits and limitations making them applicable to different, usually exclusive, flow regimes. All of these approaches take the Eulerian approach as its base i.e. they solve the governing equations on fixed control volumes.

VOF, also known as the "one fluid" method, comprises one set of momentum equations, the continuity equation and a scalar transport equation that represents the distribution of the second phase. The material constants are calculated using weighted averages of the components. This approach works when there is clear separation between phases e.g. in stratified flows or for bubbles that are much larger than the mesh size.

The Eulerian–Lagrangian (EL) approach distinguishes between the carrier and the dispersed phases. The carrier phase is treated as a continuous medium and its evolution is modelled via a set of momentum equations and continuity equations. These equations contain special source terms that represent the influence of the dispersed phase such as the drag that a particle exerts. The dispersed phase is modelled as a set of discrete particles with specified position and velocity. The velocity is calculated based on the forces acting on a particle. Then the position is advanced and the forces recalculated again using the continuous phase equations. For turbulent dispersions a random walk algorithm may be invoked. If this is the case several trajectories for a given particle are calculated and then averaged over realisations. Phase coupling in EL can be a one-way or a two-way coupling. The latter is usually more accurate than the former but may encounter significant numerical stability problems. Two-way coupling will face similar problems to those encountered in pressure-velocity coupling in single phase CFD. The solution of one set of equations might give a large residual in the second set of equations. Therefore, care must be exercised in the coupled (both sets solve simultaneously) or the segregated (iterative alternating solution) approach.

Finally, the Eulerian–Eulerian (EE) approach uses two sets of momentum equations, continuity and phase fraction equations. Again, various source terms are used to model

phase interactions which can take the form of mass, momentum or energy transfer. EE does not intrinsically assume that the phase is dispersed or continuous but the choice of source terms may limit the scope of applicability to a given flow regime.
Solving additional equations is not the only complication when dealing with multiphase flows. The behaviour of the fluid is related to the pattern of the phase distribution that is dominant at a given time. Many one dimensional computer codes will utilise some modelling expressions that are specific to a given pattern, thereby increasing the accuracy at the expense of applicability. Three dimensional CFD has the potential to address a wider range of flow patterns accurately but might demand more computational resources.
One of the ways to catalogue these patterns are so called flow maps. See Figure 1.2 for an example. The problem with composing such a chart is the dependency on the composition of phases, volume fractions and geometry and inclination of the bounding surface. The validity of a particular flow map is usually confined to specific values of above properties.

1.4 Areas of application

Non-Newtonian and multiphase flow appear often in industrial processes or everyday life phenomena. This study will focus mainly on transportation in horizontal conduits that is typical in the petroleum industry, but other areas of application suggested by Chhabra (2008) may involve:

Biology: animal waste, blood.

Chemistry: pharmaceutical products, polymer melts and solutions.

Engineering: fire fighting foams, viscous coupling unit in four wheel drive.

Food processing: diary products, fruit or vegetable purees, ice creams.

Geo-sciences: drilling muds, magmas, molten lava.

Transportation: waxy crude oil, sewage sludge, coal slurries, drilling muds, mine tailings, mineral suspensions.

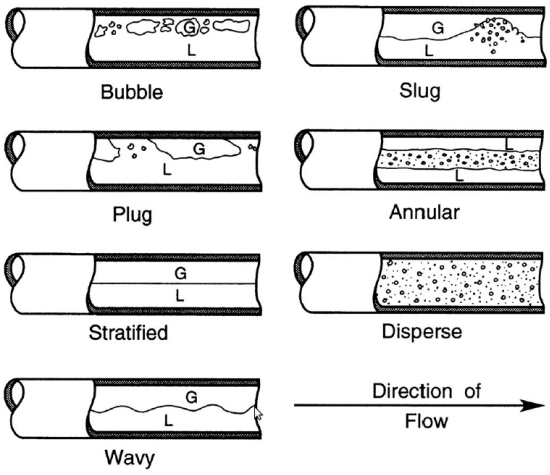

Figure 1.1: Flow patterns in horizontal flows. Picture taken from Brennen (2005)

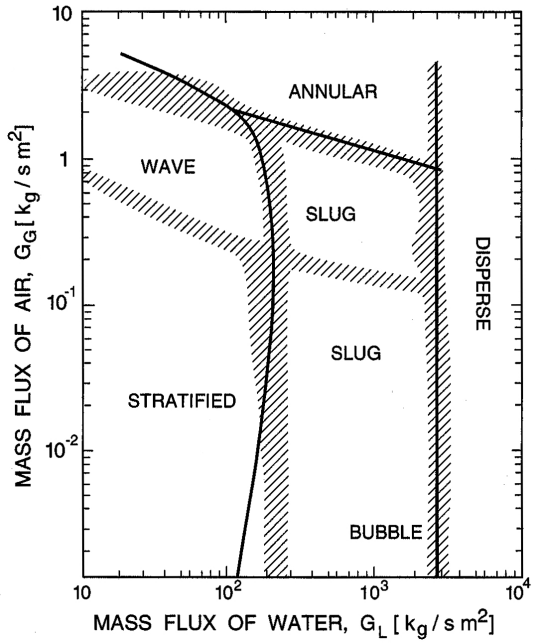

Figure 1.2: Flow map in a horizontal pipe of diameter 5.1cm Picture taken from Brennen (2005)

1.5 Objectives

The main objective of this study was to improve CFD methods for predicting stratified gas/liquid flows in long horizontal conduits. Speed and robustness were the key features that were targeted. Additionally, the models of the flow were to take non-Newtonian properties of the liquid phase into account. Several tasks were identified and studied separately:

1. Modelling of turbulent flow. A RANS approach was employed in order to give directly applicable information quickly.

2. The model must allow the specification of effective viscosity in laminar and turbulent flow of the fluid. In the context of turbulence modelling, turbulent boundary layer modelling is required.

3. Effective methods for solving the equations in large or repetitive domains. Current multidimensional CFD for multiphase flows limits the computational domain size.

4. Modelling of turbulent flow in the vicinity of the gas/liquid interface. Standard RANS methods overpredict turbulent momentum transfer at the interface.

1.6 Presented contributions

1. Non-Newtonian wall functions. Based on the literature review, four different wall functions i.e. the models for turbulent boundary layer behaviour were proposed and assessed. The advantage of using rheology aware wall functions was demonstrated and some of the functions exhibited good predictive capabilities against empirical friction factor curves. The advantage of having an accurate wall functions is decreased demand for computational resources. On the other hand, the solution becomes sensitive to wall mesh refinement since the empirical correlations hold only within a certain range of values.

2. Statistical analysis of non-Newtonian DNS data. The data collected through the literature review and private communication was subject to rigorous statistical analysis in order to test the two hypotheses proposed. The first conjectured that the average rate of strain calculated from the instantaneous velocity is larger

than the rate of strain calculated from the averaged velocity. This statement was not falsified by the data. The second one assumed a form of distribution of the turbulent rate of strain, but this hypothesis was largely disproved.

3. Effective molecular viscosity model for the bulk flow. This represents the effect of turbulence on non-Newtonian rheology in the bulk of the turbulent flow. In the turbulent core region modeled by the RANS equations the effective turbulence viscosity should dominate. A model linking rheological and turbulent quantities is proposed and compared against experimental data.

4. Periodic boundary conditions for two-phase flow. The implementation of periodic boundary conditions is extended to encompass stratified two-phase flow of two incompressible fluids under specified mass fluxes. Two and three-dimensional extensions are given and in case of two-dimensional flow the results are compared against the analytical solution.

5. Models for effective viscosity at the interface of two-phase stratified flow. RANS modelling of stratified flow is compared against experimental data and against other flow models obtained from the literature. Various corrections of turbulence at the interface are subsequently reviewed and assessed. A new method is proposed and tested.

1.7 Outline

The structure of the remaining part of the document and its relation to the objectives listed in Section 1.5 are given in Figure 1.3. Chapter 2 begins the dissertation by explaining the principles of the discretisation with the finite volume method. This is the first chapter because it all the subsequent chapters solve the equations obtained by this method. Chapter 3 describes the VOF method in detail and introduces periodic boundary conditions for multiphase flows. Next, in Chapter 4, non-Newtonian fluids are described and the special wall functions are presented. Chapter 5 focuses on the theoretical formulation of effective viscosity models and contains the statistical analysis of DNS data. CFD simulations using effective viscosity models are also shown there. Modelling of turbulent and laminar flow in the stratified regime is presented in Chapter 6.

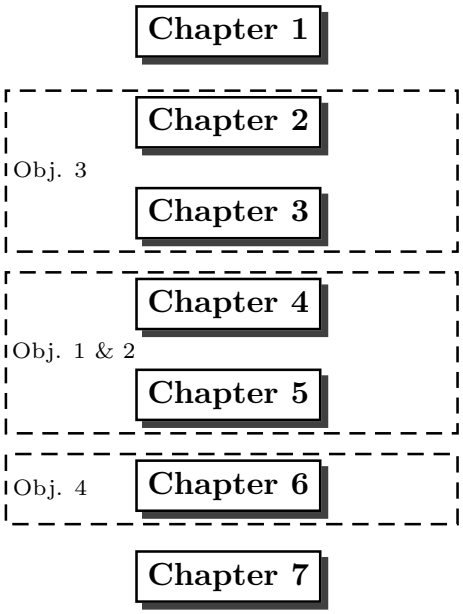

Figure 1.3: The outline of the thesis

Chapters 4 and 5 consider only single phase flows whereas Chapters 3 and 6 consider multiphase flows. This is justified, since periodicity for multiphase is an extension of single phase flow and all of the single phase solutions use this periodicity in order to focus on the behaviour of turbulence models in long conduits.
Finally, the conclusion and the outline of possible extensions to this work are outlined in Chapter 7.

Chapter 2

Finite volume method

Discretisation of partial differential equations allows the transformation of a problem from a continuous to a discrete domain. There are many methods that achieve this goal e.g. finite difference (FDM), finite volume (FVM) or finite element methods (FEM). In general these methods can lead to systems of algebraic equations which give solutions that do not correspond to the original continuous system.

FVM can be seen as a special case of FEM (see Chung (2002)) where the basis function is a linear combination of Dirac deltas and the test functions are indicator functions for each control volume. The test functions do not appear explicitly in the formulation making the method easier to implement in a computer code. Although not as general as FEM, FVM has proven to be reliable and it is in use in many commercial and open-source CFD codes. Its properties and behaviour are often more intuitive and the solutions less diffusive since the quantities are located in a single point within a cell.

There is abundant literature on FVM (Patankar (1980), Ferziger and Perić (2002), Chung (2002), Rusche (2002)) and Toro (2009)). The aim of this chapter is to recall the fundamentals that are required for the exposition of a solver that uses periodic boundary conditions and conserves mass flux constraints. In this chapter the discretisation techniques are covered with particular emphasis on difference schemes used in multiphase calculations.

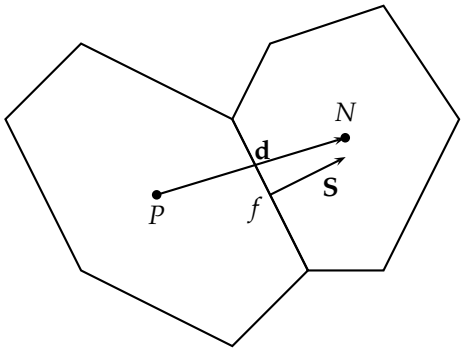

Figure 2.1: Finite volume notation.

2.1 Domain discretisation

The solution of a system of partial differential equations is a function that varies in time and space. We will proceed with a description of the temporal and spatial discretisation of the solution domain.

Time discretisation breaks the time interval into time steps of length Δt. These can have uniform length or vary in a predefined manner, usually according to some simulation parameters. Most of the modern methods will automatically decrease the time step if higher accuracy is required.

The spatial discretisation requires the division of the space into non-overlapping control volumes with adjacent faces. In this study only flat faces will be considered although it is generally possible to accommodate curved faces as well.

A pair of cells is depicted in Figure 2.1. It is common to denote a cell of interest as P, a face as f and a neighbouring cell with common face f as $N(f)$, $\mathbf{S}_f$ as a vector normal to the surface with a magnitude equal to the area of the surface. Since, in general, the shapes of faces and control volumes are arbitrary the definition of face centre $\mathbf{x}_f$ and cell centres $\mathbf{x}_P$ are as follows:

$$\int_S (\mathbf{x} - \mathbf{x}_f)\, \mathrm{d}\mathbf{S} = 0 \tag{2.1}$$

$$\int_{V_P} (\mathbf{x} - \mathbf{x}_P)\, \mathrm{d}V = 0 \tag{2.2}$$

If $\mathbf{d} = \mathbf{x}_N - \mathbf{x}_P$ satisfies $\mathbf{d} \cdot \mathbf{S}_f = |d||S_f|$ then we say that the grid is orthogonal. Otherwise the grid is called non-orthogonal and will require special treatment during a further discretisation process.

Furthermore the grids can be divided into structured and unstructured. Structured grids consist of cuboids i.e. control volumes are quadrilateral polyhedrons isomorphic to a cube. In unstructured grids the only requirements is that the control volume remain convex. When implementing solvers for unstructured girds additional care must be taken to account for connectivity.

There is also a choice of the location where the independent and dependant quantities are calculated. If all the data are estimated at cell centres than such arrangement is called a collocated grid. However, due to some numerical effects, it can be beneficial to store some quantities at the face centres. Such arrangement is called a staggered grid.

2.2 Equations discretisation

After discretising the domain the next step is to discretise the equations describing the phenomenon under study. This procedure transforms continuous differential equations to a system of discrete algebraic equations where the vector of unknowns represents field values in every point in the grid and for each time step. The equations solved in fluid dynamics problems are all based on conservation laws and take the form of a general scalar transport equation:

$$\underbrace{\frac{\partial \rho\phi}{\partial t}}_{\text{Transient term}} + \underbrace{\nabla \cdot (\rho \mathbf{U} \phi)}_{\text{Convective term}} = \underbrace{\nabla \cdot (\Gamma \nabla \phi)}_{\text{Diffusion term}} + \underbrace{S_\phi(\phi)}_{\text{Source term}} ,$$

where ϕ is a scalar, ρ density, $\mathbf{U}$ velocity, Γ diffusion rate and S_ϕ a source term. In FVM the algebraic equations are formed by taking an integral over volume and over time of the above equation. This leads to:

$$\int_t^{t+\Delta t} \left[\int_{V_P} \frac{\partial \rho\phi}{\partial t} \, \mathrm{d}V + \int_{V_P} \nabla \cdot (\rho \mathbf{U} \phi) \, \mathrm{d}V \right] \mathrm{d}t = \int_t^{t+\Delta t} \left[\int_{V_P} \nabla \cdot (\Gamma \nabla \phi) \, \mathrm{d}V + \int_{V_P} S_\phi(\phi) \, \mathrm{d}V \right] \mathrm{d}t. \tag{2.3}$$

The next step is to apply the divergence theorem to turn some of the spatial integrals into surface integrals. If F is a vector field then the divergence theorem states:

$$\int_{V_P} (\nabla \cdot F) \, \mathrm{d}V = \oint_{S_P} F \, \mathrm{d}S, \tag{2.4}$$

where S_P is the surface encompassing the cell containing point P. In a collocated arrangement the appearance of surface integrals and therefore surface values forces us to approximate them from the values at cell centres. The collocated arrangement admits certain oscillating solutions that are unrealistic from the physics point of view and would not appear in the originally continuous system. Techniques to alleviate this problem will be discussed later.

The next subsection will be devoted to face interpolation schemes. Then we will proceed to the discretisation of particular terms that appear in Equation (2.3).

2.2.1 Face interpolation

The choice of a face interpolation method has been an active area of research since the emergence of FVM. There seems to be a frustrating lack of universality and schemes that perform better under one set of circumstances will manifest deficiencies under a different set of conditions. It is perhaps worth mentioning that a simple 1D, advection equation still remains a benchmark problem (see Toro (2009), Leonard (1991)).

If there exist regions where the flow characteristics change sharply (e.g. the interface in stratified flow) the choice of an appropriate interpolation scheme can significantly affect the result. For scalar convection problems the scheme should exhibit the required accuracy whilst minimising numerical diffusivity and satisfying boundedness.

Fields describing real-life phenomena often have to satisfy certain boundedness criteria e.g. temperature in K must be positive, phase indicator function must be between 0 and 1 etc. Certain choice of interpolation may lead to schemes that violate these bounds giving unrealistic solutions. A canonical example is given in Patankar (1980). The choice of central differencing as the discretisation of spatial derivative in heat convection/diffusion problem gives a scheme that admits solutions with values that exceed given bounds.

The central difference scheme corresponds to an interpolation based on piecewise linear functions that connect the values at central points. It takes the form of:

$$\phi_{f,\mathrm{CD}} = f_x \phi_P + (1 - f_x)\phi_N, \tag{2.5}$$

$$f_x = \frac{|x_f - x_N|}{|x_f - x_N| + |x_f - x_P|}. \tag{2.6}$$

This is a second-order accurate scheme, which stems from the fact that we match the second term in the Taylor series. It can be shown that even for simple, 1D, heat transfer this method can give unbounded, unrealistic solutions (see e.g. Patankar (1980)).
To address these difficulties an upwind scheme is often used. It can be formulated as follows:

$$\phi_{f,\mathrm{UD}} = \begin{cases} \phi_P & U \cdot S_f > 0 \\ \phi_N & U \cdot S_f < 0 \end{cases}, \tag{2.7}$$

This scheme is only first-order accurate, is diffusive, but is bounded.
These two extreme approaches show the typical dilemma one faces in the choice of an appropriate scheme: improving some properties usually proves detrimental in other areas. To tackle this, a hybrid method can be proposed by introducing a blending factor.

$$\phi_{f,\mathrm{BD}} = \gamma\phi_{f,\mathrm{UD}} + (1-\gamma)\phi_{f,\mathrm{CD}}, \tag{2.8}$$

where $0 < \gamma < 1$.
Numerical diffusion is especially detrimental in keeping a sharp interface between phases. The problem can be addressed to some extent with increased grid resolution. However in industrial-scale, multiphase, VOF models this can lead to high computational cost. On the other hand, coarser meshes will lead to significant loss of accuracy and therefore the so-called interface capturing schemes became an important component of these simulations.
Some of the first developments in this area were DAS (Donor–acceptor scheme) by Hirt and Nichols (1981), SLIC (Simple line interface capturing) by Noh and Woodward (1976) and PLIC (Piecewise linear interface capturing) by Youngs (1982). More recently, activities involved extension of these ideas into spline fitting, e.g. López et al. (2004), or fitting with least squares method as in Pilliod (2004).
The above methods take the mesh structure into account making them less versatile under changing geometries. Also the computational cost can be prohibitive in large-scale calculations. Three widely recognised schemes, applicable to both structured and unstructured meshes, are (according to Darwish (2010)):

- CICSAM (Compressive interface capturing scheme for arbitrary meshes),
- HRIC (High resolution interface capturing),

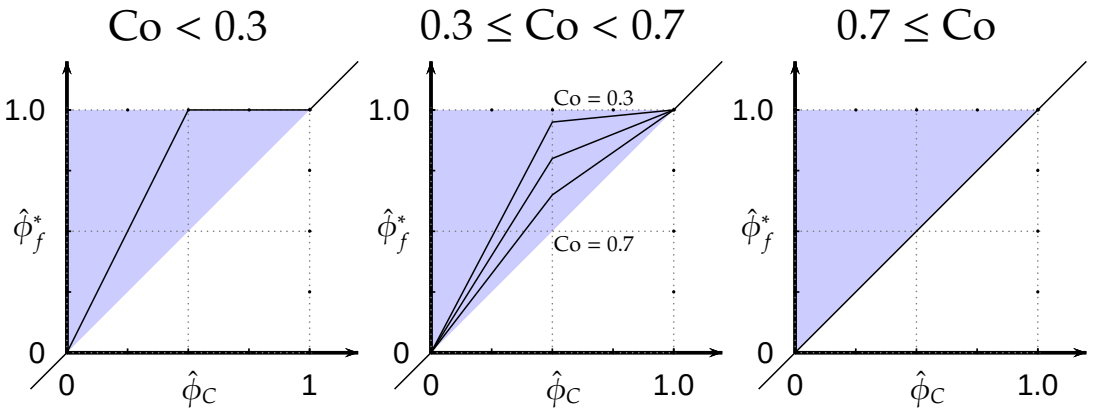

Figure 2.2: Normalised value diagrams for HRIC. The shaded area represents schemes satisfying convective boundedness criteria.

- STACS (Switching technique for advection and capturing of surfaces).

All of these methods can be described using a normalised value diagram (NVD). Here, only the second one will be briefly presented. More detailed descriptions as well as comparative surveys can be found in: Muzaferija et al. (1999); Ozkan et al. (2007); Ubbink and Issa (1999). First the cell value ϕ_C is normalised with respect to upwind ϕ_U and downwind ϕ_D values:

$$\hat{\phi}_C = \frac{\phi_C - \phi_U}{\phi_D - \phi_U}. \tag{2.9}$$

Gaskell and Lau (1988) formulated so-called convective boundedness criteria (CBC) as:

$$\hat{\phi}_f = \hat{\phi}_C \qquad \hat{\phi}_C < 0 \text{ or } 1 \leq \hat{\phi}_C, \tag{2.10}$$

$$\hat{\phi}_C \leq \hat{\phi}_f \leq 1 \qquad 0 \leq \hat{\phi}_C < 1. \tag{2.11}$$

The objective of HRIC is to minimise diffusion while simultaneously satisfying CBC. Next the normalised value at the face is calculated. This procedure can be seen as a hybrid between downwind and upwind:

$$\hat{\phi}_f = \begin{cases} \hat{\phi}_C & \phi_C < 0 \text{ or } \phi_C > 1 \\ 2\hat{\phi}_C & 0 < \phi_C < 0.5 \\ 1 & \hat{0}.5 \leq \phi_C \leq 1 \end{cases}, \tag{2.12}$$

So far the switching between downwind and upwind depends only on spatial distribution of ϕ. It is known that this can produce stability problems and therefore the following correction is introduced to enable switching according to the dynamics of the process (see Figure 2.2):

$$\hat{\phi}_f^* = \begin{cases} \hat{\phi}_f & \text{Co} < 0.3 \\ \hat{\phi}_C + \frac{0.7-\text{Co}}{0.7-0.3}\left(\hat{\phi}_f - \hat{\phi}_C\right) & 0.3 \leq \text{Co} < 0.7 \\ \hat{\phi}_C & 0.7 \leq \text{Co} \end{cases}, \tag{2.13}$$

here $\text{Co} = \frac{\mathbf{U}\cdot\mathbf{S}_f}{\mathbf{d}\cdot\mathbf{S}_f}\Delta t$ is a local Courant number. Since a downwind scheme can cause alignment of the interface with the mesh there is need of a correction that takes the grid alignment into account. This is performed in the following way:

$$\cos(\theta) = \frac{\nabla\phi \cdot \mathbf{d}}{|\nabla\phi||\mathbf{d}|}, \tag{2.14}$$

$$\hat{\phi}_f^{**} = \hat{\phi}_f^* \sqrt{\cos(\theta)} + \hat{\phi}_C \sqrt{1-\cos(\theta)}. \tag{2.15}$$

θ is simply the angle between the grid alignment and the normal to the interface. Eventually the scheme is just a blending between downwind and upwind schemes.

$$\gamma = \frac{(1-\phi_f^{**})(\phi_D - \phi_U)}{\phi_D - \phi_C} \tag{2.16}$$

$$\phi_f = \gamma\phi_C + (1-\gamma)\phi_D \tag{2.17}$$

Two features that appear in the above description are common to all the interface capturing schemes. They are all a combination of compressive and high resolution schemes, and the blending is a function of the angle between the grid orientation and the interface direction.

Another scheme that was used in this study was developed by Roe (1985) and is called Superbee. Superbee is really a limiter function that can be used together with a class of flux-limited numerical schemes. The idea originates from the piecewise constant approximation (Godunov scheme) that is extended into piecewise linear interpolation i.e. values are assumed to be changing linearly between the nodes. Based on this subgrid scale model an average flux is calculated. The only unknown of this model are the slopes of the linear functions that are used for interpolation. The flux equations are closed using various expressions involving the node values e.g. central difference (Fromm's method), upwind difference (Beam–Warming method) or downwind difference (Lax–Wendroff method).

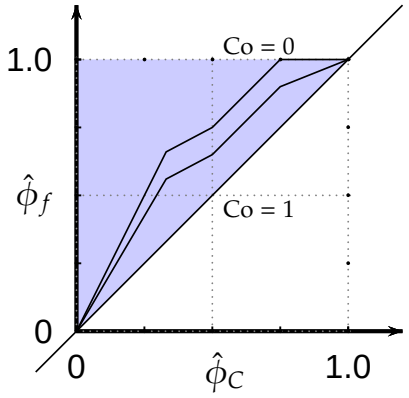

Figure 2.3: The NVD diagram for Superbee scheme.

The piecewise linear approximation can, however, introduce unphysical oscillations in the vicinity of a sharp discontinuity and this is where flux-limiters are used. The idea of using a flux limiter is to remove these oscillations at discontinuities but retain high accuracy at smoothly varying regions.

To detect the regions in which discontunity might occur a ratio of gradients of the form:

$$r = \frac{\phi_C - \phi_U}{\phi_D - \phi_C} \tag{2.18}$$

is introduced. Based on this ratio a limiting function, denoted here by ϕ_l, can be defined. For Superbee it is given by:

$$\phi_l(r) = \max\left\{0, \min\left\{2r, 1\right\}, \min\left\{r, 2\right\}\right\}. \tag{2.19}$$

Finally the approximation of the value is:

$$\phi_f = \phi_C + \frac{1}{2}\left(1 - \mathrm{Co}\right)\phi_l(r)(\phi_D - \phi_C), \tag{2.20}$$

which is shown on the NVD diagram in Figure 2.3. Superbee is known for being highly compressive and therefore it is useful in the context of preserving the interface discontinuity.

2.2.2 Discretisation of transport equation terms

Now we shall proceed to the discretisation of each term in Equation (2.3). To discretise the time derivative of the form $\frac{\partial \rho\phi}{\partial t}$ a simple backward Euler scheme is used and then integrated over the cell volume:

$$\int_V \frac{\partial \rho\phi}{\partial t} \, \mathrm{d}V = \frac{\rho_P^n \phi_P^n - \rho_P^0 \phi_P^0}{\Delta t} V_P \tag{2.21}$$

where $\phi^n = \phi(t + \Delta t)$ and $\phi^0 = \phi(t)$.

The next term is the convective term which as remarked earlier is first turned into the surface integral:

$$\int_{V_P} \nabla \cdot (\rho \mathbf{U} \phi) \, \mathrm{d}V = \oint_{S_P} (\rho \mathbf{U} \phi) \cdot \, \mathrm{d}\mathbf{S} \approx \sum_f \mathbf{S}_f \cdot (\rho \mathbf{U})_f \phi_f = \sum_f F_f \phi_f, \tag{2.22}$$

where $F_f = \mathbf{S}_f \cdot (\rho \mathbf{U})_f$ is the mass flux and ϕ_f is a face value that can be evaluated in a way described in Section 2.2.1.

Similarly we treat the diffusion term:

$$\int_{V_P} \nabla \cdot (\Gamma \nabla \phi) \, \mathrm{d}V = \oint_{S_P} (\Gamma \nabla \phi)_f \cdot \, \mathrm{d}\mathbf{S} \approx \sum_f \Gamma_f \cdot \nabla_f \phi, \tag{2.23}$$

where the only additional difficulty is the gradient term. On orthogonal meshes, the above approximation is second order accurate, but for non-orthogonal meshes further corrections are required. Since this study uses only orthogonal meshes the issue will not be discussed.

Finally, we arrive at source terms of Equation (2.3). The spatial discretisation proceeds with the linearisation and then integration of these terms:

$$\int_{V_P} S_\phi(\phi) \, \mathrm{d}V \approx \int_{V_P} S_I \phi + S_E \, \mathrm{d}V = S_I V_P \phi_P + S_E V_P. \tag{2.24}$$

Additional care has to be taken in the temporal discretisation. Two options are to use the value of ϕ_P from the current or from the previous step. These two treatments are called respectively implicit and explicit discretisations. Since eventually the discretisation process will lead to a system of algebraic equations it is important to think about the resulting matrix of the system and a vector of coefficients. The general strategy is to increase the diagonal dominance of the corresponding linear equation system and therefore whenever the S_I is negative an implicit treatment is advised. Contrariwise when S_I is positive an explicit formulation is better.

2.3 Boundary conditions

All the control volumes inside the domain are discretised in the same manner. The fluxes are expressed in terms of values of neighbouring cells as described in Section 2.2.1. The problem of estimating fluxes arises only at the boundaries where no neighbouring cells exist and hence an extrapolation is required.
For differential equations three types of boundaries are usually possible:

1. Dirichlet boundary conditions, where the value at the boundary points are specified.

2. Neuman boundary conditions, where the normal gradients at the boundary points are specified.

3. Robin or mixed boundary conditions where a combination of the above boundaries is specified.

4. Periodic boundary conditions.

Now a review of these four primitive boundary types is presented. But it is worth noting that in a multidimensional flow there is a number of possible boundaries reflecting various physical situations *e.g.* free surfaces, far-field boundaries, inlets, outlets, etc. These conditions express the influence of the surrounding that is not captured by the equations defined at interior points. Since this study focuses on internal flows, only the boundaries specific to this class will be reviewed.
In the finite volume approach we seek to evaluate the fluxes at the boundaries of each control volume. We can distinguish two types of fluxes: convective fluxes and diffusive fluxes. The former will usually be prescribed at the inflow boundaries and vanish at impermeable walls. The diffusive fluxes may be specified at a wall where the difference is used to approximate the normal gradient.

Dirichlet A specification of a value ϕ_b is provided at the boundary. This means that the equation for a control volume adjacent to this boundary will have $\phi_f = \phi_b$. If the equation contains a gradient then a an approximation of the following form can be used

$$\mathbf{S} \cdot \nabla_f \phi = |\mathbf{S}| \frac{\phi_b - \phi_P}{|\mathbf{d}_B|}. \tag{2.25}$$

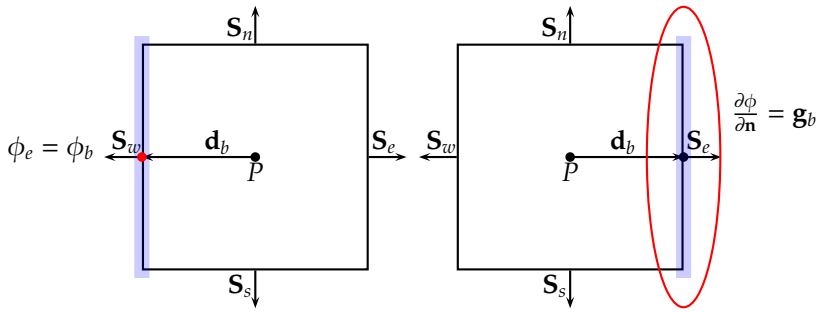

Figure 2.4: Dirichlet and Neuman boundary conditions.

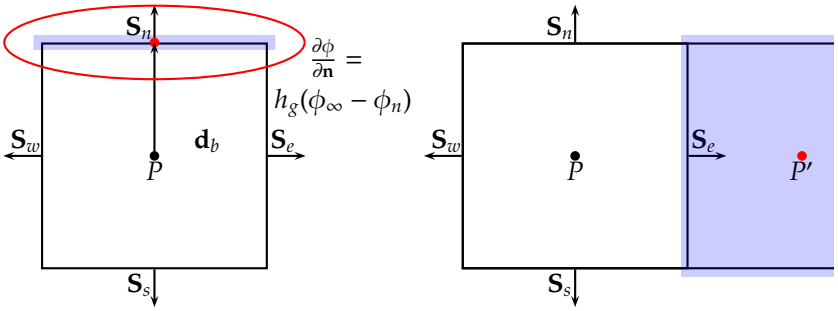

Figure 2.5: Robin and periodic boundary conditions.

Often inlet boundaries are treated this way.

Neuman The fixed gradient at the boundary is known and given as $g_b = \nabla_f \phi$. Now it is the value at the face which is unknown but can be obtained by for example:

$$\phi_f = \phi_P + \mathbf{d}_b \nabla_f \phi = \phi_P + \mathbf{d}_b g_b. \tag{2.26}$$

This treatment is often employed in outlet boundary conditions or at a wall in heat transfer where the normal gradient denotes the prescribed heat flux through the wall (if $g_b = 0$ than an adiabatic wall is obtained).

Robin boundaries fix only the linear combination of the normal gradient and the value. This is often conveniently expressed as:

$$\frac{\partial \phi}{\partial \mathbf{n}} = h(\phi_\infty - \phi_b), \tag{2.27}$$

where h is the diffusion rate at the wall and ϕ_b is the value of the scalar in the environment surrounding the boundary. This can be explicitly expressed through

centroid values after approximating the gradient with a finite difference:

$$\frac{\phi_P - \phi_b}{|\mathbf{d}|} = h_b(\phi_\infty - \phi_b), \tag{2.28}$$

which after rearrangement gives:

$$\phi_b = \frac{\phi_P + |\mathbf{d}|h_b\phi_\infty}{1 + |\mathbf{d}|h_b}, \tag{2.29}$$

that eventually leads to an estimate of the value at the face in the transport equation for the boundary control volume.

This condition determines the medium "impedance" it can be used in heat transfer problems where it models the heat exchange between the environment and the material behind the wall.

Periodic boundaries consist of two sets of faces often referred to as periodic zone and shadow zone. Each face on the periodic boundary requires a specification of the corresponding face in the shadow zone. Then the regions are matched and behave as if they were adjacent. The cells which are adjacent through a periodic zone are considered neighbours adjusting appropriately the fluxes in the control volume transport equation. Essentially, the equations for the boundary cells are now exactly the same as for internal cells.

2.4 The system of linear equations

The final form of the linear equations is obtained by substituting the discretised and linearised terms back into Equation (2.3). The most compact way of expressing the resulting system of linear equations takes the form:

$$a_P\phi_P + \sum_N a_N\phi_N = R_P, \tag{2.30}$$

where a_P, a_Ns are coefficients which depend on the choice of discretisation method. Equation (2.30) expressed in matrix notation is:

$$\mathbf{A}_\phi\phi = \mathbf{R}. \tag{2.31}$$

Matrix $\mathbf{A}_\phi$ contains a_P coefficients on the diagonal and a_N outside of it. ϕ is a vector of unknowns and $\mathbf{R}$ a source vector. This equation can be fed into a linear equation solver.

Now Equation (2.31) has to be solved with respect to ϕ using a viable numerical technique. Linear equation solvers can be broadly split into two groups: iterative and direct methods. The latter ones usually give an exact answer in a finite number of steps however the number of steps usually grows as a cube of the number of unknowns, making the total cost prohibitively high for large scale computations. Iterative methods begin with an initial guess and at each step attempt to improve the solution. Convergence of these methods depends on the form of the matrix and will usually require satisfaction of some additional criteria.

For the estimate of computational resources required to solve Equation (2.31) it is important to note that $\mathbf{A}_\phi$ is usually a sparse matrix *i.e.* only a relatively small subset of coefficients has non-zero values. Choosing a solver that preserves this property will limit memory requirements. It is also important to notice that discretisation errors are usually an order of magnitude higher than the errors coming from the solution of Equation (2.31) and therefore there is no need for a high accuracy solution of the linear equation.

In the discretisation every term treated explicitly will contribute to the source vector R whilst implicit terms might contribute to both A and R (c.f. Subsection Section 2.2.2) A matrix is said to be diagonally dominant if for all P it satisfies $\sum_N |a_N| \leq |a_P|$. For Jacobi and Gauss–Seidel methods diagonal dominance is a sufficient condition for the convergence of the algorithm. Therefore, increasing the diagonal dominance will enhance the performance of the linear solver.

A solver used in this study for symmetric matrices is a preconditioned conjugate gradient (PCG). The original method was proposed by Hestens and Stiefel (1952). It converges in a number of steps less than or equal to the number of equations. The exact number of steps depends on the dispersion of eigenvalues characterised by so called condition number. In general condition number is a property of the problem that measures how much the output values change with small perturbations of input values. If the change is large than the problem is said to be ill-conditioned and if the change is small it is said to be well-conditioned.

For an arbitrary matrix the condition number is the ratio of the highest to the lowest singular value from the matrix singular value decomposition. For real, square matrices this simplifies to the ratio of the maximal eigenvalue to the minimal eigenvalue. Preconditioner is a method of preprocessing of the matrix in order to decrease this

value. The preconditioner used in this study is diagonal incomplete Cholesky (DIC). For asymmetric matrices the solver used was the Preconditioned Bi-Conjugate Gradient (PBiCG) with a Diagonal Incomplete LU (DILU) as a preconditioner.

2.4.1 Under-relaxation

For steady state calculations, which are often undertaken in this study, the time derivative is neglected which significantly decreases the diagonal dominance of matrix A. In the absence of implicit source terms the matrix can be at best diagonally equal making it unsuitable for iterative linear solvers (see Rusche (2002)). To enhance diagonal dominance an artificial term is introduced

$$a_P\phi_P^n + \frac{1-\lambda}{\lambda}a_P\phi_P^n + \sum_N a_N\phi_N = R_P + \frac{1-\lambda}{\lambda}a_P\phi_P^0, \tag{2.32}$$

where $0 < \lambda \leq 1$ is an under-relaxation factor (URF), and ϕ^n,ϕ^0 are the current and the previous iteration values of the solution respectively. If we rewrite this equation to a form:

$$\frac{1}{\lambda}a_P\phi_P^n + \sum_N a_N\phi_N^n = R_P + \frac{1-\lambda}{\lambda}a_P\phi_P^0, \tag{2.33}$$

where it is clear that decreasing λ increase the diagonal dominance of the left hand side. With this modification the simulation is considered converged when ϕ^n approaches ϕ^0.

Chapter 3

Volume of fluid method with periodic boundaries

A single scalar transport equation of the form presented in the previous chapter is insufficient to describe the governing equations of fluid dynamics. The equations derived from the conservation of momentum form a vector transport equation. The first important difference is that the convection term now ties together the values of all vector components creating a coupling between equations. This vector equation is further coupled with a continuity equation through the pressure field. The pressure term in momentum equations can be treated as a source term which leads to a non-conservative formulation or as a surface force which leads to a conservative formulation (see Ferziger and Perić (2002)).

In this chapter we present the standard equations solved by computational methods and then we review the techniques commonly employed to resolve with the pressure-velocity coupling. Then we move to a special treatment of periodic boundary conditions for single phase and multiphase flows. Validation against an analytical result is also presented.

3.1 Governing equations

In the community of multiphase flows, the methodology presented here is called as "one fluid" approach (see Prosperatti and Tryggvason (2006)) since only one set of momentum equations and one continuity equation will be solved. If we are to take account

of the different properties of the fluids it is necessary to account for varying material constants i.e. density, viscosity or thermal properties as well as to add appropriate terms to the momentum equations to account for interfacial phenomena (e.g. surface tension).

For a two-phase flow, the constituent fluids can be identified with an indicator function $H(\mathbf{x})$. We assume that the fluids are immiscible and therefore only one phase can occupy point $\mathbf{x}$ and consequently the indicator will take only two possible values: 1 if area is occupied by the denoted phase and 0 otherwise. For two-phase flow only one indicator is necessary.

If both of the fluids are incompressible the density is given by

$$\rho(\mathbf{x}) = H(\mathbf{x})\rho_1 + (1 - H(\mathbf{x}))\rho_2. \tag{3.1}$$

Similar equations can be derived for other material properties, but it is important to note that the constants appearing in the diffusion terms might be further related to the position of the interface. In these cases the relation between the direction of diffusion and the position of the interface might significantly affect the rates of diffusion.

To account for interfacial effects in the momentum equations it is necessary to localise the interface in the spatial domain. The interface is marked by a non-zero gradient of the indicator function. Therefore we need to calculate the gradient of H. The indicator function can be re-expressed in terms of delta functions as follows:

$$H = \int_A \delta(x_1 - \hat{x}_1)\delta(x_2 - \hat{x}_2)\ \mathrm{d}\hat{\mathbf{x}}, \tag{3.2}$$

where A corresponds to an area occupied by the phase denoted by H. The gradient can be expressed as

$$\begin{aligned}
\nabla H =& \nabla_{\mathbf{x}} \int_A \delta(x_1 - \hat{x}_1)\delta(x_2 - \hat{x}_2)\ \mathrm{d}\hat{\mathbf{x}} \\
=& \int_A \nabla_{\mathbf{x}} \delta(x_1 - \hat{x}_1)\delta(x_2 - \hat{x}_2)\ \mathrm{d}\hat{\mathbf{x}} \\
=& -\int_A \nabla_{\hat{\mathbf{x}}} \delta(x_1 - \hat{x}_1)\delta(x_2 - \hat{x}_2)\ \mathrm{d}\hat{\mathbf{x}} \\
=& -\oint_S \delta(x_1 - \hat{x}_1)\delta(x_2 - \hat{x}_2)\mathbf{n}'\ \mathrm{d}\hat{s}',
\end{aligned} \tag{3.3}$$

where S is the bounding surface of A. The transformation of the variables in the gradient was possible because δ is antisymmetric with the integration of the variable.

Now we introduce a new coordinate system. The first coordinate will be the distance s along the bounding surface. The second coordinate is the length of a vector normal to the surface S. This is denoted by n. With the new coordinate system it is possible to write:

$$\delta(x_1 - \hat{x}_1)\delta(x_2 - \hat{x}_2) = \delta(n)\delta(s). \tag{3.4}$$

And eventually the Heaviside function is expressed:

$$\nabla H = -\oint_S \delta(s')\delta(n')\mathbf{n}\,\mathrm{d}s' = -\delta(n)\mathbf{n}. \tag{3.5}$$

For the sake of brevity the above derivation has been written for two-dimensional flow. A generalisation to three dimensions is possible and will be used subsequently. This allows us to write down the momentum equations

$$\frac{\partial \rho \mathbf{U}}{\partial t} + \nabla \cdot \left(\rho \mathbf{U}\mathbf{U}^{\mathbf{T}}\right) = -\nabla p + \nabla \cdot \boldsymbol{\tau} + \mathbf{g} + \sigma\kappa\delta(n)\mathbf{n}, \tag{3.6}$$

where κ is the curvature of the interface, ρ density, μ viscosity, and σ surface tension coefficient.

The above equations contain discontinuities over the material interfaces and therefore cannot be solved with the FDM. However, the finite volume method can obtain a solution to an equivalent integral form, which admits discontinuous solutions.

In the discretisation process the indicator function will be turned into a scalar field. The corresponding scalar transport equation must be added to the system.

3.1.1 Phase fraction

In the VOF approach the indicator function becomes another scalar field which enters the system of governing equations as an unknown. Let α denote a volume fraction occupied by the first phase within a given control volume. This study adopts the following equation to capture the evolution of the phase distribution:

$$\frac{\partial \alpha}{\partial t} + \nabla \cdot (\alpha \mathbf{U}) + \underbrace{\nabla \cdot (\alpha(1-\alpha)\mathbf{U}_c)}_{\text{interface compression}} = 0, \tag{3.7}$$

where $\mathbf{U}_c$ is an additional velocity field required to compress the interface. This equation differs from an ordinary scalar transport equation (Equation (2.3)). The third term on the left hand side has no physical meaning and it has been artificially added in

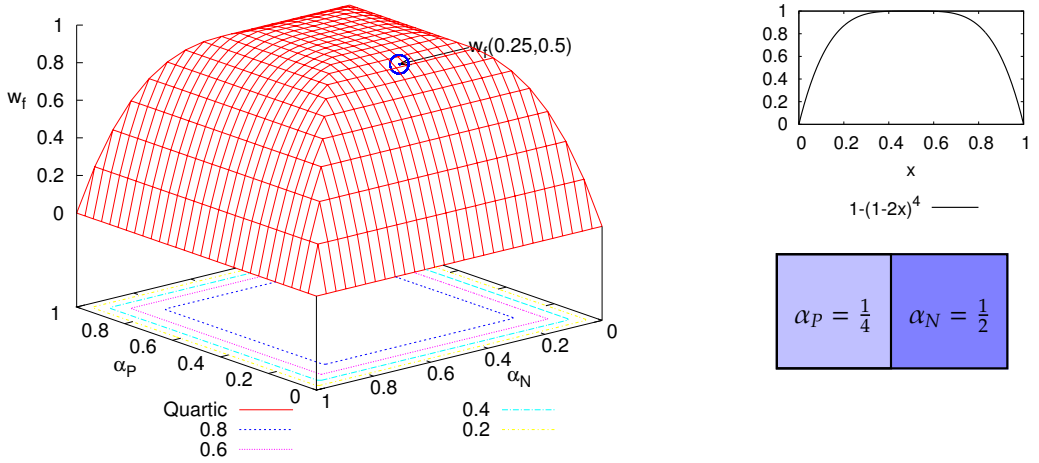

Figure 3.1: Quartic scheme for two neighboring cells and its iso-surfaces.

order to counteract numerical diffusion and keep the interface between phases sharp. Note that the weighting $\alpha(1-\alpha)$ ensures that the whole term is effective only in the region where both phases coexist.

After discretisation with FVM Equation (3.7) will take the form:

$$\frac{\alpha_P - \alpha_P^{\text{old}}}{\Delta t} + \sum_f F_f \alpha_f + \sum_f F_f^c w_f(\alpha) w_f(1-\alpha) = 0, \tag{3.8}$$

where $F = \mathbf{U} \cdot \mathbf{S}$ is the flux surface field and α_f is a face value of α estimated according to a chosen interpolation scheme. F_{cf}, appearing in the third term, is the compressive flux and $w(\cdot)$ is quartic weighting which is described below in greater detail.

The additional flux F^c is designed to keep the interface sharp. The approach adopted in this study, calculates it as a flux equal in magnitude to the original flux, but pointing in the direction of the phase fraction gradient. The flux direction is expressed by:

$$\hat{\mathbf{n}} = \frac{\nabla \alpha}{|\nabla \alpha| + \delta}, \tag{3.9}$$

where δ is the smallest positive number available in a given digital representation, included to prevent numerical instabilities.

$$F_c = |F| \left(\hat{\mathbf{n}} \cdot \frac{\mathbf{S}_f}{|\mathbf{S}_f|} \right). \tag{3.10}$$

The special weighting $w_f(\cdot)$, employed in Equation (3.8), is calculated in the following way:

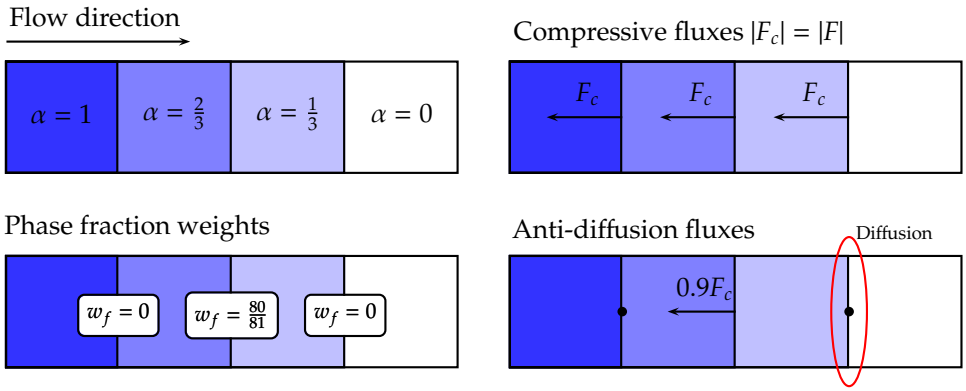

Figure 3.2: Capturing the interface at the front of a displaced phase region. The velocities in each cell are equal and the values of phase fraction were chosen arbitrarily to create a two-cell wide interface. Note the lack of treatment on the first face.

$$w_f^*(\alpha_N, \alpha_P) = 1 - \max\left\{(1-2\alpha_P)^4, (1-2\alpha_N)^4\right\}, \tag{3.11}$$

$$w_f(\alpha_N, \alpha_P) = \begin{cases} 0 & w_f^*(\alpha_N, \alpha_P) < 0 \\ w_f^*(\alpha_N, \alpha_P) & \text{otherwise} \end{cases}. \tag{3.12}$$

The interface compression weighting scheme is based on the quartic scheme and is depicted in Figure 3.1. The values are obtained for each face based on two neighbouring cells. Also, the function in Equation (3.11) is symmetric with respect to a point $(0.5, 0.5)$ and therefore for $0 \leq \alpha \leq 1$

$$w_f(\alpha_N, \alpha_P) = w_f(1-\alpha_N, 1-\alpha_P). \tag{3.13}$$

The interface compression term is inactive if the there are less than two layers of cells with phase fraction between zero and one. For wider interfaces the treatment is not symmetric with respect to the side of the front: the method behaves differently in the case of a phase entering the control volume and for the phase leaving the control volume. The first example is depicted in Figure 3.2. The method is inactive if any of the neighboring cells is 1 or 0. This means that numerical diffusion is counteracted only in the region between transition cells and not in the first cell of the interface.
If the phase is leaving the control volume (see Figure 3.3) then the non-zero compressive flux is positioned between the last cell containing the phase and its upwind neighbour. This time the compressive treatment increases the transport rate of the phase and therefore keeps a sharper gradient at the phase boundary.

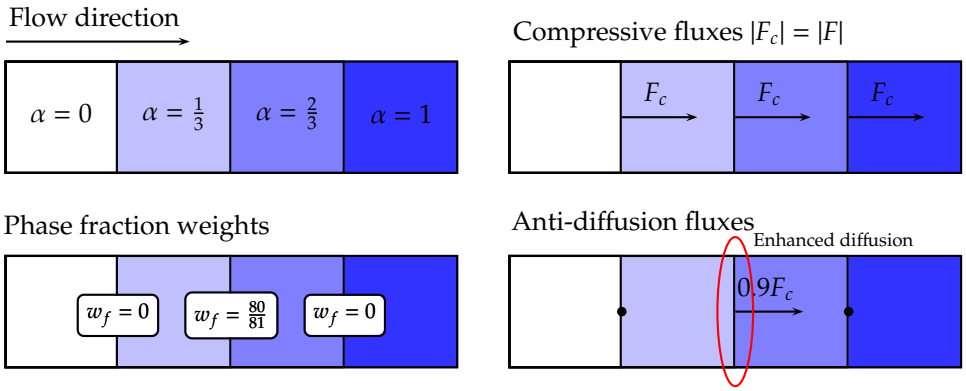

Figure 3.3: Capturing the interface at the back of displaced field. Note the increased diffusion from the last cell. Velocities in each cell are equal and the values of phase fraction were chosen arbitrary to create a two-cell wide interface.

To summarise, in front of the displaced phase a rarefaction wave will be formed, which connects continuously regions of two phases. This effect will decay fairly quickly since subsequent cells will receive an anti-diffusion treatment which hinder an increased scalar spreading. At the back of the bubble the discontinuity will remain sharp due to enhanced diffusion. Simple tests show an exponentially decaying region at the front of a displaced phase and a sharp interface on its back. This result is in contradiction with a weak solution of a Riemann problem for Burgers equation where an exactly opposite picture emerges (i.e. a discontinuity at the front and a rarefaction at the back of the displaced phase).

A comparison between various interpolation schemes of the kind presented in Chapter 2 with the method presented in this section is shown in Figure 3.4. The test is the result of advancing a 1D linear advection equation on a uniformly spaced grid with the Courant number equal to 0.1. This demonstration serves to show that the artificial flux method presented in this section can perform the task of advecting a discontinuity in a similar way to the more established methods.

The definition of a phase fraction indicator, α, allows the calculation of material constants as averages where α takes the role of weighting function:

$$\rho = \alpha\rho_G + (1-\alpha)\rho_L, \qquad \mu = \alpha\mu_G + (1-\alpha)\mu_L \tag{3.14}$$

and similar relationships for thermodynamical properties. Again we point out that in

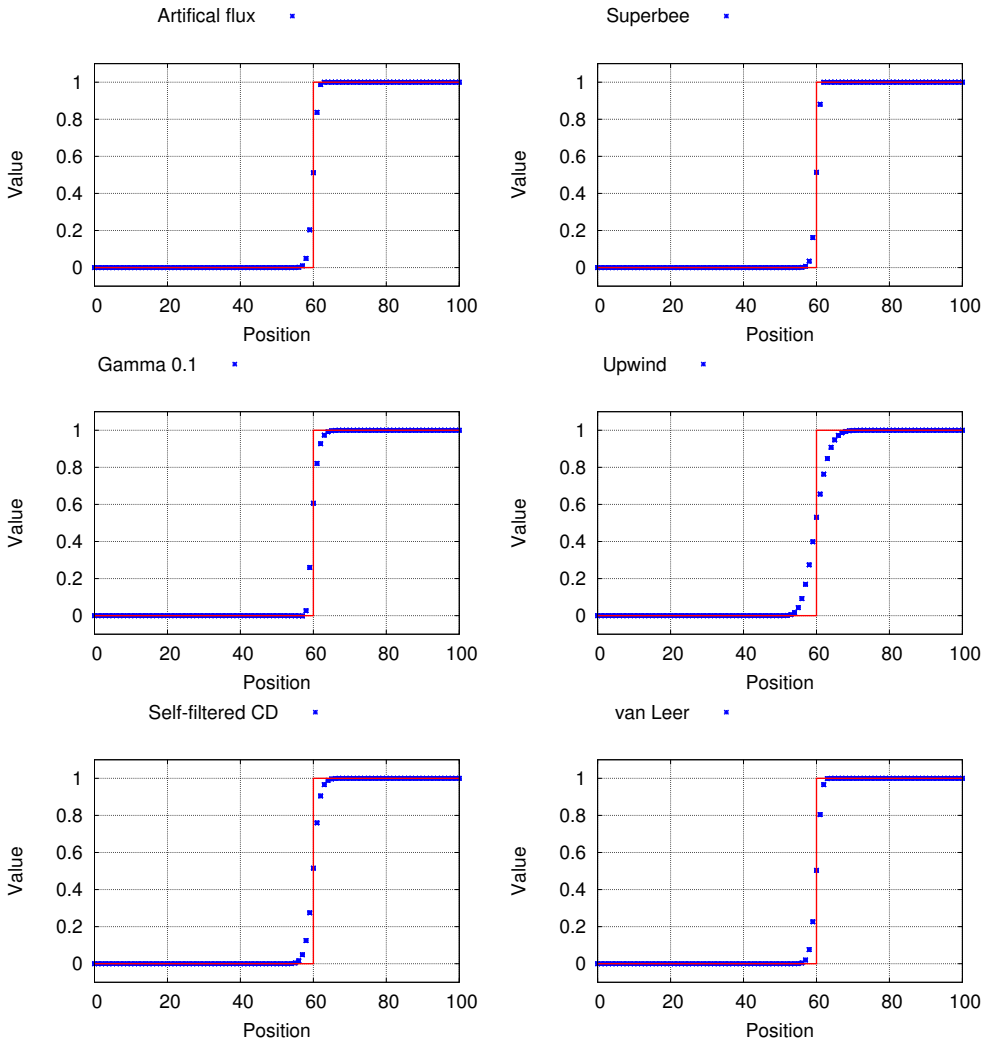

Figure 3.4: The comparison of different interpolation schemes for Riemann problem. Courant number equals to 0.1.

some cases the orientation of the interface with respect to diffusion should be taken into account.

3.1.2 Continuity and momentum Equations

The material properties calculated in the previous stage allow us to obtain coefficients for momentum equations properly accounting for the differences between phases. This leads to a single set of governing equations with varying coefficients which represent averages over control volumes. The equations for a single phase flow with varying coefficients have been derived by many authors (see e.g. Batchelor (1967), Landau and Lifshitz (1987), Anderson (1995), Panton (1996)). The form that is relevant to two-phase flows needs additional terms that model phase interactions e.g. gravity force or surface tension.
To simplify the specification of pressure at the boundary a modified pressure is usually introduced. The equations are then solved with the modified pressure as an independent variable.

$$\hat{p} = p - \rho \mathbf{g} \cdot \mathbf{x}. \tag{3.15}$$

This also eliminates the constant gravity source term that appears on the right hand side of Equation (3.6) since the gradient of pressure is now expressed by:

$$\nabla p = \nabla \hat{p} + \mathbf{g} \cdot \mathbf{x} \nabla \rho + \rho \mathbf{g}. \tag{3.16}$$

To include the effects of surface tension the curvature coefficient κ has to be calculated. In the interface capturing methodology there is no explicit interface and κ has to be extracted from the phase fraction distribution. Using the interface normal vector $\hat{\mathbf{n}}$ obtained in the previous section, the curvature can be obtained as:

$$\kappa = \nabla \cdot \hat{\mathbf{n}}. \tag{3.17}$$

The form of the stress tensor is derived based on the following assumptions. The tensor must be related to the local deformation of the fluid, which can be expressed by velocity gradients. If we assume that the deformations are small, we can postulate that the stress depends only on the first derivative of velocity and the dependency is linear. Also, there can be no terms which are independent of velocity derivatives, since

the tensor has to vanish for a constant velocity field. The most general tensor of rank two satisfying these condition is (see Landau and Lifshitz (1987)):

$$\boldsymbol{\tau} = \mu\left(\nabla\mathbf{U} + (\nabla\mathbf{U})^T - \frac{2}{3}\mathbb{I}\mathrm{tr}\nabla\cdot\mathbf{U}\right) + \zeta\mathbb{I}\mathrm{tr}\nabla\cdot\mathbf{U}, \tag{3.18}$$

where $\mathbb{I}$ is the identity tensor, μ is the shear viscosity and ζ is the extensional viscosity. In incompressible flows the term containing extensional viscosity vanishes and therefore this constant will not be taken into account. In some cases, relevant to multiphase flow it is important to introduce it, e.g. Batchelor (1967) studies the extensional viscosity of bubbly liquids.

With these relations the general equations of momentum transfer are:

$$\begin{aligned}\frac{\partial\rho\mathbf{U}}{\partial t} + \nabla\cdot\left(\rho\mathbf{U}\mathbf{U}^{\mathbf{T}}\right) = -\nabla\hat{p} + \underbrace{\nabla\cdot\mu(\nabla\mathbf{U} + (\nabla\mathbf{U})^T)}_{\text{viscous stresses}} + \\ - \underbrace{\mathbf{g}\cdot\mathbf{x}\nabla\rho}_{\text{gravity}} + \underbrace{\sigma\kappa\nabla\alpha}_{\text{surface tension}},\end{aligned} \tag{3.19}$$

where the stress tensor has been further expanded taking into account that viscosity now varies spatially.

Apart from the conservation of momentum, the overall mass conservation must be satisfied.

$$\frac{\partial\rho}{\partial t} + \nabla\cdot(\rho\mathbf{U}) = 0 \tag{3.20}$$

3.1.3 Turbulence equations

If Equation (3.19) was solved for high Reynolds number flow than a very fine mesh would have to be adopted in order to resolve all the scales of turbulence. This equation would constitute the core of DNS approach. In this study turbulence modelling is adopted and therefore the above equations are derived for averaged velocities. This procedure gives an additional term on the right hand side:

$$\begin{aligned}\frac{\partial\rho\mathbf{U}}{\partial t} + \nabla\cdot\left(\rho\mathbf{U}\mathbf{U}^{\mathbf{T}}\right) = -\nabla\hat{p} + \nabla\cdot\mu(\nabla\mathbf{U} + (\nabla\mathbf{U})^T) + \\ - \mathbf{g}\cdot\mathbf{x}\nabla\rho + \sigma\kappa\nabla\alpha + \underbrace{\nabla\cdot\rho\overline{\mathbf{u}\mathbf{u}}}_{\text{Reynolds stress}},\end{aligned} \tag{3.21}$$

where $\mathbf{U}$ has a meaning of average velocity and there is an additional term which needs to be modelled. The modelling assumption usually adopted is called Boussinesq

eddy viscosity assumption. It expresses the unknown correlations in terms of averaged velocities and turbulent viscosity that is derived from scaling arguments.

$$\rho\overline{\mathbf{uu}} = \mu_t \left(\nabla\mathbf{U} + (\nabla\mathbf{U})^T\right) - \frac{2}{3}\rho\mathbb{I}k, \tag{3.22}$$

Turbulence and turbulence modelling are described in more detail in Chapter 4. Here it is only important to mention that apart from momentum and mass balance equations, a set of scalar transport equations is also solved. As an example a Wilcox (1988) k–ω turbulence model equations are presented here. The two additional quantities and their corresponding transport equations are.

$$\mu_T = \rho\frac{k}{\omega} \tag{3.23}$$

$$\frac{\partial}{\partial x_i}(\rho u_i k) = \mu_T \left(\frac{\partial u_i}{\partial x_j}\right)^2 - \rho C_k k\omega + \frac{\partial}{\partial x_j}\left[(\hat{\mu} + \sigma_k\mu_t)\frac{\partial k}{\partial x_j}\right] \tag{3.24}$$

$$\frac{\partial}{\partial x_i}(\rho u_i \omega) = \mu_T C_{1\omega}\left(\frac{\partial u_i}{\partial x_j}\right)^2 \frac{\omega}{k} - \rho C_{2\omega}\omega^2 + \frac{\partial}{\partial x_j}\left[(\hat{\mu} + \sigma_\omega\mu_t)\frac{\partial \omega}{\partial x_j}\right] \tag{3.25}$$

The constants in the above equations are $C_k = 0.09$, $C_{1\omega} = \frac{5}{9}$, $C_{2\omega} = \frac{3}{40}$, $\sigma_k = \frac{1}{2}$, $\sigma_\omega = \frac{1}{2}$.

3.1.4 Additional constraints

Equations (3.7), (3.21), (3.24) and (3.25) are solved inside every control volume. For the control volumes that do not border with any boundaries the fluxes are expressed using the values in neighbouring cells. For the control volumes on the border of the domain, the fluxes need to be specified. Here, we use no-slip boundary condition for every solid wall i.e. the convective flux over the patch is equal to zero. The diffusive fluxes are approximated using the value of wall velocity.

The velocity inlet and the pressure outlet can be used for inlet/outlet modelling, however, this study focuses on periodic boundary conditions. Neighborhood list of the control volumes adjacent to the inlet now includes the control volumes adjacent to the outlet.

Furthermore a mass flux over the periodic surface is imposed. Because each of the phases is incompressible, this is conveniently expressed through superficial velocities,

which are bulk velocities of a given phase if the phase were to occupy the whole cross-section. If the periodic cross-section is denoted by S, then

$$\frac{1}{|S|}\int_S \alpha \mathbf{U} \cdot \, \mathrm{d}\mathbf{S} = U_{\mathrm{sg}} \qquad \frac{1}{|S|}\int_S (1-\alpha)\mathbf{U} \cdot \, \mathrm{d}\mathbf{S} = U_{\mathrm{sl}} \tag{3.26}$$

where U_{sg} and U_{sl} are known superficial velocities. The imposition of these mass fluxes completes the specification of the problem.

3.2 Pressure-velocity coupling

The governing equations presented in Section 3.1 are a system of coupled, non-linear equations. If the coupling between these equations is weak then an efficient strategy of obtaining a solution is to solve these equations sequentially. In this approach we begin with an initial guess and correct each unknown field assuming that the remaining fields do not change.

In general, the governing equations have to be solved in both time and space. During the calculation various coefficients in these equations might change. Therefore there is a need to distinguish between inner and outer iterations. The solution procedure can be repeated several times taking the previous solution as an initial guess. These repetitions are called inner iterations and the series of inner iterations coupled with a stopping criterion is an outer iteration. For example an inner iterations might be run for a given time step and then every execution of inner iterations leads to an improved solution for a given time step. When the stopping criterion has been met, the equation is advanced in time and another series of inner iterations is performed.

Convergence criteria can be specified in many ways. For transient simulations it is necessary to prescribe the end time of the simulation. For inner iterations of transient calculations or for steady state calculation a relative residual is usually given.

$$R_n < \epsilon R_0, \tag{3.27}$$

where ϵ is a specified number. In this study $\epsilon = 10^{-6}$ is used. Figure 3.5 summarises the above algorithm for the governing equations presented in Section 3.1.

The momentum equations, Equation (3.19), are discretised according with the FVM which leads to the following form

$$\mathbf{A}_{\mathrm{D}}\mathbf{U}^* = \mathbf{A}_{\mathrm{H}} - \nabla \hat{p}^* - \mathbf{g} \cdot \mathbf{x} \nabla \rho + \sigma \kappa \nabla \alpha, \tag{3.28}$$

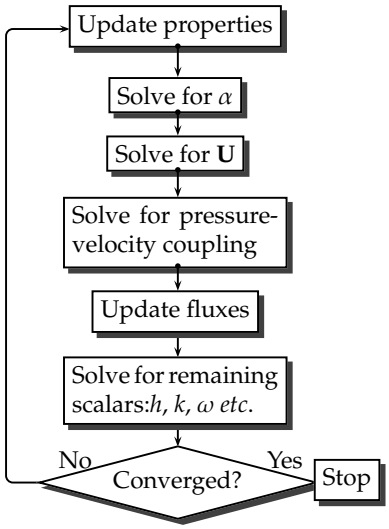

Figure 3.5: The structure of a segregated solver.

where $\mathbf{U}^*$ and $\hat{p}^*$ are vectors of unknowns corresponding to values at cell centres. $\mathbf{A}_\mathrm{D}$ is a matrix of diagonal generated from time derivatives and the implicit source terms. The matrix $\mathbf{A}_\mathrm{H}$ is:

$$\mathbf{A}_\mathrm{H} = \mathbf{A}_\mathrm{R} - \mathbf{A}_\mathrm{N}\mathbf{U}^\mathrm{old} \tag{3.29}$$

where $\mathbf{A}_\mathrm{R}$ is a term derived from the discretisation of the explicit source vector and $\mathbf{A}_\mathrm{N}$ is a matrix of off-diagonal coefficients coming from the convective and viscous terms, $\mathbf{U}^\mathrm{old}$ is a velocity vector from the previous iteration. We can re-express Equation (3.28) as:

$$\mathbf{U}^* = \frac{\mathbf{A}_\mathrm{H}}{\mathbf{A}_\mathrm{D}} - \frac{1}{\mathbf{A}_\mathrm{D}}\nabla\hat{p}^* - \frac{1}{\mathbf{A}_\mathrm{D}}\mathbf{g}\cdot\mathbf{x}\nabla\rho + \frac{1}{\mathbf{A}_\mathrm{D}}\sigma\kappa\nabla\alpha \tag{3.30}$$

since division is well-defined for non-singular, diagonal matrices. Now if we express this in terms of volumetric fluxes for each of the cell bounding surfaces we get:

$$\phi = \phi^\mathrm{old} - \left(\frac{1}{\mathbf{A}_\mathrm{D}}\right)_f |\mathbf{S}|\nabla_f^\perp\hat{p}^* \tag{3.31}$$

where $\mathbf{S}$ is the surface vector and subscript f denotes the quantity interpolated at the surface. ϕ^old is:

$$\phi^\mathrm{old} = \frac{\mathbf{A}_\mathrm{H}}{\mathbf{A}_\mathrm{D}}\cdot\mathbf{S} - \frac{1}{\mathbf{A}_\mathrm{D}}\left(\mathbf{g}\cdot\mathbf{x}\right)_f|\mathbf{S}|\nabla_f^\perp\rho + \frac{1}{\mathbf{A}_\mathrm{D}}\left(\sigma\kappa\right)_f\nabla_f^\perp\alpha. \tag{3.32}$$

Equation (3.31) substituted in the continuity equation gives a Poisson equation:

$$\nabla \cdot \left[\left(\frac{1}{\mathbf{A}_{\mathrm{D}}} \right)_f |\mathbf{S}| \nabla_f^{\perp} \hat{p}^* \right] = \nabla \cdot \phi^{\mathrm{old}}. \tag{3.33}$$

Solving the above equation will give a velocity and pressure field that satisfy the continuity equation but might not satisfy the momentum equation. At this point we execute the next inner iteration by using the new values for velocity and pressure. We continue until convergence is reached.

The above is a classical example of so called projection methods, which projects out the divergence producing part. Other commonly used methods rely on a decomposition of velocity and pressure into a provisional value and a correction required to satisfy the original set of equations. The decomposition is denoted by:

$$\mathbf{U}^* = \mathbf{U}^{\mathrm{old}} + \mathbf{U}', \qquad \hat{p}^* = \hat{p}^{\mathrm{old}} + \hat{p}', \tag{3.34}$$

It is assumed that the equation $\hat{p}^{\mathrm{old}}$ and $\mathbf{U}^{\mathrm{old}}$ satisfy the momentum equation although they do not have to satisfy the continuity equations. Subtracting the momentum equations with the old values from the current iteration values gives:

$$\mathbf{U}' = -\frac{\mathbf{A}_{\mathrm{N}}\mathbf{U}'}{\mathbf{A}_{\mathrm{D}}} - \left(\frac{1}{\mathbf{A}_{\mathrm{D}}} \right) \nabla \hat{p}', \tag{3.35}$$

which ties the correction of velocity to the correction of pressure. By expressing this correction in terms of volumetric fluxes this can be substituted back in the continuity equation:

$$\phi' = (\phi')^{\mathrm{old}} - \left(\frac{1}{\mathbf{A}_{\mathrm{D}}} \right)_f |\mathbf{S}| \nabla_f^{\perp} \hat{p}', \tag{3.36}$$

$$(\phi')^{\mathrm{old}} = -\frac{\mathbf{A}_{\mathrm{N}}\mathbf{U}'}{\mathbf{A}_{\mathrm{D}}} \cdot \mathbf{S}, \tag{3.37}$$

$$\nabla \cdot \left[\left(\frac{1}{\mathbf{A}_{\mathrm{D}}} \right)_f |\mathbf{S}| \nabla_f^{\perp} \hat{p}' \right] = \nabla \cdot \phi^{\mathrm{old}} + \nabla \cdot (\phi')^{\mathrm{old}}, \tag{3.38}$$

which must be implicitly solved for $\hat{p}'$ and $\mathbf{U}'$. Many methods have been proposed based on the treatment of the last term on the right hand side. Two extreme approaches will be presented here.

3.2.1 SIMPLE

In the semi-implicit method for pressure-linked equations the effect of the last term on the right hand side of Equation (3.38) is neglected and the correction of velocity is expressed by:

$$\mathbf{U}' = -\left(\frac{1}{\mathbf{A}_\mathrm{D}}\right)\nabla\hat{p}'. \tag{3.39}$$

There is no formal justification for this step. However, if the method converges, then the values of p' and $\mathbf{U}'$ are small in comparison with $\hat{p}^{\mathrm{old}}$,$\mathbf{U}^{\mathrm{old}}$ and therefore the coupling term will have little effect, vanishing if the exact solution is recovered.
The price paid for this simplification is that the method is known to converge slowly (see Ferziger and Perić (2002)) and often does not converge at all. Under-relaxation factors have to be used to control the convergence rate.

3.2.2 PISO

Pressure-implicit split-operators method performs a series of corrections to velocity and pressure. The first iteration, similarly to SIMPLE, neglects the correction coupling term. However, subsequent iterations use the velocity corrections calculated in the previous stage giving an explicit estimate of the last term in Equation (3.38):

$$\mathbf{U}'' = -\frac{\mathbf{A}_\mathrm{N}\mathbf{U}'}{\mathbf{A}_\mathrm{D}} - \left(\frac{1}{\mathbf{A}_\mathrm{D}}\right)\nabla\hat{p}''. \tag{3.40}$$

Since the velocity field $\mathbf{U}'$ obtained in the previous stage from Equation (3.39) already satisfies continuity conditions now only the velocity of $\mathbf{U}''$ is substituted back to continuity giving:

$$\nabla\cdot\left[\left(\frac{1}{\mathbf{A}_\mathrm{D}}\right)_f|\mathbf{S}|\nabla_f^{\perp}\hat{p}''\right] = \nabla\cdot\left(\phi'\right)^{\mathrm{old}}. \tag{3.41}$$

This procedure can be repeated several times giving many interim estimates of pressure and velocity fields. There is no need to use to the under-relaxation factors in this approach.

3.2.3 Additional discretisation considerations

As mentioned in Chapter 2 collocated grid may introduce solution that do not have a meaningful physical interpretation. This is caused by the fact that after discretisation of pressure term in the momentum equation with simple linear interpolation the central value of pressure for each control volume vanishes.

This leads various spurious solutions e.g. for 1D and 2D are respectively the so called zigzag solution and the checkerboard solution. These solutions use an interchanging pattern of values e.g. for 2D $p_{2i} = 100$ and $p_{2i+1} = 500$ (example from Patankar (1980). Since the central value is not accounted in the control volume discretised momentum equation, pressure will be solved on the twice as coarse grid as every other quantity interchanging values will be perceived by the method as a uniform pressure field. This is sometimes called odd-even decoupling.

In structured grids a remedy to this problem is to adopt the staggered arrangement: pressure is solved for the points in the centre of the control volume whilst velocity is solved for the points that lie on the faces of control volumes. Staggered grid, however, becomes more difficult to implement in complex geometries when unstructured grids need to be used.

Rhie–Chow interpolation alleviates this problem by including such a correction term in convective velocities that the central value of pressure does not vanish from the pressure correction equation and an odd-even decoupling does not take place.

$$a_P U_{iP} + [\nabla p]_P = H_P, \tag{3.42}$$

$$a_N U_{iN} + [\nabla p]_N = H_N, \tag{3.43}$$

where i denotes the direction, a_P, a_N denote corresponding coeffcients in matrix $\mathbf{A}_\mathrm{D}$ and H denotes remaining terms after discretisation. Now we write the same equation for the face value:

$$a_f U_{if} + [\nabla p]_f = H_f. \tag{3.44}$$

Rhie–Chow interpolation assumes that the value for the face can be described as a weighted average of H_N and H_B, which after simple algebraic transformations leads to

$$U_{if} = \overline{U}_{if} + \frac{1}{a_f}\left(\overline{\nabla_i p} - \nabla_i p\right), \tag{3.45}$$

where an overbar denotes the weighted average. The key benefit from this formulation is that the values included in the weighted average come from the centres and the gradients from the centres will use face values which in turn will use the central values again. As a result more values will be used and most importantly the central values will be retained (they will not simplify).

The methods presented in preceding subsections circumvent these difficulties by calculating flux with face values of pressure in Equation (3.31) and then solving for centroid values in Equation (3.33). This can be termed as a correction in the spirit of the Rhie–Chow interpolation since approximation in Equation (3.45) never appears explicitly.

3.3 Periodic boundary conditions

Periodic boundary conditions alter the solution procedure at the level of pressure-velocity coupling. Firstly, observe that the constraint expressed by Equation (3.26) has a global character and involves two independent quantities, namely velocity and phase fraction. This is different from a single phase, incompressible flow case, where velocity was the only independent quantity.

On its own, the multiphase equivalent of the problem will have many solutions. However, if we confine ourselves to stratified flows only, then the we expect the steady state solution to have the liquid at the bottom and gas at the top of the channel. This limits the number of solutions and allows the development of effective procedures.

The assumption of having a heavier phase at the bottom simplifies the goal of calculating the height and the pressure gradient. At each step three quantities will be modified: pressure, velocity and phase fraction. Many approaches have been attempted in this study. Eventually a three step method has been proposed. In the first step we account for continuity using the PISO algorithm to resolve pressure-velocity coupling. This is a standard procedure in segregated solvers. In the second step streamwise pressure gradient and velocity are corrected for gas and liquid separately. This generalises the procedures described in Murthy and Mathur (1997), Patankar and Spalding (1972), Beale (2007). Note, that these correction are performed separately.

The next step compares the pressure gradients in liquid and gas phases and performs a local correction to the phase fraction distribution that moves the interface in the normal direction in such a manner that the streamwise pressure gradients in each phase become

equal. The idea behind the local correction was guided by an attempt to keep the shape of the interface intact. This would allow us to obtain the shape of interface from the solution of VOF equation and then move it in the normal direction to account for constraint of Equation (3.26). The simulation is said to converge when the pressure gradients in both phase are sufficiently close to each other.
This method is applied here for steady state calculations only. However, it is possible to incorporate it as an inner loop of an unsteady simulation. In this case the modification would work only on the periodic patch, whilst the internal control volumes would solve the full unsteady form of the governing equations. The shape of the interface would appear due to modifications caused by gravity and surface tension, whilst its exact position would be calculated using the above procedure.

3.3.1 Notation

Consider the domain of length L, with a periodic patch applied at both ends. This should represent a repeatable segment of the original flow problem. Let $\mathbf{e}$ be a normal to the periodic patch. Then, similarly to Murthy and Mathur (1997), periodicity can be described as follows:

$$\mathbf{U}(\mathbf{x}) = \mathbf{U}(\mathbf{x} + \mathbf{e}L), \tag{3.46}$$

$$\frac{\hat{p}(\mathbf{x} + \mathbf{e}L) - \hat{p}(\mathbf{x})}{L} = \frac{\hat{p}(\mathbf{x} + 2\mathbf{e}L) - \hat{p}(\mathbf{x} + \mathbf{e}L)}{L}. \tag{3.47}$$

As opposed to the velocity field, the pressure field is not strictly periodic, since there is a jump of constant height between the outlet and the inlet of each segment. To perform periodic calculations we must include the jump of pressure at the periodic patch.

$$\hat{p}(\mathbf{x}) = \hat{p}^*(\mathbf{x}) + (\mathbf{x} \cdot \mathbf{e})\beta \tag{3.48}$$

where β will designate a constant, streamwise pressure gradient and $\hat{p}$ will be the periodic pressure field.

3.3.2 Single-phase pressure-correction

Some of the first publications on periodic boundary conditions in three-dimensional flows were those by Patankar and Spalding (1972), Patankar et al. (1977). In the former one the FDM was used to solve continuity, momentum equation and a general

scalar transport equation. To run a 3D calculation with a speed comparable to 2D a Tri-Diagonal Matrix Algorithm in y and z is employed. When sweep in one of the direction is performed the values in the other transverse direction are held constant. In the latter temperature equation is also considered with a special consideration of wall-boundary conditions as the choice of these, alter the form of the resulting periodic equations.

Murthy and Mathur (1997) reports a development of a FVM code on unstructured meshes, generalising the previous results. Using this technique they study triangular ducts, serrated channel and pipe bundles. Application to offset-fin heat exchangers was presented by Beale (2007).

Using periodic boundary conditions Kawamura (1998), Tiselj et al. (2001), Kozuka et al. (2009) performed a series of direct numerical simulations that allow the study of the turbulent heat flux budget, temperature variation, heat dissipation and other statistical quantities related to thermal fields of a turbulent flow.

In a single phase flow only one equation for the mass flux is necessary. In the incompressible case we can use constant volumetric flux or average velocity instead of constant mass flux. The average velocity at a discretised periodic face is given by:

$$\frac{1}{|S|}\sum_f \mathbf{U}_f \cdot \mathbf{S}_f = U_b, \tag{3.49}$$

where U_b is a given bulk velocity that has to be specified as an input to the procedure. We decompose velocity according to Equation (3.34) and reorganise the terms to get the corrections on the left hand side.

$$\frac{1}{|S|}\sum_f (\mathbf{U}'_f) \cdot \mathbf{S}_f = U_b - U_b^{\text{old}}, \tag{3.50}$$

Similarly to pressure, the pressure drop across the periodic patch has to be decomposed into the current value and the correction:

$$\beta = \beta^{\text{old}} + \beta'. \tag{3.51}$$

Now in case of the SIMPLE algorithm we can express the velocity correction in terms of a pressure correction according to Equation (3.39), a discretisation of the gradient and the decomposition of pressure in Equation (3.48) and we obtain:

$$\beta' = -\frac{U_b - U_b^{\text{old}}}{\sum_f d_f^{-1}}, \tag{3.52}$$

where d_f is a diagonal value of matrix $\mathbf{A}_\mathrm{D}$. Ultimately, the calculation using periodic boundaries with a specified mass flux requires us to solve the momentum equations for the points inside the domain and subsequently apply the correction for β which leads to a correction of the values on the boundary of the domain.

3.3.3 Two-phase pressure-correction

As described at the beginning of this section, for two-phase flow we solve two periodic problems separately. First we decompose β in the following way:

$$\beta = \alpha\beta_G + (1-\alpha)\beta_L, \tag{3.53}$$

where β_G and β_L are streamwise pressure drops across the periodic boundary for gas and liquid respectively. This effectively makes β a function dependant on spatial coordinates. Now our task is to calculate the constants β_P, where P=G,L. Again, we can decompose these phase values into the current value and the correction:

$$\beta_P = \beta_P^{\mathrm{old}} + \beta_P^{'}. \tag{3.54}$$

The discretised form of Equation (3.26) is given by:

$$\frac{1}{|S|}\sum_{f\in\mathcal{B}} \alpha_f \mathbf{U}_f \cdot \mathbf{S}_f = U_{sP} \tag{3.55}$$

where $\mathcal{B}$ is the periodic streamwise boundary through which the net mass flux is imposed. Using specified superficial velocities and pressure-velocity coupling we can derive a correction for β_P similarly to Murthy and Mathur (1997):

$$\beta_P^{'} = -\frac{U_{sP} - U_{sP}^{\mathrm{old}}}{\sum_f \alpha_f d_f^{-1}}. \tag{3.56}$$

After correcting the respective β_P the rest of the correction to velocity proceeds in the same manner as in single phase flow.

3.3.4 Liquid height correction

Correction of the velocity completes the second step. Now Equation (3.26) is satisfied but β_L and β_G might differ. The problem we face now is to adjust the phase distribution in such a way that will be closer to equilibrium in the next iteration. The intuitive idea

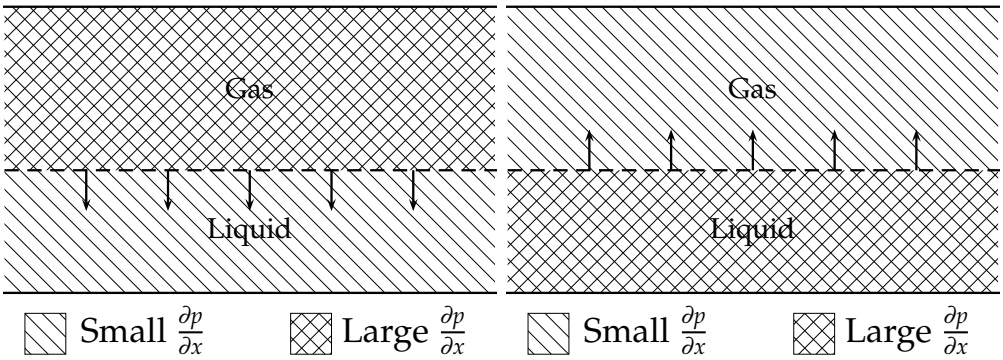

Figure 3.6: Intuitive idea for the phase correction algorithm.

for this scheme is presented in Figure 3.6. If the streamwise gradient is lower on the liquid side than the interface is moved down which increased gas phase width, decreasing the pressure gradient and decreases liquid phase width, increasing the pressure gradient there. If the pressure gradient is lower on the gas side the correction is performed in the opposite direction with an analogous effect.

The realisation of this idea can be performed via the iteration of the advection equation for the values of phase fraction at the patch:

$$\frac{\partial \alpha}{\partial t} + \nabla(U_{\text{corr}}\alpha) = 0 \tag{3.57}$$

where U_{corr} is an artificial velocity that is specified to secure the direction for the correction according to the above logic. Its specification is a part of an algorithm and in this study the following formula proved to be sufficient:

$$U_{\text{corr}} = \frac{(|\beta_G| - |\beta_L|)\upsilon}{\max\{|\beta_L|, |\beta_G|\}}. \tag{3.58}$$

where υ is a constant with the dimension of velocity.

Finally, the procedure is said to converge when the difference between streamwise pressure gradients in both phases is longer small than a given tolerance:

$$|\beta_G - \beta_L| < \epsilon \tag{3.59}$$

This modification is performed only for the cells at the periodic patch. The time step in Equation (3.57) is a fractional time step for unsteady simulation and the number

of iterations is another parameter of the solution procedure. A simple explicit scheme was adopted to solve Equation (3.57) with the Superbee interpolation scheme for the divergence term. Superbee is renowned for its ability to keep discontinuities compressed and was therefore suitable for a task of moving the interface.

3.3.5 Other approaches

The above approach includes artificial flux that acts only as a way to impose mass flux constraints. Provided the method converges, the artificial flux vanishes and therefore the resulting field is a solution to the problem posed at the beginning of this chapter. Since the indicator function is directly translated this may cause smearing of the interface which will deteriorate the quality of the results.

A way to address this problem would be to keep the value of interface height explicitly in the code, modify it at every step of the procedure and then invoke a reinitialisation to keep the interface compressed. This approach has been successfully implemented in the progress of this study in FLUENT and STAR-CD commercial packages, however the results are not presented here, since the method does not generalise easily to three dimensions. In three dimensions concave and convex or irregular interfaces are possible, which would require further parametrization and suitable corrections.

A use of geometrical interface reconstruction could alleviate some of the problems but this approach is not followed here.

A completely different approach would be to formulate the problem where the pressure gradient is known and the mass fluxes are to be calculated. Such approaches have been already presented in the literature for instance Lombardi et al. (1996) or Fulgosi et al. (2003). Specifying the pressure gradient alone leads to a strong dependency on initial solution since the dependency on the distribution of the phase fraction will determine different velocity fields under the same pressure gradient. An otter algorithm could be then implemented which would perform a search for a pressure gradient and an initial phase fraction distribution that satisfy given mass fluxes. Although this procedure is essentially equivalent to the one proposed above, it is argued that in practical terms it will incur a higher computational cost. This is caused by the fact that every time the CFD calculation is executed the initial condition might vary significantly leading to decreased convergence rate or even convergence problems.

3.3.6 Preliminary results

Figure 3.7 show a typical result of a periodic calculation. Phase fraction and velocity field are obtained. It was discovered that incorporating additional layers in the streamwise direction enhanced the stability of the procedure. More results follow in the Chapter 6 where for simpler cases a comparison with analytical solution is presented. For turbulent flows a comparison with experimental data is carried out.

3.4 Concluding remarks

The novel approach to periodic boundary for two-phase calculations is presented here. The solution procedure combines single phase periodicity in such a way as to assure the fluxes over the periodic face remain constant and equal to a specified number. In the following chapter VOF method is used with inlet and outlet boundary conditions. The periodic boundary condition is used only with flat interface assumption. However, there is no contraindication for this procedure to work with VOF, provided that the modification is limited to the cells adjacent to the periodic boundary. The compatibility with VOF method is achieved by defining corrections for phase indicator function.
A simpler version would be to apply periodicity with specified pressure drop across the periodic face, a given initial condition and evolve the state of the system with the governing equations. Unfortunately, this method has no way of preserving the relative mass fluxes and the physical Reynolds number characterising the flow, might change over time. The periodic boundary method presented here is used in the following chapters as a tool for assessing turbulence model and preserving the physical Reynolds number is an important feature.

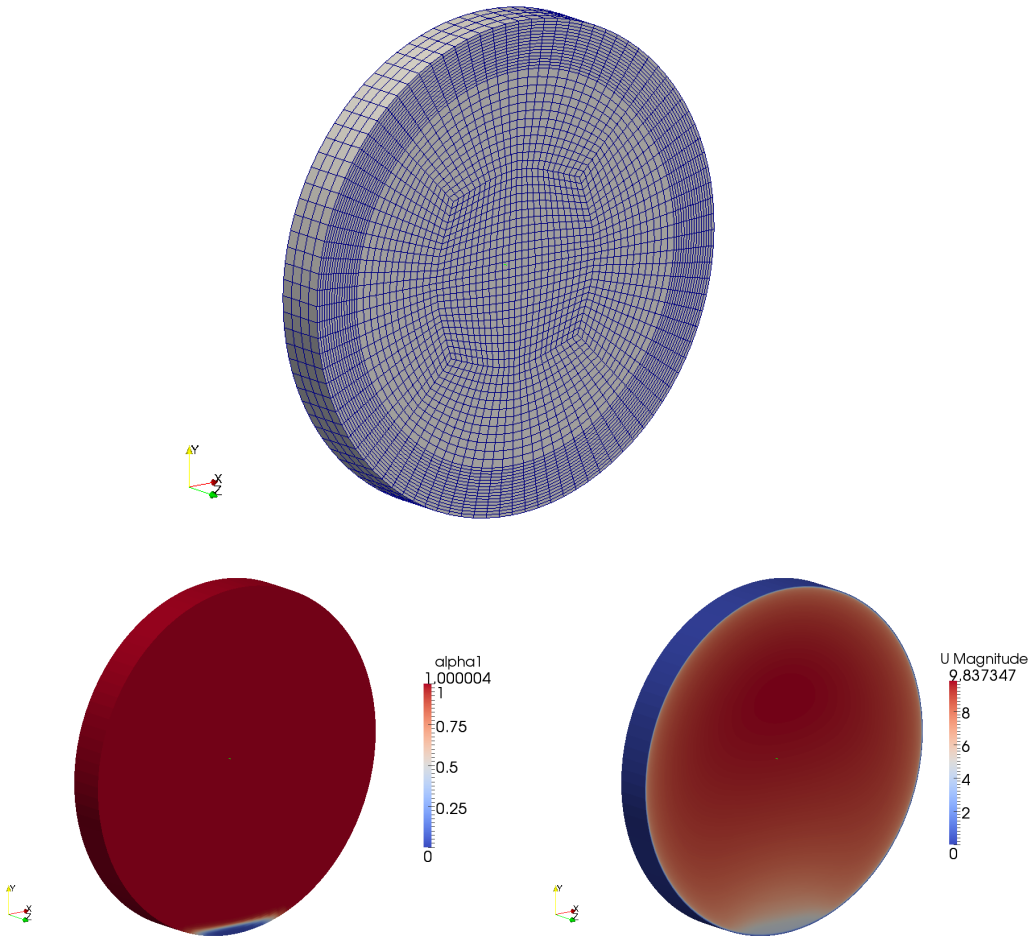

Figure 3.7: Typical results from a 3D periodic simulation of a stratified flow.

Chapter 4

Non-Newtonian properties in turbulence modelling

Despite being more than a hundred years since the pioneering work of Boussinesq and Reynolds on the statistical nature of turbulent flow, turbulence modelling remains a very active area of both science and engineering. The lack of universally applicable models on one side, and numerous applications and the ubiquitousness of turbulence on the other, proved to be extremely motivating factors and led to multiple specialised branches. One of them is turbulent flow of non-Newtonian fluids with turbulent drag reduction in polymeric solutions appearing as an important and distinguishing feature. The chapter begins with recalling one of the main results in the Newtonian case, namely the logarithmic law of the wall and corresponding friction factors that were obtained for channel and pipe flows. These formulae assist engineers in calculating pressure gradients and therefore are useful for pipe design purposes. Then we move to results in rheology that have been pioneered by Dodge and Metzner (1959), who observed a necessity of introducing power-law viscosity equations to describe some fluids of interest to industry. We follow the results that have been obtained in this context and eventually we arrive at the recent turbulence models of non-Newtonian fluids.

In this chapter a new approach to calculating turbulent flows of power-law and yield stress fluids is proposed. Emphasis is put on correcting the near wall modelling which in standard approaches does not take the fluid rheology into account. In the spirit of the RANS wall function modelling several possible corrections are proposed and tested on a wide range of experimental conditions.

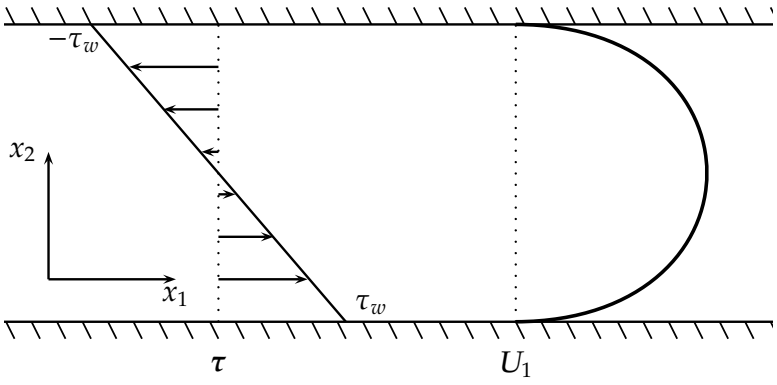

Figure 4.1: Channel flow: stress and velocity profile sketch.

4.1 Newtonian turbulence in channels and pipes

Consider the flow presented on Figure 4.1. Consider the flow is steady and fully developed so that all streamwise and time derivatives vanish. If additionally the flow is incompressible than the simplified single phase momentum equations are as follows:

$$\frac{\partial U_i}{\partial x_i} = 0, \tag{4.1}$$

$$0 = -\frac{1}{\rho}\frac{\partial p}{\partial x_1} - \frac{\partial}{\partial x_2}\overline{u_1 u_2} + \nu\frac{\partial^2 U_1}{\partial x_2^2}, \tag{4.2}$$

$$0 = -\frac{1}{\rho}\frac{\partial p}{\partial x_2} - \frac{\partial}{\partial x_2}\overline{u_2^2}, \tag{4.3}$$

where $\overline{u_i u_j}$ is the Reynolds stress i.e. correlation between fluctuating velocities. The second momentum equation can be readily integrated giving:

$$\frac{p}{\rho} + \overline{u_2^2} = \frac{p_w}{\rho}, \tag{4.4}$$

where $p_w = p(x_1, 0, 0)$ is a pressure at the wall and therefore is a function of the axial coordinate only. Upon substitution of this equation into the first momentum equation, recalling that velocity statistics are independent of the axial coordinate (fully developed flow) and with subsequent integration along x_2 we obtain:

$$0 = -\frac{x_2}{\rho}\frac{\partial p_w}{\partial x_1} - \overline{u_1 u_2} + \nu\frac{\partial U_1}{\partial x_2} - u_\tau^2 \tag{4.5}$$

where $u_\tau = \sqrt{\frac{\tau_w}{\rho}}$ relating it to shear stress at the wall. At this stage Equation (4.5) still has many solutions. There are two unknown functions: Reynolds stress and velocity. By applying a symmetry condition of the form $\overline{u_1 u_2} + \nu \frac{\partial U_1}{\partial x_2} = 0$ at $H/2$ we observe that the balance between remaining terms gives:

$$-\frac{\delta}{\rho}\frac{\partial p_w}{\partial x_1} = u_\tau^2, \tag{4.6}$$

where $2\delta = H$. After substitution to Equation (4.5) we arrive with:

$$-\overline{u_1 u_2} + \nu \frac{\partial U_1}{\partial x_2} = u_\tau^2 \left(1 - \frac{x_2}{\delta}\right). \tag{4.7}$$

With these simplifications, further analysis will just be an exercise in coordinate perturbation coupled with dimensional analysis. The reasoning is based on Tennekes and Lumley (1972).

The x momentum balance equation may written in the following non-dimensional forms:

$$-\frac{\overline{u_1 u_2}}{u_\tau^2} + \mathrm{Re}_\tau^{-1} \frac{\partial}{\partial \eta}\frac{U_1}{u_\tau} = 1 - \eta \tag{4.8}$$

$$-\frac{\overline{u_1 u_2}}{u_\tau^2} + \frac{\partial}{\partial y^+}\frac{U_1}{u_\tau} = 1 - \mathrm{Re}_\tau^{-1} y^+ \tag{4.9}$$

scaled by $\eta = x_2/\delta$, $y^+ = x_2 u_\tau/\nu$ and with Reynolds number as $\mathrm{Re}_\tau = u_\tau \delta/\nu$.

Lastly, from the purely mathematical standpoint the symmetry condition does not have to hold. Also the point where the stress is equal to zero does not have to coincide with the centre of the channel. This assumption was introduced on empirical grounds only. A plausible justification is that steady state, fully developed flow without Reynolds decomposition has the zero stress point exactly in the centre. It is the introduction of a new function, namely Reynolds stress, which distorts the symmetry that is contained in the original equations.

4.1.1 Logarithmic law of the wall

In the large Reynolds number limit Equation (4.9) the Reynolds number effect on the RHS becomes negligible. Therefore, the left hand side terms have to be functions of y^+ only:

$$\frac{\overline{u_1 u_2}}{u_\tau^2} = g(y^+) \tag{4.10}$$

$$\frac{U_1}{u_\tau} = f(y^+) \tag{4.11}$$

Function f will play the role of an inner expansion. After neglecting Reynolds stress, which vanishes at the wall anyway, we can integrate Equation (4.9) and obtain a linear profile which is valid close to the wall.

$$\frac{U_1}{u_\tau} \sim y^+ \tag{4.12}$$

Unfortunately the asymptotic form of the momentum equations will reveal nothing more. To obtain proper scaling relations we have to turn to the turbulent kinetic energy equation. For this case it takes the form:

$$\overline{u_1 u_2}\frac{\partial U_1}{\partial x_2} = -\frac{\partial}{\partial x_2}\left(\frac{1}{\rho}\overline{p u_2} + \frac{1}{2}\overline{u_i u_i u_2}\right) - \epsilon. \tag{4.13}$$

From Equation (4.8) we know that $u_1 u_2$ scales as u_τ^2. Based on this, an argument can be constructed for pure shear flows (see Tennekes and Lumley (1972)) that the RHS of the above scales as u_τ^3/δ. With this estimate[1] the velocity gradient scales as:

$$\frac{\partial U_1}{\partial y} = \frac{u_\tau}{\delta}\frac{\partial F}{\partial \eta}, \tag{4.14}$$

where F is an unknown function that will play the role of an outer expansion.
Having defined inner and outer expansions the third step is to match the functions in the limits where one coordinate begin to overlap the other (coordinate perturbation). Instead of matching the functions themselves it is better to perform matching on the functions' derivatives. Using the inner expansion the velocity gradient can be expressed as:

$$\frac{\partial U_1}{\partial y} = \frac{u_\tau^2}{\nu}\frac{\partial f}{\partial y^+}, \tag{4.15}$$

and the matching condition is:

$$\frac{u_\tau}{\delta}\frac{\partial F}{\partial \eta} = \frac{u_\tau^2}{\nu}\frac{\partial f}{\partial y^+}, \tag{4.16}$$

which upon multiplication by y gives:

$$\eta\frac{\partial F}{\partial \eta} = y^+\frac{\partial f}{\partial y^+}. \tag{4.17}$$

[1] To obtain it a set of equations describing the evolution equation of u_i^2 for each i have to be derived and compared the dissipation term that is known to scale as u_τ^3/δ. The lack of production terms in equations for components normal to the mean flow suggests that the energy is redistributed through pressure interaction terms which have to sum up to zero due to incompressibility. Note that the flow is not isotropic.

Now assuming that η and y^+ are independent quantities, we may conclude that the left and right side of Equation (4.17) has to be equal to a constant:

$$\eta \frac{\partial F}{\partial \eta} = \frac{1}{\kappa} \tag{4.18}$$

The outer solution might not be valid close to the wall and therefore the integration has to be conducted from the centre of the channel leading to:

$$\frac{U_c - U_1}{u_\tau} = F(\eta) \tag{4.19}$$

where $U_c = U_1(\delta)$ is the mean velocity at the centre. After integration we obtain:

$$\frac{U_c - U_1}{u_\tau} = F(\eta) = \frac{1}{\kappa} \ln \eta + C_1, \tag{4.20}$$

$$\frac{U_1}{u_\tau} = f(y^+) = \frac{1}{\kappa} \ln y^+ + C_2, \tag{4.21}$$

which is the well-known logarithmic law of the wall. The above analysis can be repeated for pipelines which will also result in a logarithmic velocity profile (see Pope (2000); Tennekes and Lumley (1972)).

4.1.2 Friction factors for pipelines

There are numerous laws relating, pressure gradient, flow rates and other problem parameters. For pipeline design and also for validation of turbulence models the Darcy–Weisbach friction factor expression is commonly used:

$$f = \frac{\Delta p D}{\frac{1}{2} \rho U_b^2 L}, \tag{4.22}$$

where L is pipe length, D pipe diameter, ρ density, U_b is the stream-wise velocity averaged over crossection. Averaged values must be understood in a sense appropriate for a given flow problem e.g. in the context of pipelines the bulk velocity which is given by:

$$U_b = \frac{1}{\pi R^2} \int_0^R 2U_1(r) \pi r \, \mathrm{d}r \tag{4.23}$$

Writing down the equations of motion in cylindrical coordinates (convenient for a pipeline) and with the above definitions it is already possible to draw several relations (see Pope (2000)):

$$\frac{u_\tau}{U_b} = \sqrt{\frac{1}{f}} \tag{4.24}$$

An analysis similar to Section 4.1.1 but performed in cylindrical coordinates can be now applied to yield an estimate of bulk velocity.

Moreover the so called "friction law of smooth pipes" can be obtained which explicitly captures the Reynolds number effect. The law may be obtained by simply adding Equations (4.20) and (4.21) which eliminates dependency on the y^+ coordinate leading to:

$$\frac{U_0}{u_\tau} = \frac{1}{\kappa} \ln \left(\mathrm{Re} \left(\frac{U_0}{u_\tau} \right)^{-1} \right) + C_1. \tag{4.25}$$

This result with appropriate constants which have to be given empirically is:

$$\frac{1}{\sqrt{f}} = 2.0 \log_{10} \left(\sqrt{f} \mathrm{Re} \right) - 0.8 \tag{4.26}$$

where the empirical constants have been chosen to fit Nikuradse (1932) data who performed a number of experiments for turbulent flows in pipes.

The above law performs well for smooth pipes. In practice, the internal surface might not be smooth. Nikuradse (1933) presents friction factor data for rough pipes.

$$f = \frac{1}{\left(2 \log \frac{R}{k_r} + 1.74 \right)^2}, \tag{4.27}$$

where $R = D/2$ and k_r is the roughness parameter.

Smooth and fully rough pipes represent two extreme cases for friction factors. The experimental data reveal also an existence of a transition region. To account for it in a friction factor expression Colebrook (1939) proposed:

$$\frac{1}{\sqrt{f}} = 1.74 - 2.0 \log_{10} \left(\frac{k_r}{R} + \frac{18.7}{\sqrt{f} \mathrm{Re}} \right). \tag{4.28}$$

This formula reduces to Prandtl law of smooth pipes if k_r is set to zero. The von Karman law, which captures the rough pipe data, is recovered if $\mathrm{Re} \to \infty$.

4.1.3 Relevant quantities and their order of magnitude analysis

For the purpose of developing turbulence models, especially low-Reynolds number turbulence models, it is necessary to secure so called asymptotic consistency with the wall behaviour. To gain into insights about the variation of Reynolds stresses in the vicinity

of a solid wall a Taylor expansion of fluctuating components is carried out:

$$u_1 = a_{11} + a_{12}x_2 + \ldots, \tag{4.29}$$

$$u_2 = a_{21} + a_{22}x_2 + \ldots, \tag{4.30}$$

$$u_3 = a_{31} + a_{32}x_2 + \ldots. \tag{4.31}$$

By applying a no slip boundary condition we observe that the first terms of each equation a_{i1} vanish. Moreover substituting these expansions into the continuity equation results in $a_{22} = 0$. With these relations we can estimate the Reynolds stresses and consequently terms in the equations of turbulent kinetic energy. The equation for fully developed flows is the following:

$$\frac{\partial}{\partial x_2}\left(\frac{1}{2}\overline{u_i u_i u_2} + \frac{1}{\rho}\overline{u_2 p'} - \nu\frac{\partial}{\partial x_2}\left(k + \overline{u_2^2}\right)\right) = P - \epsilon \tag{4.32}$$

where p' denotes fluctuating pressure. With

$$P = \mathcal{O}(x_2^3) \qquad \epsilon = \mathcal{O}(1), \tag{4.33}$$

$$\nu\frac{\mathrm{d}^2 k}{\mathrm{d}x_2^2} = \mathcal{O}(1), \qquad \nu\frac{\mathrm{d}^2\overline{u_2^2}}{\mathrm{d}x_2^2} = \mathcal{O}(x_2^2) \tag{4.34}$$

$$\frac{\partial}{\partial x_2}\left(\frac{1}{2}u_2\overline{u_i u_i}\right) = \mathcal{O}(x_2^3) \qquad \frac{\partial}{\partial x_2}\left(\frac{\overline{u_2 p'}}{\rho}\right) = \mathcal{O}(x_2) \tag{4.35}$$

The above estimates are important as they provide the desirable asymptotic behaviour of low-Reynolds number models.

4.1.4 Near-wall treatments

The structure of a turbulent boundary layer exhibits large gradients of velocity and quantities characterising turbulence, compared with the flow in the core region. In a collocated grid these gradients will be approximated using discretisation procedures which are not suitable for such high variation since they usually assume linear interpolation of values between cell centres.

Moreover, the additional quantities appearing in the two-equation models that were briefly presented in Chapter 3 require specification of their boundary conditions that from purely physical grounds cannot be specified *a priori*.

This situation gave rise to a plethora of near-wall treatments. Two approaches can be distinguished:

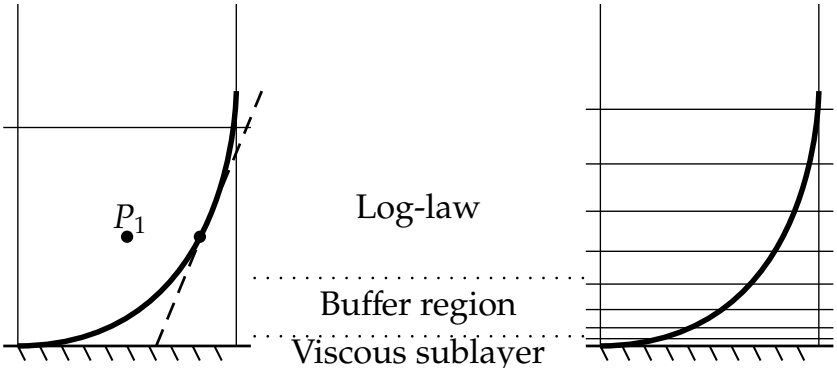

Figure 4.2: Turbulent boundary layer structure with respect to the first computational cell. High and low Reynolds number approaches i.e. wall function against fine grid (possibly with damping functions).

- Low Reynolds number treatment (LRN) integrates every equation up to the viscous sublayer and therefore the first computational cell must have its centroid at $y^+ \sim 1$. This results in very fine meshes close to the wall. Additionally, for some models additional treatment (damping functions) of the equations is required to guarantee asymptotic consistency with the turbulent boundary layer behaviour. This often makes the equations stiff and further increases computation time.

- High Reynolds number treatment (HRN) also known as the wall functions approach relies on a log-law velocity profile and therefore the first computational cell must have its centroid in the log-layer. Use of HRN often enhances convergence rate and numerical stability.

Interestingly, neither of the current approaches can deal with buffer layer i.e. the layer in which both viscous and Reynolds stresses are significant. The first computational cell should be either in viscous sublayer or in log-layer – not in-between. Automatic wall treatments, available in some codes, are an *ad hoc* solution but the blending techniques employed there are usually arbitrary and though they can achieve the switching between HRN and LRN treatments they cannot be regarded as the correct representation of the buffer layer.

4.1.4.1 Low Reynolds-number treatment

Low Reynolds approaches employ fine grids to resolve the turbulent boundary layer. Some models require additional care in order to guarantee consistency with the known asymptotic behaviour at the wall. In particular in a standard k-ϵ model eddy viscosity vanishes as y^4 at the wall, whereas from the considerations presented in Section 4.1.3 it is supposed to vanish as y^3.

To deal with the problem many low Reynolds-number corrections have been proposed. These models use additional functions that dampen some terms in model equations. As an example and also for future reference Lam and Bremhorst (1981) k-ϵ model equations are:

$$\nu_t = C_\mu f_\mu k^2/\epsilon, \tag{4.36}$$

$$\frac{\partial k}{\partial t} + \frac{\partial U_i k}{\partial x_i} = \frac{\partial}{\partial x_i}\left[(\nu + \nu_t/\sigma_k)\frac{\partial k}{\partial x_i}\right] + P - \epsilon, \tag{4.37}$$

$$\frac{\partial \epsilon}{\partial t} + \frac{\partial U_i \epsilon}{\partial x_i} = \frac{\partial}{\partial x_i}\left[(\nu + \nu_t/\sigma_\epsilon)\frac{\partial \epsilon}{\partial x_i}\right] + C_{1\epsilon} f_1 P\epsilon/k - C_{2\epsilon} f_2 \epsilon^2/k, \tag{4.38}$$

with the damping functions:

$$f_\mu = [1 - \exp(-0.0165\mathrm{Re}_w)]^2/(1 + 20.5/\mathrm{Re}_t), \tag{4.39}$$

$$f_1 = 1 + (0.05/f_\mu)^3 \tag{4.40}$$

$$f_2 = 1 - \exp(-\mathrm{Re}_t^2) \tag{4.41}$$

where $\mathrm{Re}_w = \sqrt{k} y_w/\nu$ is a wall Reynolds number with y_w being the wall distance. Finally, $\mathrm{Re}_t = k^2/(\epsilon\nu)$ is a turbulent Reynolds number. A Taylor expansion around the wall will show that ν_t now vanishes as y^3. Unlike HRN approaches, LRN can reproduce classical laminar solutions e.g. a parabolic velocity profile in a channel or a pipeline. This is demonstrated in Appendix A where it is also compared with other commercially available LRN models and with laminar model for a range of Reynolds numbers and meshes.

4.1.4.2 High-Reynolds number treatment

There are two possible ways of implementing wall functions in a finite volume code:

- Additional source term in the momentum equations.

- Modification of turbulent viscosity in cells adjacent to solid walls.

The source term in the first approach is simply the difference between the logarithmic and linear interpolation of velocity gradient multiplied by viscosity (the difference between a shear stress using linear interpolation and the shear stress from logarithmic interpolation). The second approach does not attempt to reproduce the correct velocity gradient. Instead, turbulent viscosity is modified in such a way as to guarantee the correct shear stress. After reorganising Equation (4.21) and using $\tau_w = \rho u_\tau^2$ we obtain:

$$\tau_w = \frac{\rho u_\tau \kappa U}{\ln E y^+}, \tag{4.42}$$

where $E = 9.8$ is equivalent to additive constants. On the other hand, the linear interpolation for shear stress $U\big|_{y=0} = 0$ we have:

$$\tau_w = \rho(\nu_t + \nu)\frac{U_p}{y_p}. \tag{4.43}$$

Comparing Equations (4.42) and (4.43) an expression for turbulent viscosity can be obtained:

$$\nu_t = \nu\left(\frac{y^+\kappa}{\ln E y^+} - 1\right). \tag{4.44}$$

Note that u_τ has been been incorporated in y^+. The latter remains the only unknown in the equation and has to be estimated for the current velocity field. In the standard approach this cannot be done explicitly and instead an implicit way of obtaining y^+ has to be employed.

After multiplying Equation (4.21) by y_p/ν we obtain a compact version

$$\frac{\kappa U_p y_p}{\nu} = y^+ \ln E y^+, \tag{4.45}$$

This equation can be solved numerically with respect to y^+ for example via root searching algorithms e.g. Newton's method for specified U_p, y_p and ν. One iteration in a Newton's method for Equation (4.45) is

$$y^+_{n+1} = \frac{\frac{\kappa U_p y_p}{\nu} + y^+_n}{1 + \ln E y^+_n}. \tag{4.46}$$

Thus obtained y^+ is then substituted to Equation (4.44). Eventually the estimated u_τ serves also to define the values of turbulent quantities in the cell adjacent to the wall:

$$k_p = \frac{u_\tau^2}{\sqrt{C_\mu}}, \qquad \omega_p = \frac{\sqrt{k_p}}{C_\mu^{1/4}\kappa y_p}, \tag{4.47}$$

which are the values for k and ω according to Wilcox (2006) asymptotic analysis of log layer. These wall functions for k and ω are a results of a solution of model equation for the logarithmic layer.

The above methodology is known in the literature as Standard Wall Functions. It has been shown that this approach has many limitations, especially in separated flows like backward facing step, where u_τ becomes zero by definition in separation and reattachment points. A different approach is to use the relation $u_\tau = C_\mu^{1/4}\sqrt{k}$ in both y^+ and Equation (4.42) leading to:

$$\nu_t = \nu\left(\frac{y^*\kappa}{\ln Ey^*} - 1\right), \tag{4.48}$$

where

$$y^* = \frac{y_p C_\mu^{1/4}\sqrt{k}}{\nu} \tag{4.49}$$

To guarantee the correct behaviour of k in the first cell the production term is adjusted:

$$P_p = -\overline{u_1 u_2}\frac{\partial U_1}{\partial x_2} = \underbrace{(\nu_t + \nu)\frac{\partial U_1}{\partial x_2}}_{\text{Boussinesq assumption}} \underbrace{\frac{C_\mu^{1/4}\sqrt{k_p}}{\kappa y_p}}_{\text{Logarithmic velocity}} \tag{4.50}$$

and ω_p is specified as in Equation (4.47).

This enhancement has been proposed by Launder and Spalding (1974). For rough surfaces a different form of log law velocity has to be used to derive the correct wall functions.

4.2 Constitutive laws

From a mathematical point of view a non-Newtonian rheology changes the stress term in the Navier–Stokes equation. The modifications may come under various forms including the introduction of viscometric functions or a new differential equation relating stress tensor to the rate of strain tensor. Viscometric functions introduce a variation of viscosity with relation to the scalar invariants of the rate of strain tensor. The differential equation can account for history and can capture effects like viscoelasticity. The former is usually applied for robust engineering calculations of steady state flow whereas the latter is used primarily for scientific purposes to understand the impact of non-Newtonian behaviour in transient and complex flow simulations.

4.2.1 Reiner–Rivlin fluids

Reiner–Rivlin fluids arise by applying principles of material isotropy and homogeneity (see Astarita and Marrucci (1974)) to an equation of the form:

$$\boldsymbol{\tau} = g(\hat{\boldsymbol{S}}), \tag{4.51}$$

where

$$\hat{\boldsymbol{S}} = [\hat{s}_{ij}]_{ij}\,, \qquad \hat{s}_{ij} = \frac{1}{2}\left(\frac{\partial \hat{u}_i}{\partial x_j} + \frac{\partial \hat{u}_j}{\partial x_i}\right), \tag{4.52}$$

where $\hat{u}_i$ is an instantaneous velocity. The hat symbol was introduced to distinguish between instantaneous and fluctuating values. By homogeneity we mean that the material function g does not change with respect to translation of the frame of reference. Isotropy states that any rotation of the frame of reference leaves the form of the function g intact. The latter can be formally rewritten as:

$$\boldsymbol{Q} \cdot g(\hat{\boldsymbol{S}}) \cdot \boldsymbol{Q}^T = g(\boldsymbol{Q} \cdot \hat{\boldsymbol{S}} \cdot \boldsymbol{Q}^T), \tag{4.53}$$

where $\boldsymbol{Q}$ is an orthogonal tensor. Isotropic and symmetric tensor function can only be of the following form:

$$g(\hat{\boldsymbol{S}}) = \phi_0 \mathbf{1} + \phi_1 \hat{\boldsymbol{S}} + \phi_2 \hat{\boldsymbol{S}}^2. \tag{4.54}$$

The scalar coefficients can depend only on the tensor scalar invariants $\mathrm{I}_{\boldsymbol{S}}$, $\mathrm{II}_{\boldsymbol{S}}$, $\mathrm{III}_{\boldsymbol{S}}$ defined as:

$$\mathrm{I}_{\boldsymbol{S}} = \mathrm{tr}\hat{\boldsymbol{S}}, \tag{4.55}$$

$$\mathrm{II}_{\boldsymbol{S}} = \mathrm{tr}\hat{\boldsymbol{S}}^2 - \mathrm{tr}\hat{\boldsymbol{S}}^2, \tag{4.56}$$

$$\mathrm{III}_{\boldsymbol{S}} = \det\hat{\boldsymbol{S}}, \tag{4.57}$$

where tr is the trace. The first invariant, denoted $\mathrm{I}_{\boldsymbol{S}}$ vanishes for incompressible flows. The first term in Equation (4.54) can also be neglected since we expect the stress to be zero if no deformation occurs. Therefore we have:

$$\boldsymbol{\tau} = \phi_1\left(\mathrm{II}_{\boldsymbol{S}}, \mathrm{III}_{\boldsymbol{S}}\right)\hat{\boldsymbol{S}} + \phi_2\left(\mathrm{II}_{\boldsymbol{S}}, \mathrm{III}_{\boldsymbol{S}}\right)\hat{\boldsymbol{S}}^2. \tag{4.58}$$

A fluid that satisfies above equation is called Reiner-Rivlin fluid and the functions ϕ_1, ϕ_2 are often referred to as material functions. Newtonian case is reconstructed by taking $\phi_1 = 2\mu$, $\phi_2 = 0$. The main drawback of this model is its inability to account for normal-stress effects.

4.2.2 Generalised Newtonian fluids

An important subclass of Reiner–Rivlin fluids is a group called generalised Newtonian fluids (GNF). This class is obtained by taking:

$$\phi_1(\mathrm{II}_{\boldsymbol{S}}, \mathrm{III}_{\boldsymbol{S}}) = \mu(\mathrm{II}_{\boldsymbol{S}}), \tag{4.59}$$

$$\phi_2(\mathrm{II}_{\boldsymbol{S}}, \mathrm{III}_{\boldsymbol{S}}) = 0. \tag{4.60}$$

The literature usually denotes

$$\dot{\gamma} = \sqrt{2\mathrm{II}_{\boldsymbol{S}}}, \tag{4.61}$$

and defines viscosity models with respect to this parameter.
The most popular is the Ostwald–de Waele model (see Chhabra (2006)), also known as power-law model. It aims to describe a log-linear relation that commonly observed in many industrial processes.

$$\mu = K\left(\dot{\gamma}\right)^{n-1} \tag{4.62}$$

where K is a so called consistency index and n is a power-law index, both chosen empirically. Based on the latter one we can introduce the following distinction:

1. $n < 1$ is called shear-thinning fluid,
2. $n > 1$ is a shear-thickening fluid,
3. $n = 1$ is a Newtonian fluid.

It should be emphasized that the power-law is applicable on finite shear intervals only. Also it exhibits a singularity close to $\dot{\gamma} = 0$ which can cause numerical solvers to complain. This is why various regularisation are considered, of which the most common is:

$$\mu = \begin{cases} K\left(\dot{\gamma}\right)^{n-1} & \mu_0 \leqslant K\left(\dot{\gamma}\right)^{n-1} \leqslant \mu_\infty \\ \mu_0 & K\left(\dot{\gamma}\right)^{n-1} < \mu_0 \\ \mu_\infty & K\left(\dot{\gamma}\right)^{n-1} > \mu_\infty \end{cases}, \tag{4.63}$$

where limiting viscosities μ_0, μ_∞ have been imposed somewhat brutally.
A more elegant solution is the Cross model which is defined on a single interval and guarantees a smooth[1] transition between limiting viscosities.

$$\mu = \mu_\infty + \frac{\mu_0 - \mu_\infty}{1 + \left(\lambda\dot{\gamma}\right)^{1-n}}. \tag{4.64}$$

[1]The function is in C^∞ i.e. having continuous derivatives

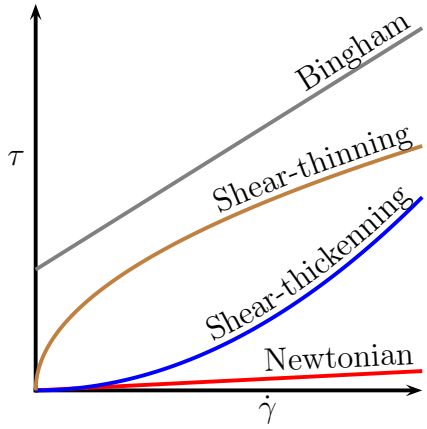

Figure 4.3: Various classes of genaralised Newtonian fluids.

4.2.3 Viscoplasitc fluids

Another class of fluids are fluids that do not yield if the stress does not exceed certain critical value called yield stress. The Herschel–Bulkey fluid is a constitutive law that models this behaviour:

$$K\dot{\gamma}^n = \begin{cases} 0 & \tau < \tau_Y \\ \tau - \tau_Y & \text{otherwise} \end{cases}, \tag{4.65}$$

where τ_y is the yield stress, K is a consistency index, n is a power law index, τ_Y is a yield stress. For $\tau_y = 0$ the model reduces to power-law model of Ostwald–de Waele and for $n = 1$ Bingham plastic behaviour is reproduced.
Two regularisations used in the literature and computational codes are

$$\mu = \begin{cases} \mu_y & \dot{\gamma} < \tau_y/\mu_y \\ \frac{\tau_y}{\dot{\gamma}} + K\dot{\gamma}^{n-1} & \text{otherwise} \end{cases} \tag{4.66}$$

and the exponential one suggested by Papanastasiou (1987):

$$\mu = \left(1 - e^{-m\dot{\gamma}}\right) \frac{(\tau_y + K\dot{\gamma}^n)}{\dot{\gamma}}. \tag{4.67}$$

These regularised forms can be also considered as examples of Reiner–Rivlin fluids

4.2.4 Viscoelastic fluids

A viscoelastic fluid is a one which combines viscosity and elasticity. The link between these behaviours can be postulated by equation:

$$\tau_{21} + \frac{\mu}{G}\frac{\partial \tau_{21}}{\partial t} = -\mu\dot{\gamma}_{21}. \tag{4.68}$$

In steady state the second term on the left hand side is small and the equation reduced to the well-known Newtonian relation between strain rate and stress.
If the first term is neglected the integration of both sides gives Hooke's law:

$$\tau_{21} = -G\gamma \tag{4.69}$$

where γ is the infnitesimal strain (as opposed to strain rate). A more general equation is given by:

$$\boldsymbol{\tau} + \lambda_1 \frac{\partial \boldsymbol{\tau}}{\partial t} = -\mu \dot{\boldsymbol{\gamma}} \tag{4.70}$$

We can easily solve this equation obtaining

$$\boldsymbol{\tau}(t) = e^{-t/\lambda_1} \left(\int_{-\infty}^{t} -\frac{\mu}{\lambda_1} \dot{\boldsymbol{\gamma}}(t') e^{t'/\lambda} \, \mathrm{d}t' + C \right) \tag{4.71}$$

which shows the most important aspect of this model, namely the relationship between the stress and the history of strain.
Further generalisation of this model is the so called Jeffreys model which relates stress to the strain rate time derivative.

$$\boldsymbol{\tau} + \lambda_1 \frac{\partial \boldsymbol{\tau}}{\partial t} = -\mu \left(\dot{\boldsymbol{\gamma}} + \lambda_2 \frac{\partial \dot{\boldsymbol{\gamma}}}{\partial t} \right) \tag{4.72}$$

The experiments reported by Toms (1949) gave rise to research into a phenomenon called polymeric turbulence drag reduction. The work that has been undertaken since then had shown that it is possible to reduce the friction factor in a turbulent flow by up to 80% by adding just a few tens of parts per million (ppm) of long chain polymers. As Lumley (1964) points out this effect cannot be tied to purely viscous non-Newtonian effects and therefore has to rely on elastic effects. The DNS work by De Angelis et al. (2002); Sureshkumar et al. (1997); Vaithianathan (2003) shows, that the phenomenon can be explained by the higher extensional viscosity which inhibits vortex dynamics. This qualitative picture is yet to be furnished with quantitative predictions that relate rheology of the fluid to the actual flow as in Pinho et al. (2008).
Interestingly, a similar phenomenon can be observed in liquid with a fiber suspensions. Even more surprising is the fact that underlying mechanism of drag reduction in this case, despite some similarities with polymer solutions, is actually different. The most convincing demonstration of this fact is a mixture of polymer solutions with a fiber suspension which exhibits drag reduction greater than the sum of drag reduction of components alone.

4.2.5 Non-dimensional parameters

A common procedure when describing fluid dynamics problems is to non-dimensionalise the equations and then work only with non-dimensional groups e.g. Reynolds or Prandtl number to capture the relative contribution of various terms. Such ratios are useful in estimating the impact of corresponding effects.

In the context of viscoelastic fluids an important role is played by the Deborah[1] number which is a ratio of elastic to viscous forces and is given by:

$$\mathrm{De} = \frac{\lambda}{t_f} \tag{4.73}$$

where λ is a time scale describing the slowest molecular motion or a time constant stemming from linear viscoelasticity (Bird et al. (1987)) while t_f is a problem related time scale related to the longest path a fluid element is traveling e.g. L/U for steady state flows, where U is the magnitude of velocity and L length along velocity direction. As proposed by Reiner, the purpose is to measure the solid-like response of the fluid (see Phan-Thien (2008)) in the following sense: for $\mathrm{De} \to \infty$ the material behaves like a solid and for $\mathrm{De} = 0$ we have a liquid behaviour.

The other non-dimensional number, the Weissenberg number, measures the ratio of elastic effects to viscous effects by relating fluid relaxation time to strain rate:

$$\mathrm{We} = \lambda\kappa \tag{4.74}$$

where κ is characteristic strain rate e.g. U/D for steady state flow, where D is the length along the directions associated with the largest velocity gradient. The Weissenberg number can be only defined for flows with constant stretch history[2].

Finally the definition of known Newtonian dimensional numbers is slightly altered for above models. The first approximation of non-Newtonian turbulence might rely on the calculation of a Newtonian fluid with a viscosity equal to the wall-viscosity of non-Newtonian fluid. The estimate of non-Newtonian fluid wall viscosity can be expressed

[1] Deborah was a female prophetess of the Old Testament. The quantity was introduced by Reiner and the name refers to the following passage of Deborah's song: "Even the mountains will flow before the Lord". The Lord as a being with an infinite amount of time can indeed observe the viscous behaviour of mountains visible only on a sufficiently large time scale.

[2] Flows where the history of stretch does not depend on the time instant t but only on the time lag $t_2 - t_1$.

in terms of wall shear-stress:

$$\mu_w = K^{\frac{1}{n}} \tau_w^{\frac{n-1}{n}}, \tag{4.75}$$

$$\mu_w = \frac{K^{\frac{1}{n}} \tau_w}{(\tau_w - \tau_y)^{\frac{1}{n}}} \tag{4.76}$$

for power-law and Herschel–Bulkley fluids respectively. This allows us to define a wall Reynolds number:

$$\mathrm{Re}_w = \frac{\rho U_b D}{\mu_W}, \tag{4.77}$$

where U_b is the bulk velocity, D is the diameter and ρ the density of the fluid. We can combine these expressions now and couple them with friction factor expressions.

4.3 Friction factors

Recent review papers such as El-Emam et al. (2003) report more than 14 friction factors for non-Newtonian fluids in pipes. Most of them are accompanied by an analysis of the logarithmic region behaviour. This section briefly presents the results from the literature with some remarks about their applicability and derivation.

For laminar flows Metzner and Reed (1955) suggested a correlation utilising a generalised Reynolds number called henceforth Metzner–Reed (M–R) Reynolds number.

$$f = \frac{64}{\mathrm{Re}_{\mathrm{MR}}} \tag{4.78}$$

$$\mathrm{Re}_{\mathrm{MR}} = \frac{U_b^{2-n} D^n}{8^{n-1} K} \tag{4.79}$$

where $D = 2R$ is a pipe diameter.

4.3.1 Dodge and Metzner

The first theoretical analysis of turbulent non-Newtonian pipe-flows is ascribed to Dodge and Metzner (1959). They divided a flow in a pipe into three regions: laminar, transition and turbulent core. By applying dimensional analysis arguments and performing an asymptotic matching in the transition region they obtained velocity profiles in the transition and turbulent core regions. The velocity profile in the core region was then integrated yielding eventually an estimate of average velocity.

The formulae they obtained are the following:

$$\frac{U_c - U_1}{u_\tau} = -nA \ln\left(\frac{y}{R}\right)^n \quad \text{(turbulent core region)}, \tag{4.80}$$

$$\sqrt{\frac{1}{f}} = \frac{2}{n^{0.75}} \log\left[\mathrm{Re}_{\mathrm{MR}} f^{1-n/2}\right] - \frac{0.2}{n^{1.2}} \qquad \text{(friction factor)}. \tag{4.81}$$

4.3.2 Clapp

A similar relation for channel flow was derived by Clapp (1961) who applied the Prandtl mixing length hypothesis to close the channel flow Reynolds-averaged Navier–Stokes equations. The asymptotic analysis for laminar, transition and turbulent core region gave the following relations:

$$u^+ = (y^+)^{1/n} \quad \text{(laminar region)}, \tag{4.82}$$

$$u^+ = \frac{5.0}{n} \ln y^+ - 3.05 \quad \text{(transition region)}, \tag{4.83}$$

$$u^+ = \frac{C_1}{n} \ln y^+ + \frac{C_2}{n} \quad \text{(turbulent core)} \tag{4.84}$$

where $u^+ = U_1/u_\tau$, $y^+ = \rho u_\tau^{2-n} y^n / K$, and the friction factor:

$$\frac{1}{\sqrt{f}} = \sqrt{2}\left(\left(\frac{C_2}{2} - \frac{3C_1}{4}\right) \log \mathrm{Re}_{\mathrm{MR}} (\sqrt{f})^{2-n} + 0.174 C_1 \left(\frac{5n-8}{n}\right)\right). \tag{4.85}$$

The integration constants C_1 and C_2 were obtained as a result of experiment.

4.3.3 BNS equation

Szilas, Bobok and Navratil (1981) collected all the known friction factors at the time and derived a new one from the pipe flow momentum balance equation written in cylindrical coordinates. They approximated Reynolds stress using a closure by von Karman who derived it from similarity considerations:

$$\overline{u_1 u_2} = -\kappa^2 \left(\frac{\partial U_1}{\partial r}\right)^4 \left(\frac{\partial^2 U_1}{\partial r^2}\right)^{-2}. \tag{4.86}$$

where r is the radial coordinate. The rest of the analysis was conducted in a usual manner. An additional difficulty was the need to estimate the viscous sublayer width.

The resulting velocity profiles and friction factors are given below:

$$\frac{U_1}{u_\tau} = \frac{U_c}{u_\tau} + \frac{1}{\kappa}\left(\sqrt{\frac{r}{R}} + \ln\left(1 - \frac{r}{R}\right)\right) \qquad \text{(turbulent core)}, \tag{4.87}$$

$$\frac{u_{\max}}{u_\tau} = \frac{1}{n\kappa}\ln\left[\mathrm{Re}_{\mathrm{MR}}\left(\frac{u_\tau}{\overline{u}_2}\right)^{2-n}\right] - \frac{1}{\kappa}\left(1 + \frac{\ln\alpha}{n}\right) + \left(\frac{\alpha}{8}\right)^{1/n}\frac{6n-2}{n} \qquad \text{(maximum velocity)}, \tag{4.88}$$

$$\frac{1}{\sqrt{f}} = \frac{0.8141}{n\kappa}\log\mathrm{Re}_{\mathrm{MR}}f^{1-n/2} + 0.7532\frac{n-2}{2n\kappa} - 0.3535\left[\frac{1}{\kappa}\left(2.238 + \frac{\ln\alpha}{n}\right) + \left(\frac{\alpha}{8}\right)^{1/n}\frac{6n-2}{n}\right] \qquad \text{(friction factor)}. \tag{4.89}$$

The M–R Reynolds number used in the above formulae has the following form:

$$\mathrm{Re}_{\mathrm{MR}} = \frac{U_b^{2-n}D^n\rho}{\frac{K}{8}\left(\frac{6n+2}{n}\right)^n}. \tag{4.90}$$

4.3.4 Other friction factor correlations and some comparisons

Of course there are other non-Newtonian friction factor correlations. See El-Emam et al. (2003) for a more complete review. Worth noting are Tommita and Shaver–Merril (S–M). Shaver and Merrill extended the Blasius formula for pseudoplastic fluids while Tommitta got approached it from a similarity consideration. The latter confirmed the resulting predictions with experiments on lime slurries.

$$f = \frac{0.316}{n^5 Re_{MR}^m} \qquad \text{(Shaver–Merrill)} \tag{4.91}$$

$$m = \frac{2.63}{1.05^n} \tag{4.92}$$

$$\frac{1}{\sqrt{f}} = 2\log\left(Re\frac{\sqrt{f}}{2}\right) - 0.2 \qquad \text{(Tommita's)} \tag{4.93}$$

Comparisons of the accuracy of friction factors have been conducted by Szilas et al. (1981) and El-Emam et al. (2003). In the first review four out of five of the above equations were compared with experimental data gathered on the Algyö-Százhalombatta crude oll pipeline. The pipeline is 161.3 km long and 305 mm in diameter. Five series of measurements were taken at seven test points at Reynolds numbers varying for 10^4 to10^5. The best mean relative error of 0.39% was been obtained for the BNS equation. The next two were Clapp and Dodge–Metzner formulae with -1.75% and 1.96% relative errors. Tommita and S–M resulted in errors around 20%.

In the second review carried out by El-Emam et al. (2003) the friction factor data have been gathered from four different sets available in the literature. Ten friction factor formulae have been compared. According to the presented results the most accurate description, in a sense of mean deviation, was provided by a model using a regression analysis carried out by the authors in the same papers. Other equations performed reasonably well only on data for which they were calibrated. On average S–M and BNS equations were the second and third best, giving a percentage relative mean error below 10%, while D–M and Clapp were low in the ranking, scoring mean errors close to 20%.

4.4 Non-Newtonian wall function

Two ways of modifying wall functions are proposed here. The first one uses only the altered constants from Clapp (1961) and Dodge and Metzner (1959). The second one uses also an altered way of calculating wall distance based on the non-Newtonian definition of y^+.

The alteration of wall distance procedure based on Clapp (1961) and Dodge and Metzner (1959) formulae for the logarithmic layer is proposed here. The stage that has to be adjusted is the solution of y^+ from law of the wall. We assume that logarithmic law describes correctly the wall behaviour. For a non-Newtonian fluid the general form is given as:

$$\frac{U_1}{u_\tau} = A_n \ln y^+ + B_n, \tag{4.94}$$

where A_n and B_n are coefficients derived from experimental data and depend on the power-law index n. For Dodge and Metzner (1959) these coefficients are:

$$A_n = \frac{5.66}{n^{0.75} \ln 10}, \tag{4.95}$$

$$B_n = -\frac{0.4}{n^{0.75}} + \frac{2.458}{n^{0.75}} \left(1.96 + 1.255n - 1.628n \log_{10}\left(3 + \frac{1}{n}\right)\right). \tag{4.96}$$

And for Clapp (1961) we have

$$A_n = \frac{2.78}{n}, \tag{4.97}$$

$$B_n = \frac{3.8}{n}. \tag{4.98}$$

This can be expressed in a more compact form by:

$$U_1 = \frac{u_\tau}{\kappa_n} \ln E_n y^+ \tag{4.99}$$

where $E_n = \exp(B_n/A_n)$ and $\kappa_n = 1/A_n$. Currently Equation (4.94) has two unknowns, y^+ and u_τ and two experimental coefficients, E_n and κ_n. Using simple algebraic transformations it is possible to remove one of the unknowns.

$$\kappa_n^{2-n} U_1^{2-n} = u_\tau^{2-n} \left(\ln E_n y^+\right)^{2-n}. \tag{4.100}$$

Now multiplying by y^n/K the left hand side can be expressed as a non-Newtonian Reynolds number and on the right hand side non-Newtonian y^+ emerges.

$$\kappa_n \frac{U_1^{2-n} y^n}{K} = y^+ \left(\ln E_n y^+\right)^{2-n}. \tag{4.101}$$

Now for a given velocity field the left hand side is known. The procedure of calculating y^+ is derived based on one iteration of Newton's method of the function:

$$F(y^+) = \mathrm{Re}_\kappa - y^+ \left(\ln E_n y^+\right)^{2-n}. \tag{4.102}$$

The derivative of F with respect to y^+ is:

$$F'(y^+) = -\ln\left(E_n y^+\right)^{2-n} - (2-n)\ln\left(E_n y^+\right)^{1-n}. \tag{4.103}$$

In Newton's method we start with an initial guess for y^+ which we will denote as y_0^+. This is always initialised with the laminar value $y^+ = 11$. Then the procedure iterates using the following equations:

$$y_{n+1}^+ = y_n^+ - \frac{F(y^+)}{F'(y^+)}, \tag{4.104}$$

$$y_{n+1}^+ = \frac{\ln^{n-1}\left(E_n y^+\right)\mathrm{Re}_\kappa + (2-n)y^+}{\ln(E_n y^+) + (2-n)}, \tag{4.105}$$

which is a generalisation of Equation (4.46).

Wall functions that automatically calculate the coefficients for a given power-law index n have been implemented in OpenFOAM. Moreover the altered way of calculating wall distance has been implemented as an optional modification. Equation (4.105) is iterated no more than ten times and the tolerance is set statically in the code to 10^{-2}. The static set up is justified by the universality of the log-law behaviour and by the fact

that the procedure is executed as an inner iteration of the iteration of the main solver. A simple cross-check with FLUENT was also run to ensure that the wall functions from OpenFOAM give the same results. The test was successful and serves as validation of standard wall function in OpenFOAM.

A series of simulations was run to reproduce friction factor curves from Clapp (1961). Clapp (1961) is preferred to Dodge and Metzner (1959) because the final friction factor equation was correlated on the wider range of Reynolds numbers. All of these friction factor expressions are actually Fanning friction factors so they had to be additionally transformed into the Darcy–Weisbach formulation. The values of the parameters were non-dimensionalised and the simulated segment had a length of 10 diameters. Periodic boundary conditions were used at each end and the mass flux was specified using mean velocity. Axial symmetry was utilised. Because OpenFOAM is a three dimensional code only a circular sector instead of a 2D mesh was used. The sector had an angle of 1° and there was only one layer of cells in the angular direction. The number of cells in radial direction depended on y^+. For each case two meshes were used. The fine mesh kept $y^+ \sim 100$ whilst the coarse mesh had $y^+ \sim 300$. The streamwise direction was set to 300.

Power-law fluid with a cut-off was used for this test because the original log-law was derived for this case. The cut-off values are set up so that the lowest viscosity is never reached. This causes the power-law behaviour to affect the whole boundary layer. Also, the choice of a classical power-law makes the above methodology directly applicable. For Cross or Carreau–Yasuda, a suitable relationship between power-law indices would have to be used.

The error of the prediction is calculated in the following way:

$$e = \frac{|f_{\text{Clapp}} - f_{\text{CFD}}|}{f_{\text{Clapp}}} 100\% \tag{4.106}$$

where f_{Clapp} is the friction factor corresponding to Clapp friction factor curve and the f_{CFD} is the friction factor obtained from the calculation.

Figures 4.4 to 4.7 show the friction factors predicted with standard and modified wall functions. The continuous lines represent experimental curves from Clapp (1961) . The results agree well for flows with high Reynolds number but depart from the the experimental curves as Reynolds number decreases. Despite the proposed methodology

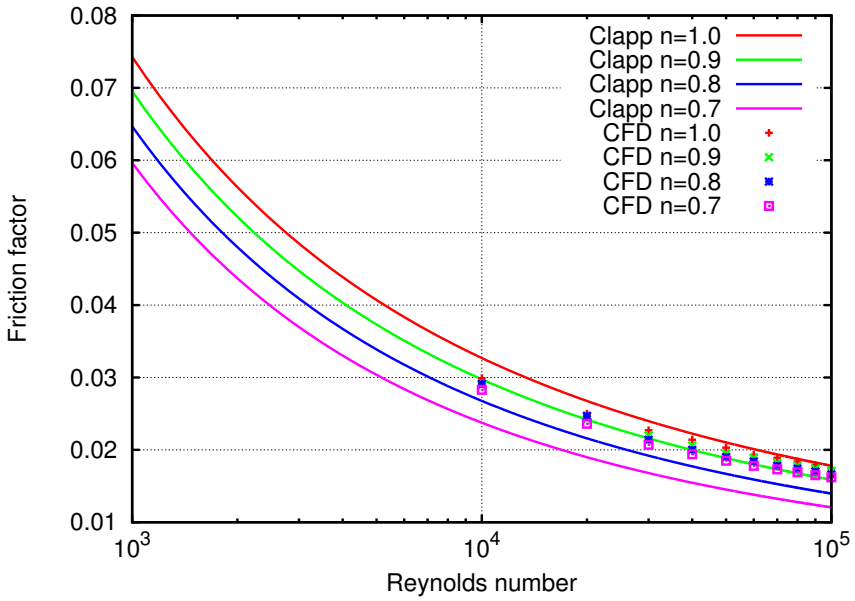

Figure 4.4: Prediction of non-Newtonian friction factors with standard wall functions.

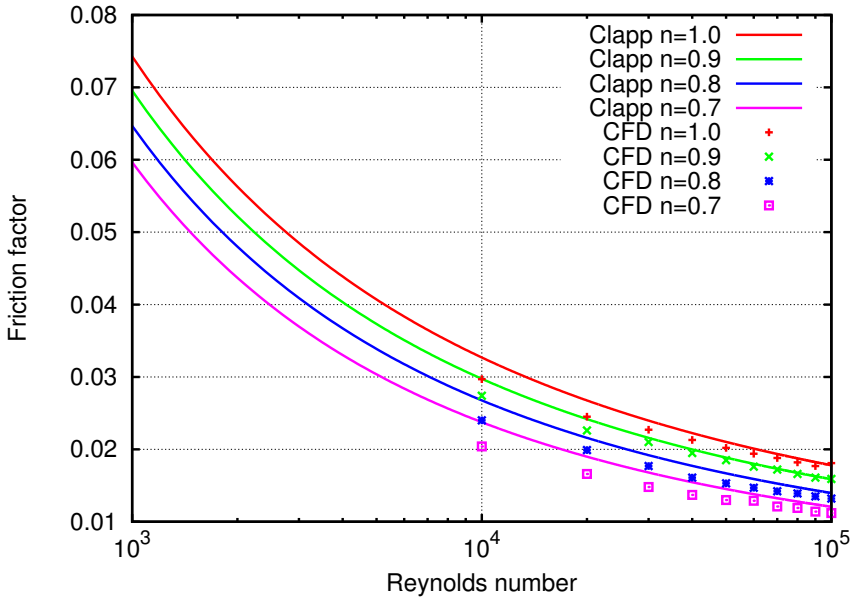

Figure 4.5: Prediction of non-Newtonian friction factors with Dodge and Metzner (1959) using only the profile constants.

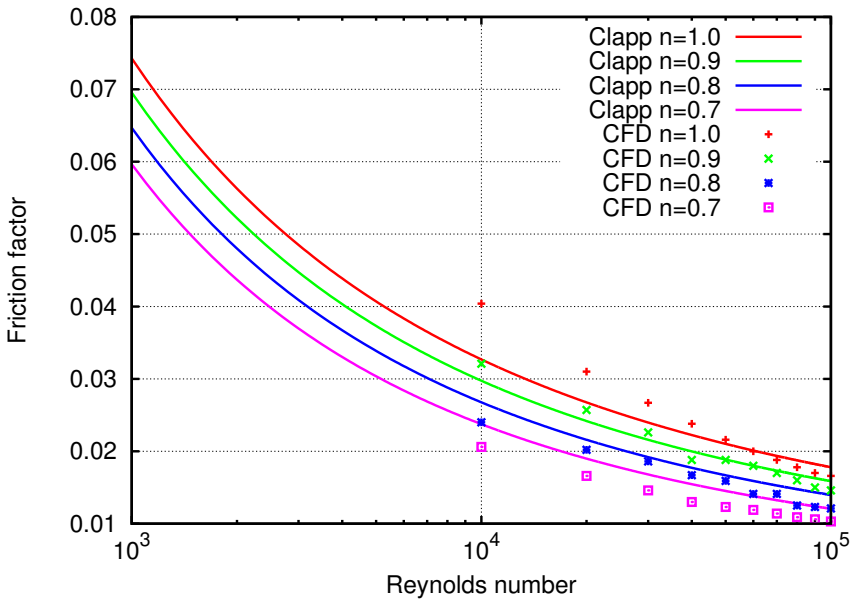

Figure 4.6: Prediction of non-Newtonian friction factors with Clapp (1961) using only the profile constants.

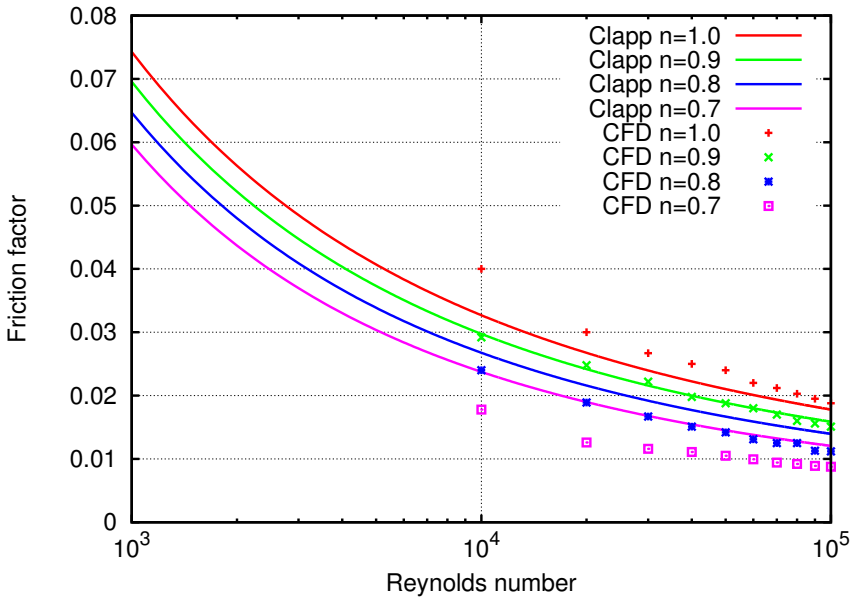

Figure 4.7: Prediction of non-Newtonian friction factors with Dodge and Metzner (1959) using wall distance calculation.

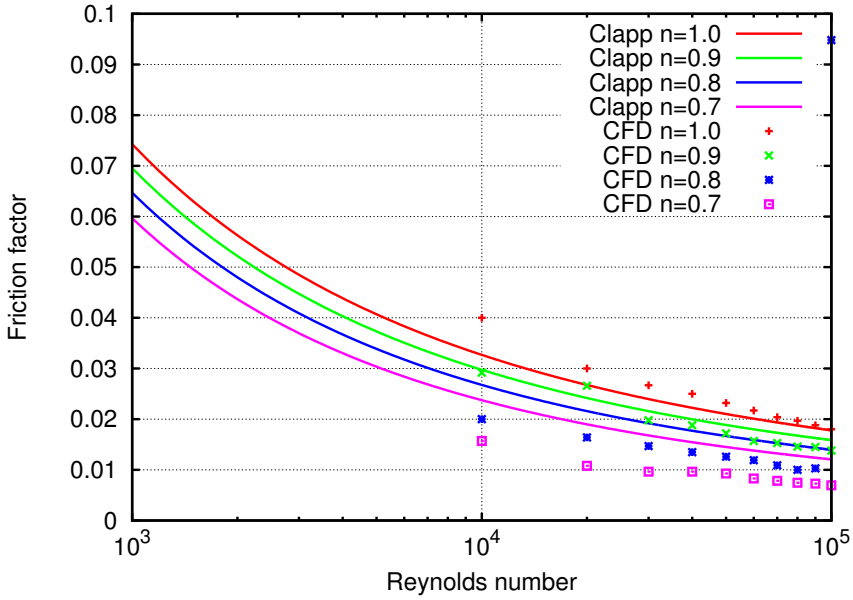

Figure 4.8: Prediction of non-Newtonian friction factors with Clapp (1961) using wall distance calculation.

it was impossible to keep y^+ above buffer layer values and the cell point was entering the buffer layer in the low Reynolds number cases.

The standard wall function is largely insensitive to fluid rheology and gives similar friction factor estimates for different values of power law index. Small discrepancies are the result of the wall viscosity entering the expression for y^+ in Equation (4.46). This is, however, not enough to account for the effect of the power-law index. Eventually, this results in errors of the order of 10% for Newtonian case but increasing to 35% with increasing the power-law index.

Non-Newtonian wall functions are rheology-aware and correctly predict the translation of the friction factor curve. As remarked on above the results deteriorate due to overly low y^+ values for the low Reynolds number cases. The main advantage is the modelling of the turbulent boundary layer for high Reynolds number.

The Newtonian behaviour is represented by the curve $n = 1$ and is reproduced correctly by all formulations of wall functions. The modified wall function correctly captures the Newtonian behaviour. A small discrepancy is caused by the difference in the experimental parameters used by Dodge and Metzner (1959) and Clapp (1961) which do

not coincide exactly with values from Nikuradse (1932). The best result was achieved with Dodge formulation where the error for high Reynolds numbers and most non-Newtonian fluid was reduced to within 1%. For the low Reynolds number the error of prediction remained at the level of 10%.
Moreover, Figure 4.10 compares the prediction of velocity and viscosity (both laminar and turbulent) profiles for the modified and unmodified function for the cases with the lowest n considered, which represents the furthest departure from Newtonian behaviour. We can see that the laminar viscosity changes across the pipe radius, which means that the cut-off values are not used and therefore should have no influence on the results. Turbulent viscosity shows the same trend but is altered due to different wall shear stress estimates imposed by the wall function. Moreover the values of turbulent viscosity compared with laminar viscosity are much larger which means that the rheology does not have significant impact far away from the wall.

4.5 Concluding remarks

Analytical investigation of the boundary layer can significantly improve the predictions of bulk quantities. Two benefits can be distinguished. Firstly, a friction factor expression can be derived based on the boundary layer analysis. This can lead to a robust method that can be of direct use to engineers designing pipelines. Secondly a model of near wall behaviour can be supplied for the purpose of CFD solvers, which which leads to a diminished demand for wall refinement and a more stable method.
As outlined in the literature review non-Newtonian properties alter the structure of the boundary layer by changing the coefficients in the universal laws for velocity. This leads to different expressions from those used in Newtonian flows and it is clear that the power-law index can affect the friction factor curve by translating it up or down depending on the power-law index.
In this chapter several modifications of standard wall functions have been proposed and tested against known friction factor expressions. The maximum improvement achieved was 35%. The result is promising but its practical application in situations relevant to engineering might pose serious difficulties. On one hand, the correct estimates for high Reynolds number are crucial since the friction factor is multiplied by the velocity squared which for high Reynolds number will be typically very large. But on the

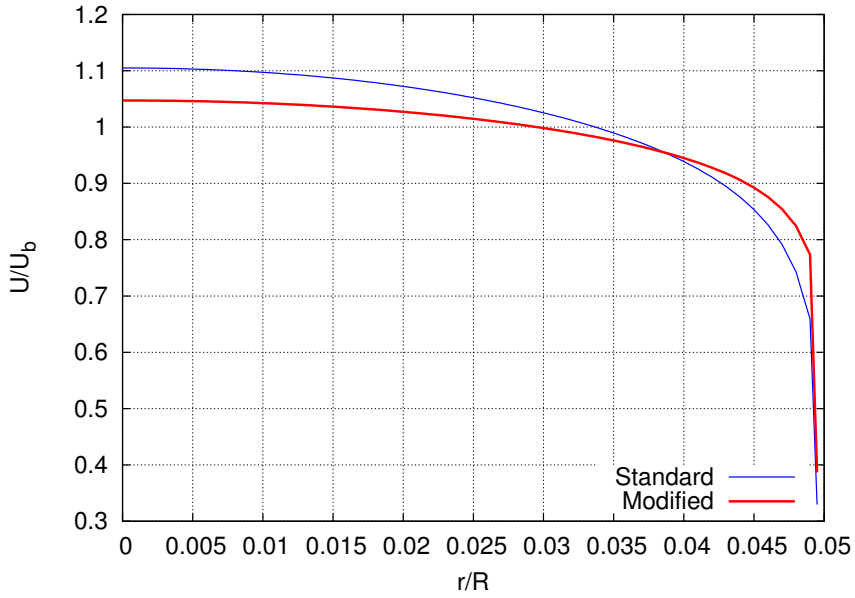

Figure 4.9: Velocity profiles for $n = 0.7$ and $\mathrm{Re_{MR}} = 10^6$.

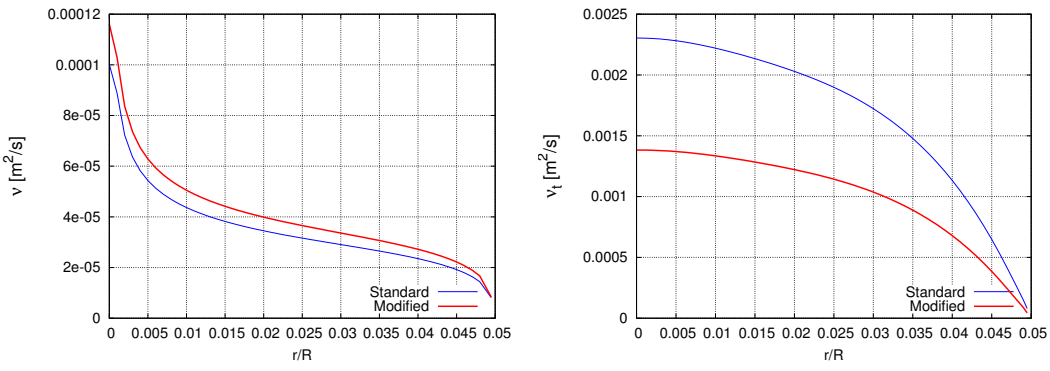

Figure 4.10: Laminar and turbulent viscosity profiles for $n = 0.7$ and $\mathrm{Re_{MR}} = 10^6$.

other hand for high Reynolds number the Colebrook-White equation suggests that pipe roughness might have a more important effect. This might further diminish the effect of fluid properties in the formation of the boundary layer.

A two layer model wall function could further explore possible advantages of the known rheology. Also, it is important to mention that only the constants in the ν_t wall function have been changed. To make these changes compatible with the whole wall function approach we also need to change the ϵ wall function. Still the presented results are a demonstration of the significance of including the power law index in the near wall modelling. The modification of ϵ wall function appears straightforward and is proposed as a further refinement of the method.

Chapter 5

Rate of strain in turbulent flow

The review of generalized Newtonian fluid (GNF) presented in Chapter 4 shows that all rheology models commonly used in the industry express viscosity in terms of the rate of strain. For RANS based CFD this means that both molecular and turbulent viscosity are functions of the flow field. Turbulent viscosity is expressed via the Boussinesq approximation, whereas molecular viscosity is expressed by a constitutive law.
In this chapter a relation between turbulent flow and the estimate of the rate of strain is studied. The issue of correct rate of strain and subsequently the correct viscosity estimation arose after running well known models against available experimental data. For some cases the predicted flow would have a laminar profile. The postulated reason for this behaviour was the flat velocity profile, characteristic for turbulent flow, and consequently molecular viscosity being large compared to eddy viscosity. This caused viscous effects to manifest themselves unnaturally far from the viscous sublayer, where one would normally expect them to be located.
Two hypotheses are proposed and examined.

1. The magnitude of the rate of strain of the instantaneous velocity field is an order of magnitude higher than the magnitude of the mean velocity field.

2. The instantaneous rate of strain follows a log-normal distribution.

The theoretical basis for these hypotheses is discussed in Section 5.1. Its verification is then presented in Section 5.3, where we look at DNS data that have been published in the literature. MATLAB has been used to construct histograms and best fit curves to collect other statistics of the relevant flow quantities. The chapter concludes with

Section 5.4 where the model is proposed and subsequently compared against other approaches in a set of new CFD calculations.

5.1 Theory

In a physical system that contains a GNF fluid, viscosity depends on the instantaneous rate of strain. However, in the RANS approach we are restricted to expected values of random variables and their second moments. The standard formulation of the k-ϵ turbulence model gives the rate of strain as the symmetric part of the mean velocity field gradient. This neglects any additional variation due to the fluctuating field. In the context of shear-thinning and yield stress fluids this leads to increased values of viscosity.

The following heuristic analysis provides some insight as to the significance of the neglected fluctuating terms. To examine the behaviour of rate of strain we decompose strain into mean and fluctuating parts:

$$\hat{s}_{ij} = S_{ij} + s_{ij} \tag{5.1}$$

and therefore the magnitude is:

$$\dot{\gamma} = \sqrt{2\hat{s}_{ij}\hat{s}_{ji}} = \sqrt{2S_{ij}S_{ji} + 4S_{ij}s_{ji} + 2s_{ij}s_{ji}}. \tag{5.2}$$

By invoking Jensen's inequality we have

$$\sqrt{2S_{ij}S_{ji}} \leqslant \overline{\dot{\gamma}} \leqslant \sqrt{2\overline{\hat{s}_{ij}\hat{s}_{ji}}} = \sqrt{2S_{ij}S_{ji} + 2\overline{s_{ij}s_{ji}}} \tag{5.3}$$

For homogeneous, isotropic, fully developed turbulence in a pure shear flow the transport equation for turbulence kinetic energy reduces to:

$$-\overline{u_i u_j}\, S_{ij} = 2\nu\overline{s_{ij}s_{ij}} \tag{5.4}$$

which comes from the assumption that production equals dissipation (see Tennekes and Lumley (1972)). Now assuming that turbulence is shear-generated with only one length scale l and one velocity scale u we can transform the above to:

$$ulS_{ij}S_{ij} \sim \nu\overline{s_{ij}s_{ij}}\,. \tag{5.5}$$

And now dividing both sides by ν will cause Reynolds number to appear on the left hand side:

$$\mathrm{Re} S_{ij} S_{ij} \sim \overline{s_{ij} s_{ij}}\,. \tag{5.6}$$

Since we assume Reynolds number to be large the following relation must hold:

$$S_{ij} S_{ji} \ll \overline{s_{ij} s_{ji}}\,. \tag{5.7}$$

Therefore, in any self-maintained turbulence the correlation of fluctuating rates of strain must be at least an order of magnitude higher than the squared mean rate of strain. Neglecting the fluctuating term will lead then to a significant underestimation of the rate of strain values which for shear-thinning and yield stress fluids correspond to increased values of viscosity. For turbulence simulation it means increased values of dissipation, lower Reynolds numbers and possibly the flow becoming laminar. Subsequently, the values of laminar viscosity will be incorrect in homogeneous region. Moreover the constitutive relationship will have a direct effect on the mean flow far away from the wall.

By examining the behaviour close to the wall we can further develop Equation (5.3). First recall that applying a no slip condition and the continuity equation leads in a fully developed flow to the following asymptotic behaviour of velocities close to the wall:

$$u_1 \sim x_2, \qquad u_2 \sim x_2^2, \qquad u_3 \sim x_2. \tag{5.8}$$

These approximations lead to $\overline{s_{ij} s_{ij}} \sim \mathcal{O}(1)$. Which remains in contradiction with the observation that in the vicinity of the wall fluctuating components vanish and only the mean flow contributes to the rate of strain. It is therefore concluded that the inequality in Equation (5.3) must be strict.

Furthermore, the expansion of the expression for the rate of strain magnitude variance $\overline{s_{ij} s_{ij}}$:

$$2\overline{s_{ij} s_{ij}} = \overline{\frac{\partial u_i}{\partial x_j}\frac{\partial u_i}{\partial x_j}} - \frac{\partial^2 \overline{u_i u_j}}{\partial x_i \partial x_j}. \tag{5.9}$$

shows that we are dealing with two quantities that are not known *a priori*. We are facing here a problem similar to the problem of the closure of the RANS equations. If we adopt a turbulence model for Reynolds stress the second term on the right hand side of Equation (5.9) becomes known, since it is the second derivative of the Reynolds stress. However the first term remains an unknown and requires further investigation.

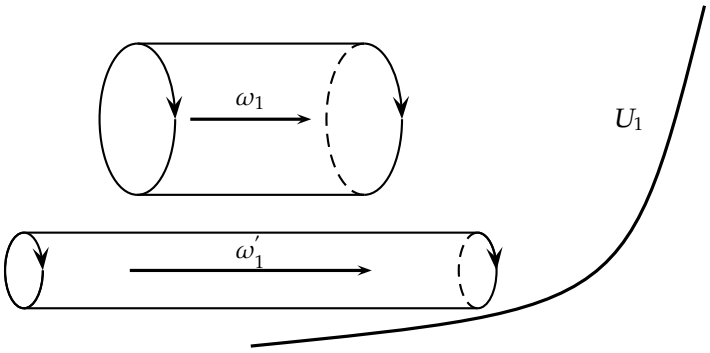

Figure 5.1: Vortex stretching phenomena that occurs in the in the presence of shear.

5.1.1 Relation to vorticity

Let us introduce fluctuating vorticity as:

$$\zeta_i = \varepsilon_{ijk} \frac{\partial u_k}{\partial x_j}, \tag{5.10}$$

where ε_{ijk} is a Levi-Civita symbol and ζ_i is the i'th component of vorticity and should not be confused with specific disspation ω known from the k-ω model.

One of the characteristic features of turbulence is a phenomenon called vortex stretching. In the language of statistical turbulence it can be expressed in the following way: the contribution to the Reynolds stress terms is highest in the regions of the flow that have the vorticity aligned with the mean strain rate. This effect can be tentatively explained by the conservation of angular momentum. Imagine a rotating filament of fluid. If the axis of the filament is aligned with positive shear rate then the filament will stretch in the direction normal to the basis and with the radius of the basis decreasing. To preserve the angular momentum the vorticity must increase. Similarly, the vorticity will decrease if the axis is aligned with negative shear rate. A sketch is provided on Figure 5.1.

For isotropic turbulence Tennekes and Lumley (1972) show:

$$\epsilon = 2\nu\overline{s_{ij}s_{ij}} = 15\nu\overline{\left(\frac{\partial u_1}{\partial x_1}\right)^2}. \tag{5.11}$$

For this flow the Taylor microscale can be defined[1] as:

$$\overline{\left(\frac{\partial u_1}{\partial x_1}\right)^2} = \frac{u^2}{\lambda^2}. \tag{5.12}$$

Moreover, according to Hinze (1959) we can write the following relationship for turbulent dissipation:

$$\epsilon = 15\nu\frac{u^2}{\lambda^2}. \tag{5.13}$$

Through a simplified energy budget expressed by Equation (5.4) and with the scaling assumptions $S_{ij} \sim u/l$ and $u_i \sim u$, we can relate the Taylor microscale to the integral scale l:

$$A\frac{u^3}{l} = 15\nu\frac{u^2}{\lambda^2}. \tag{5.14}$$

And then the ratio of these two lengthscales is:

$$\frac{\lambda}{l} = \left(\frac{15}{A}\right)^{\frac{1}{2}} \mathrm{Re}_l^{-1/2} = \frac{15}{A}\mathrm{Re}_\lambda^{-1} \tag{5.15}$$

Where Reynolds number the subscript denotes the length scale that the number is based on.

Defining the rotation tensor as the anti-symmetric part of the velocity gradient:

$$r_{ij} = \frac{1}{2}\left(\frac{\partial u_j}{\partial x_i} - \frac{\partial u_i}{\partial x_j}\right), \tag{5.16}$$

the vorticity magnitude and strain rate magnitude can be linked with following relations:

$$\overline{\zeta_i\zeta_i} = 2\overline{r_{ij}r_{ij}}\,, \tag{5.17}$$

$$\overline{s_{ij}s_{ij}} - \overline{r_{ij}r_{ij}} = \frac{\partial^2}{\partial x_i \partial x_j}\left(\overline{u_i u_j}\right). \tag{5.18}$$

Now we will use the scaling properties in Equations (5.11) and (5.12). The first term on the left hand side of Equation (5.18) is of the order $\mathcal{O}(u^2/\lambda^2)$. The term on the right hand side of the same equation is of the order $\mathcal{O}(u^2/l^2)$. According to Equation (5.15) this means that $\overline{s_{ij}s_{ij}}$ dominates in Equation (5.18) and therefore $\overline{r_{ij}r_{ij}}$ must be of the same order. Together with Equation (5.17) this means that:

$$\overline{\zeta_j\zeta_j} \sim 2\overline{s_{ij}s_{ij}}\,. \tag{5.19}$$

[1]The general definition of Taylor lengthscale is given as the reciprocal of the square root of the second derivative of the longitudinal integral length-scale at the origin.

Which means that for large Reynolds number and for isotropic turbulence the unknown shear rates in Equation (5.3) scale as fluctuating vorticity magnitude.

5.2 Probabilisitc information

Even if the above considerations give an accurate model of the rate of strain it does not necessarily lead to an accurate estimate of mean viscosity. This is caused by the non-linear relationship between rate of strain and viscosity.

Mathematically the problem can be stated as follows: if one random variable is a function of the other, what is the probability distribution of the former if the distribution of the latter as well as the function itself are known. This problem has no definite answer in general, but many specific results have been proven.

Monin and Yaglom (1975) argue that under certain self-similarity assumptions of a high-Reynolds number flow, turbulence dissipation in an inertial region is a random variable with a log-normal distribution. Their reasoning applies for any non-negative quantity related to small-scale and locally isotropic motions of turbulent flow.

If the rate of strain was a random variable with a log-normal distribution then its probability density function would be expressed as follows:

$$f_{\mathrm{P}}(\dot{\gamma}) = \frac{1}{\dot{\gamma}\sigma\sqrt{2\pi}} \exp\left\{\frac{1}{2}\left(\frac{\ln\dot{\gamma} - M}{\sigma}\right)^2\right\}, \tag{5.20}$$

where M and σ are parameters of the distribution. It can be verified that for each real valued power m, the following holds true:

$$\int_0^\infty \dot{\gamma}^m f_{\mathrm{P}}(\dot{\gamma})\,\mathrm{d}\dot{\gamma} = \exp\left(mM + \frac{m^2\sigma^2}{2}\right). \tag{5.21}$$

In other words, every moment can be expressed in terms of M and σ. The former can be factored out and expressed in terms of the first moment. In the case of Herschel–Bulkley mean viscosity one can observe that all the components are powers of rate of strain magnitude giving us:

$$\begin{aligned}\overline{\nu} =& \int_0^\infty \nu(\dot{\gamma}) f_{\mathrm{P}}(\dot{\gamma})\,\mathrm{d}\gamma = \int_0^\infty \tau_Y\dot{\gamma} + K\left(\dot{\gamma}\right)^{(n-1)}\,\mathrm{d}\dot{\gamma} = \\ =& \tau_Y\overline{\dot{\gamma}}^{-1} + K\overline{\dot{\gamma}}^{(n-1)} \exp\left(\frac{\sigma^2}{2}(n-2)(n-1)\right)\end{aligned} \tag{5.22}$$

The result in Equation (5.22) is valid only when we assume that the logarithm of $\dot{\gamma}$ has a normal distribution. This section sketches a proof supporting this assertion.

To prove the assertion expressed by Equation (5.20) let us assume that the flow in question can be enclosed in volume V_0 which has a length-scale of L_0. Let $\dot{\gamma}$ be a random variable defined for each point in space and for any volume V let us introduce the following spatial average:

$$\dot{\gamma}_V = \frac{1}{|V|} \int_V \dot{\gamma} \, \mathrm{d}V. \tag{5.23}$$

Note that this average is itself a random variable that depends upon the position in space.

Let us denote two volumes V' and V''. Both volumes have corresponding length-scales: L' and L''. Moreover, the volumes and length-scales must satisfy $V' \supset V''$, $L \gg L' > L'' \gg \eta$, where η is the Kolmogorov scale and L is a characteristic length of the whole domain. In other words one volume contains the other and their length-scales are much larger than Kolmogorov scale but much smaller than the scale of the problem. For such volumes the assumption, which is often called the condition of scale similarity of turbulent fields (see Gurvich (1967); Novikov (1969)), states that if the Reynolds number is large the following holds true:

$$f_{\mathrm{P}}\left(\frac{\dot{\gamma}_{V'}}{\dot{\gamma}_V}\right) \sim \frac{L'}{L} \tag{5.24}$$

$$f_{\mathrm{P}}\left(\frac{\dot{\gamma}_{V''}}{\dot{\gamma}_{V'}}\frac{\dot{\gamma}_{V'}}{\dot{\gamma}_V}\right) = f_{\mathrm{P}}\left(\frac{\dot{\gamma}_{V''}}{\dot{\gamma}_{V'}}\right) f_{\mathrm{P}}\left(\frac{\dot{\gamma}_{V'}}{\dot{\gamma}_V}\right). \tag{5.25}$$

In other words the distribution of the ratio depends only on the ratio of scales and the ratios are independent. From these assumptions one can easily arrive at:

$$f_{\mathrm{P}}\left(\frac{\dot{\gamma}_{V''}}{\dot{\gamma}_{V'}}\right) \sim \frac{L''}{L'}. \tag{5.26}$$

Now let us take a sequence of volumes such that $V_0 \supset V_1 \supset \ldots \supset V_m \supset \ldots$ with corresponding length-scales $L_0 > L_1 > \ldots > L_m > \ldots$ and adopt the following notation:

$$\dot{\gamma}_m = \dot{\gamma}_{V_m} \qquad\qquad R_m = \dot{\gamma}_m / \dot{\gamma}_{m-1} \tag{5.27}$$

First, observe that the ratios of averages R_m are independently distributed. Using the above hypothesis we can write:

$$\overline{R_{m+1} R_m} \sim \overline{\frac{L_{m+1}}{L_m}\frac{L_m}{L_{m-1}}} = \overline{\frac{L_{m+1}}{L_m}}\;\overline{\frac{L_m}{L_{m-1}}} \sim \overline{R}_{m+1}\,\overline{R}_m \tag{5.28}$$

which proves the independence of R_m and R_{m+1}. The central equality is trivial since the length scale ratios are simply constants.
The next step is to observe that each average can be expressed in terms of ratios:

$$\dot{\gamma}_m = \dot{\gamma}_0 R_1 R_2 \dots R_{m-1} \tag{5.29}$$

Taking the logarithm of the above expression, setting each $L_i/L_{i-1} = \text{const}$ we get

$$\ln \frac{\dot{\gamma}_m}{\dot{\gamma}_0} = \ln R_1 + \ln R_2 + \dots \ln R_{m-1}. \tag{5.30}$$

The sum on the right hand side according to our hypothesis comprises mostly terms that are independently, identically distributed random variables. Now the central limit theorem can be invoked and leads to:

$$\ln \frac{\dot{\gamma}_m}{\dot{\gamma}_0} \sim \mathcal{N}(M_m, \sigma_m). \tag{5.31}$$

The relation is only approximate since there are terms in the sum of the right hand side of Equation (5.30) for which the conditions of the similarity hypothesis do not hold. The influence of these terms is assumed to be confined to the parameters of the distribution since they are either very small or constant in a given volume.

5.3 Analysis of DNS data

The DNS data from Rudman et al. (2004) have been chosen for investigation of the relative magnitude and the hypothesis about the log-normal distribution. The data has been obtained through a private communication. The level of detail that can be achieved in DNS flow was the main reason for choosing this data set. The typical data set contained 384 cross-sections with each cross-section comprising 12705 grid points refined near the wall. The grid is presented on Figure 5.2.
Moreover, the Rudman et al. data consists of shear-thinning as well as yield stress fluids. The investigation of the former has been undertaken by Pinho (2003) and resulted in a development of a zeroth order model for power-law fluids. This study extends his work into yield stress fluids.
All the values were normalised by bulk velocity, density and pipe diameter of the pipe. The data were transformed to polar coordinates and interpolated to a radial grid to facilitate the construction of radial statistics. The interpolation was performed

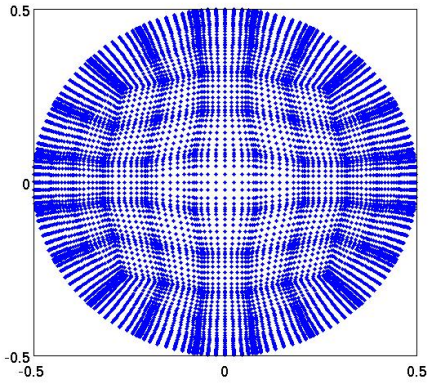

Figure 5.2: DNS grid by Rudman et al. (2004).

using a Delaunay triangulation (de Berg et al. (2000)). Delaunay triangulation is a triangulation in which every triangle circumscribed circle does not contain in its interior any other point of the triangulation. This allows the interpolation of values within each triangle as a convex combination. This procedure is implemented in the MATLAB in-built functions.

After data transformations the rates of strain have been obtained from velocity field. Two types of this quantity are used here: rate of strain based on mean velocity field and rate of strain based on instantaneous velocity field. In polar coordinates the rate of strain tensor has the following form:

$$\hat{\boldsymbol{S}} = \begin{pmatrix} \frac{\partial U_1}{\partial r} & \frac{1}{2}\left(r\frac{\partial U_2/r}{\partial r} + \frac{1}{r}\frac{\partial U_1}{\partial \theta}\right) & \frac{1}{2}\left(\frac{\partial U_3}{\partial r} + \frac{\partial U_1}{\partial z}\right) \\ \frac{1}{2}\left(r\frac{\partial U_2/r}{\partial r} + \frac{1}{r}\frac{\partial U_1}{\partial \theta}\right) & \frac{1}{r}\frac{\partial U_2}{\partial \theta} + \frac{U_2}{r} & \frac{1}{2}\left(\frac{\partial U_2}{\partial z} + \frac{1}{r}\frac{\partial U_3}{\partial \theta}\right) \\ \frac{1}{2}\left(\frac{\partial U_3}{\partial r} + \frac{\partial U_1}{\partial z}\right) & \frac{1}{2}\left(\frac{\partial U_2}{\partial z} + \frac{1}{r}\frac{\partial U_3}{\partial \theta}\right) & \frac{\partial U_3}{\partial z} \end{pmatrix} \tag{5.32}$$

5.3.1 Comparison of viscosity fields

The viscosity field was computed by estimating the rate of strain from the velocity field and substituting it into the Herschel–Bulkley fluid constitutive law with rheological parameters taken from Rudman et al. (2004). Subsequently, it was compared with the viscosity field supplied with the data. The field has been averaged over all angles and over all cross-sections to obtain the graph presented in Figure 5.3. It can be seen that the viscosity field obtained from interpolation agrees with the data close to the wall. A

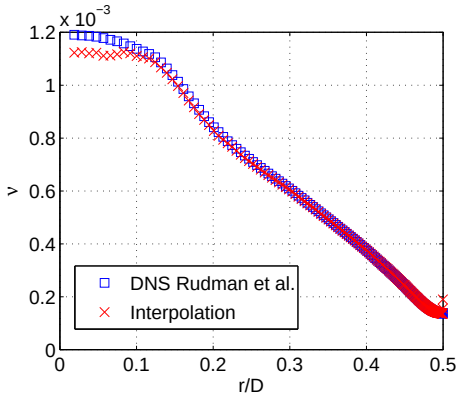

Figure 5.3: The radial interpolation of viscosity field.

small discrepancy is observed towards the centre of the pipeline. It is stipulated that the agreement is correlated to the grid structure which is coarser at the centre. Also, close to the wall the mesh from Rudman et al. (2004) resembles a radial grid whilst further away from the wall it changes into rectangular blocks.

5.3.2 Rate of strain magnitude

Figure 5.4 presents a typical cross-section showing magnitudes of the rate of strain. Obviously, the values based on instantaneous rates show much bigger variation. To compare these two data sets a third snapshot was constructed showing the ratio of instantaneous to mean velocity based rate of strain. The simulations reveal the existence of regions where the rate of strain of instantaneous velocity field is at least an order of magnitude higher than the rate of strain of mean velocity field. These regions are formed at the distance from the wall that corresponds to a peak turbulence intensity region. Then the region moves towards the centre of the pipeline where it remains for a short time until it dissipates completely. These results present only the snapshots for yield stress fluids, but for shear-thinning fluids similar behaviour was observed.

This picture shows a qualitative similarity to the vortex stretching phenomena depicted in Figure 5.1. The vortices that are formed in the presence of the mean velocity gradient travel towards the pipe centre, expanding and diminishing in magnitude. This additional motion causes the local rate of strain to increase, showing that in the instantaneous picture the mean rate of strain can be increased by coherent structures of

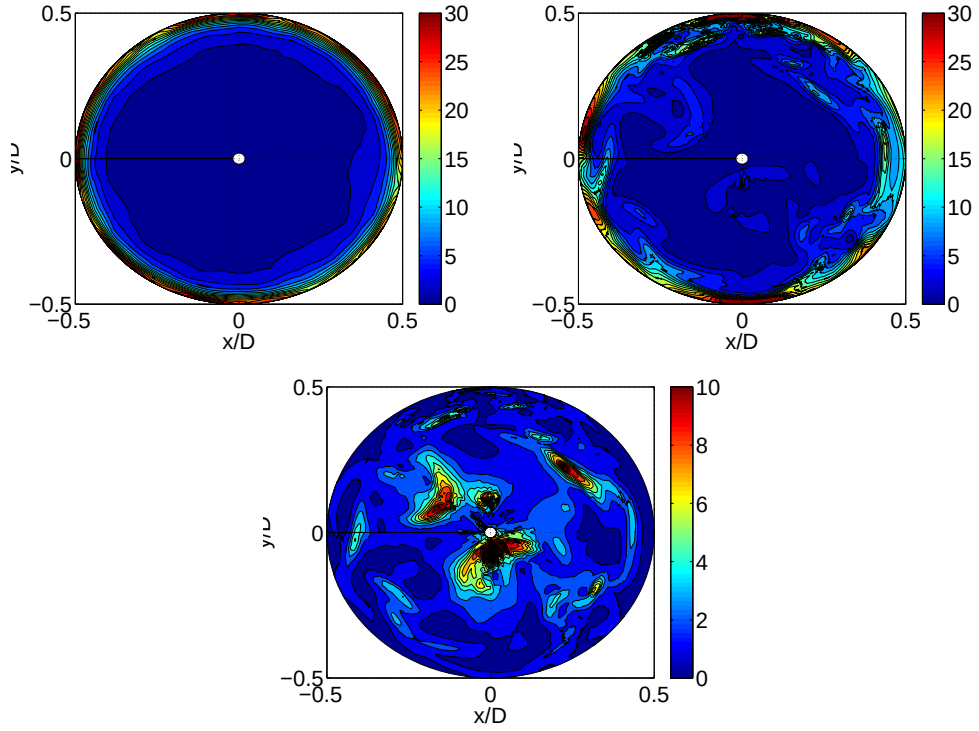

Figure 5.4: Top: rate of strain based on mean (left) and rate of strain based on instantaneous velocity (right). Bottom: the ratio of instantaneous to mean rate of strain. Reg regions show signficant differences between shear rate caused by mean and fluctuating components.

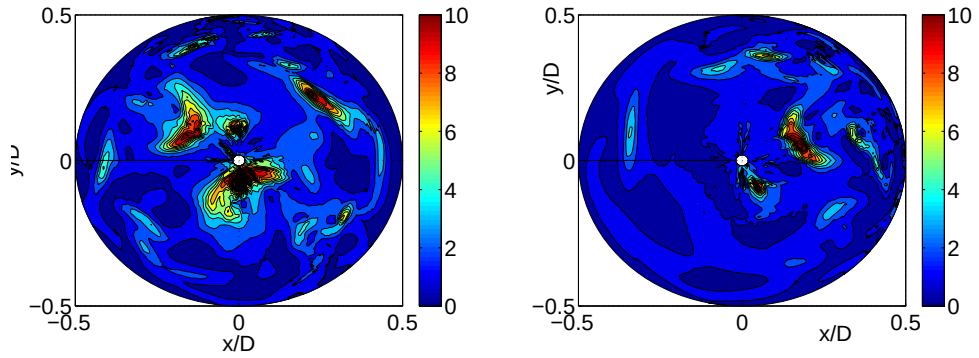

Figure 5.5: Ratios of instantaneous to mean rate of strain for $\tau_Y = 0.28$ (Left) $\tau_Y = 0.85$ (Right).

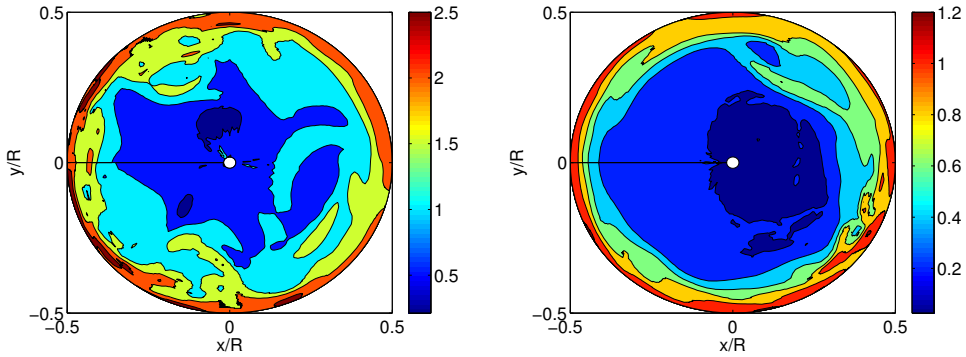

Figure 5.6: The logarithm of shear-stress normalised by yield stress for $\tau_Y = 0.28$ (Left) $\tau_Y = 0.85$ (Right).

turbulence.

To investigate the matter further we decided to gauge the effect of yield stress. A second dataset with a yield stress four times larger has been examined and the resulting ratios are compared on Figure 5.5. The evolution of shear regions at a higher rate is greatly attenuated by a much faster dissipation away from the wall, which is in agreement with Rudman et al. (2004). The frequency of occurrence of these regions is of the same magnitude which suggests that turbulence in a non-Newtonian fluid remains a wall phenomenon.

5.3.3 Yield stress and unyielded regions

As outlined above the higher yield stress attenuates turbulence in the core flow. Moreover, shear stress decreases towards the centre of the pipe. This means that at a certain point it will pass the yield threshold and unyielded regions may form. In GNF the viscosity is a function of shear rate tensor invariants. Since the viscosity and rate of strain fields have been already calculated it was straightforward to calculate shear stress.

Figure 5.6 presents a typical snapshot of shear-stress in a cross-section. The shear-stress has been normalised with yield stress so the value of one corresponds to an unyielded region. We can observe a significant difference between the two presented cases. When the yield stress is higher there is a large region of shear stress values close or exactly equal to one. For lower values of yield threshold the regions tend to be smaller and are

confined only to the centre of the pipeline, appearing and disappearing in a transient fashion.

5.3.4 Statistical hypothesis testing

Rigorous hypothesis testing requires tools of statistical inference. In particular a null hypothesis must be identified and tested with an arbitrary significance level. This methodology leads to four possible situations:

1. Failing to reject a true null hypothesis.
2. Rejecting a true null hypothesis – this is called Type I error or false positive.
3. Failing to reject a false null hypothesis – this is called Type II error or false negative.
4. Rejecting a false null hypothesis.

With this distinction, statistical inference becomes a particular type of constrained optimization problem. We want to minimize the probability of Type II error with a specified probability of Type I error. The specification of the probability of Type I error is the choice of significance level:

$$\Pr(A|H_0) = 1 - \alpha \tag{5.33}$$

where $\Pr(\cdot|\cdot)$ is the conditional probability, A is the event observed, H_0 is the null hypothesis and $\alpha \in [0, 1]$ is the level of significance. We will adopt here $\alpha = 0.05$. Therefore, the test will treat as extraordinary all the values that under the null hypothesis comprise the 5% of possible realisations. If such a value appears in the test the null hypothesis is rejected. Increasing the level of significance is equivalent to reducing the probability that the result occurred by chance.
A closely related concept is the confidence interval. The confidence interval is an interval which contains the values of the random variable with a specified probability given the null hypothesis is true.
Firstly, we investigate the hypothesis about the difference of means calculated from mean rate of strain and from instantaneous rate of strain. To this end we adopt the

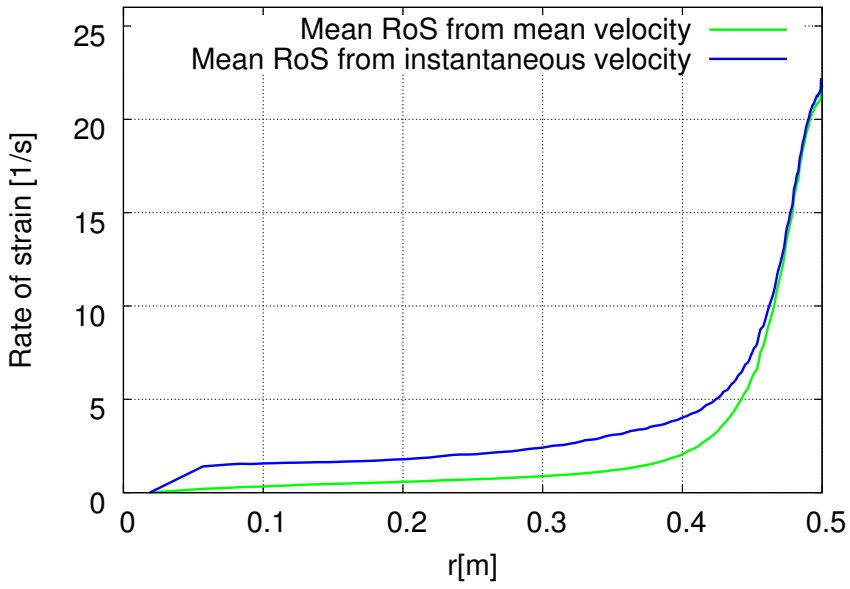

Figure 5.7: The difference between the rate of strain (RoS) calculated from the mean velocity and instantaneous velocity, averaged over all radial points.

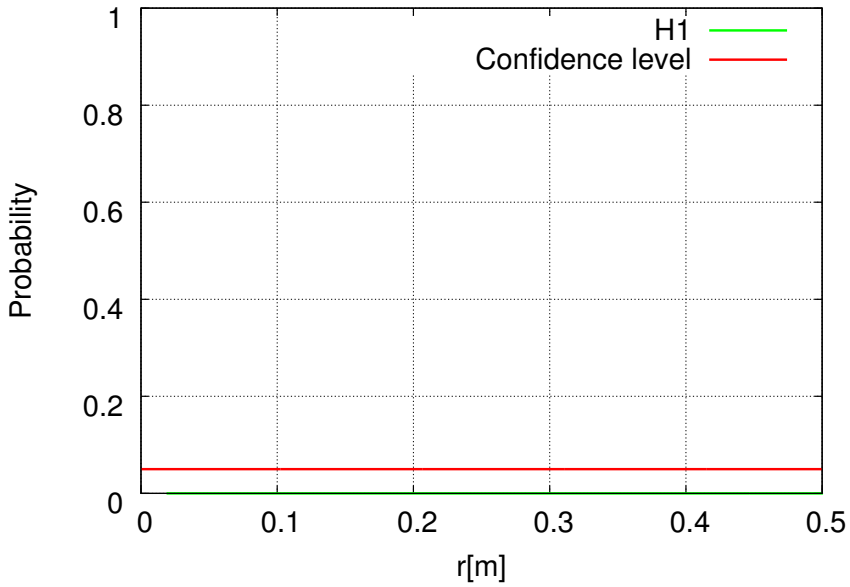

Figure 5.8: p-values for the equal mean hypothesis.

equality of means as the null hypothesis. To establish the equality of means in two samples a modified t-Student test is used.

$$t = \frac{\overline{X}_1 - \overline{X}_2}{\sqrt{\frac{1}{n}\left(\mathrm{Var}(X_1) + \mathrm{Var}(X_2)\right)}}, \tag{5.34}$$

where $\overline{X}$ is the sample mean, n is the population size and $\mathrm{Var}(\cdot)$ is the variance. Under the null hypothesis this statistic will have a t-distribution with the degrees of freedom equal to $2n - 2$. Subsequently a two tailed test is performed. A two tailed tests calculates:

$$p = \Pr(|T| > t), \tag{5.35}$$

where T is the random variable following the t-distribution as described above. If p is below the level of significance the null hypothesis is rejected.

Figure 5.7 shows the means calculated from the instantaneous rate of strain and mean rate of strain, for the power-law fluid in Rudman et al. (2004). The estimates exhibit a discrepancy that is especially pronounced around the centre of the pipe but decreases as the wall is approached. It important to observe that the systematic difference remains close to the wall, although it is decreased in magnitude. The p-value calculated from Equation (5.35) and displayed on Figure 5.8 confirms this visual observation as the value never surpasses the 0.05 significance level. The large population size allows us to detect even the small discrepancy close to the wall.

The second hypothesis was the log normality of the rate of strain calculated from instantaneous data. Therefore, the logarithm of the values should have approximately normal distributions. This hypothesis is adopted directly as the null hypothesis. In the literature many tests of data normality were proposed. The test used in this study was proposed by D'Agostino et al. (1990) and it uses the fact that the sample skewness and sample kurtosis must have values of zero and three respectively for normally distributed populations.

More specifically, the skewness and kurtosis are defined in terms of central moments:

$$\gamma_1 = \frac{\mathcal{E}\left(X - \mathcal{E}X\right)^3}{\left(\mathcal{E}\left(X - \mathcal{E}X\right)^2\right)^{3/2}}, \tag{5.36}$$

$$\gamma_2 = \frac{\mathcal{E}\left(X - \mathcal{E}X\right)^4}{\left(\mathcal{E}\left(X - \mathcal{E}X\right)^2\right)^2}, \tag{5.37}$$

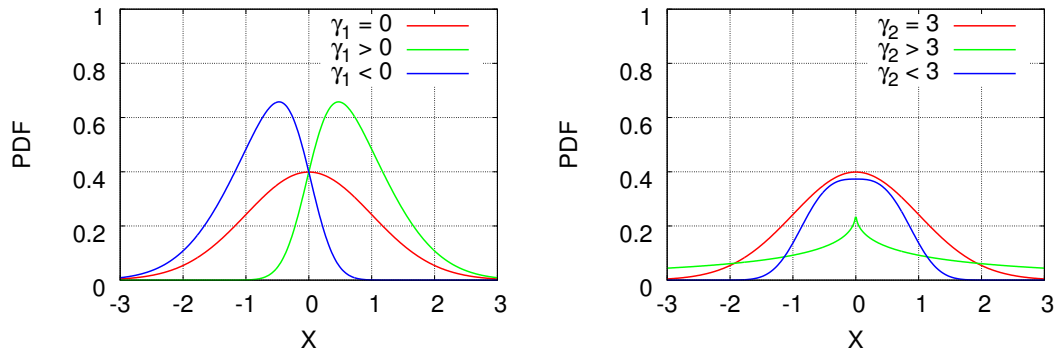

Figure 5.9: Skewness (left) and kurtosis (right) of the probability distribution.

where $\mathcal{E}$ denotes expected value. The geometrical representations of these concepts are shown on Figure 5.9. If X is normally distributed then we have:

$$\gamma_1 = 0, \quad \gamma_2 = 3. \tag{5.38}$$

The sample equivalents are:

$$g_1 = \frac{m_3}{m_2^{3/2}}, \tag{5.39}$$

$$g_2 = \frac{m_4}{m_2^2}, \tag{5.40}$$

$$m_k = \frac{1}{n}\sum_{i=1}^{n}\left(X_i - \overline{X}\right)^k \tag{5.41}$$

Both, g_1 and g_2 are asymptotically normal. Therefore, it is possible to construct the confidence interval for these values and compare it against the values obtained experimentally. Unfortunately in practice the rate of convergence is very slow and consequently requires a prohibitively large population size.

D'Agostino (1970) and Anscombe and Glynn (1983) propose transformations of these sample quantities in such a way that the transformed quantities have an increased rate of convergence to the normal distribution. These formulae are a good approximation for sample sizes larger than twenty. Using these formulae the test for skewness can be

expressed as follows:

$$\mathcal{Y} = \sqrt{g_1}\left(\frac{(n+1)\,(n+3)}{6\,(n-2)}\right)^{\frac{1}{2}}, \tag{5.42}$$

$$\gamma_2(\sqrt{g_1}) = \frac{3(n^2+27n-70)(n+1)(n+3)}{(n-2)(n+5)(n+7)(n+9)}, \tag{5.43}$$

$$\mathcal{W}^2 = -1 + \left(2\left(\gamma_2(\sqrt{g_1})-1\right)\right)^{\frac{1}{2}}, \tag{5.44}$$

$$\mathcal{X} = \left(\frac{2}{\mathcal{W}^2-1}\right)^{\frac{1}{2}}, \tag{5.45}$$

$$Z(g_1) = \delta \ln\left(\frac{Y}{\mathcal{X}} + \left(\left(\frac{Y}{\mathcal{X}}\right)^2 + 1\right)\right), \tag{5.46}$$

where $Z(g_1)$ has a normal distribution. The test for kurtosis is expressed by:

$$\mathcal{E}(g_2) = \frac{3\,(n-1)}{n+1}, \tag{5.47}$$

$$\mathrm{Var}(g_2) = \frac{24n\,(n-2)\,(n-3)}{(n+1)^2\,(n+3)\,(n+5)}, \tag{5.48}$$

$$\sqrt{\gamma_1(g_2)} = \frac{6(n^2-5n+2)}{(n+7)(n+9)}\sqrt{\frac{6(n+3)(n+5)}{n(n-2)(n-3)}}, \tag{5.49}$$

$$\mathcal{A} = 6 + \frac{8}{\sqrt{\gamma_1(g_2)}}\left(\frac{2}{\sqrt{\gamma_1(g_2)}} + \sqrt{\left(1+\frac{4}{\gamma_1(g_2)}\right)}\right), \tag{5.50}$$

$$Z(g_2) = \sqrt{\frac{9\mathcal{A}}{2}}\left(\left(1-\frac{2}{9\mathcal{A}}\right) - \left(\frac{1-2/\mathcal{A}}{1+\frac{g_2-\mathcal{E}(g_2)}{\sqrt{\mathrm{Var}(g_2)}}\sqrt{2/\left(\mathcal{A}-4\right)}}\right)^{1/3}\right). \tag{5.51}$$

Finally, we construct an omnibus test i.e. a test which simultaneously verifies skewness and kurtosis:

$$K^2 = Z^2\left(g_1\right) + Z^2\left(g_2\right). \tag{5.52}$$

Since both components have a normal distribution the sum have has a χ-squared distribution with two degrees of freedom. This allows us to construct a simple one sided test that gives the probability of being simultaneously away from normal distribution skewness and kurtosis.

Figure 5.10 shows the p-values for the log normality hypothesis. It can be seen that the data fails this test for most of the radial points. This leads to rejection of the null

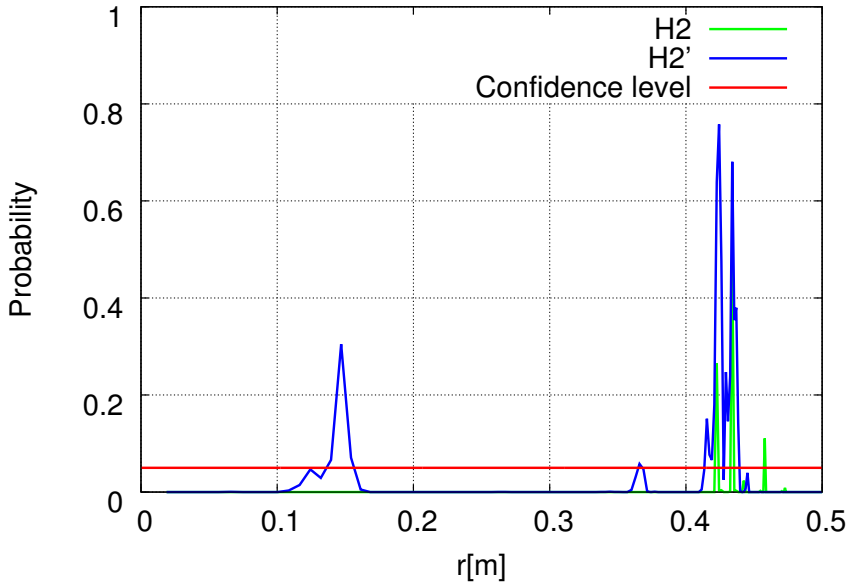

Figure 5.10: The p–values associated with hypothesis of log-normality of instantaneous rate of strain (H2) and normality of mean rate of strain (H2').

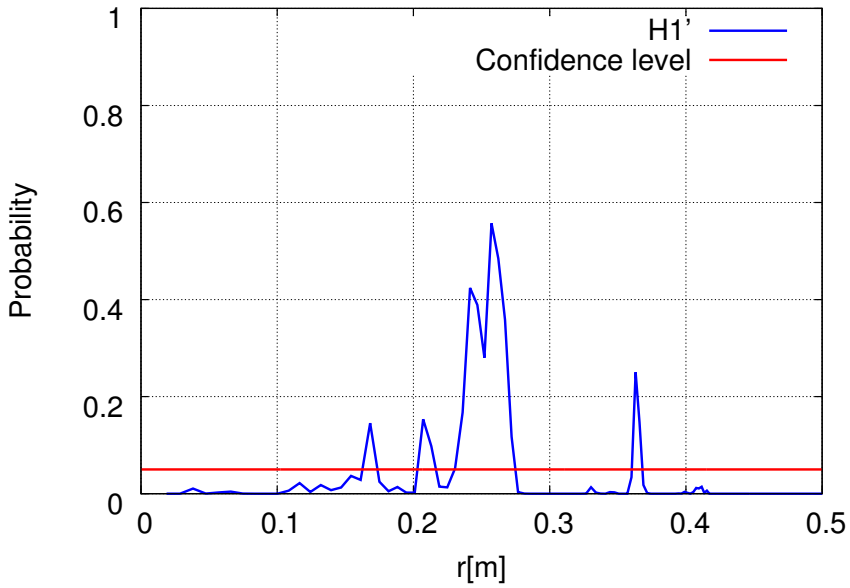

Figure 5.11: The p–values associated with hypothesis of log-normality of the fluctuating rate of strain H2'.

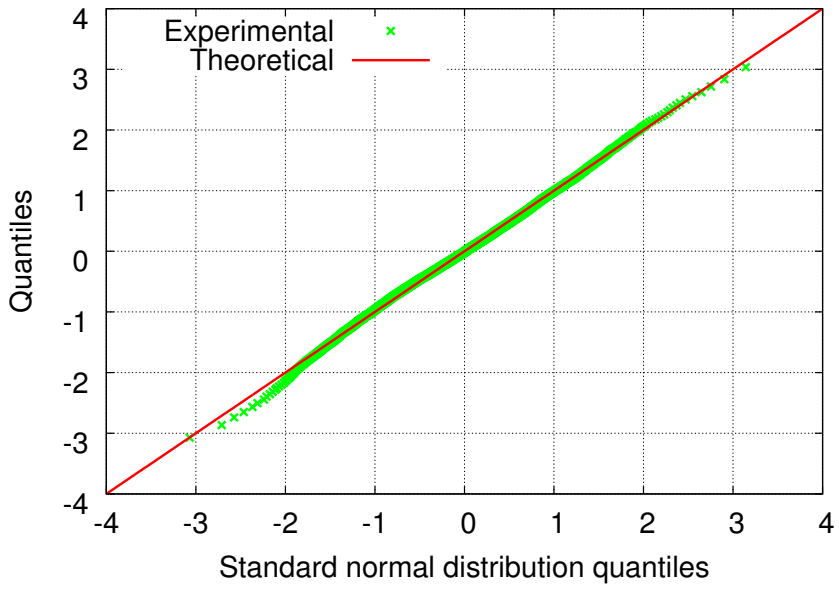

Figure 5.12: The QQ plot for the one of the fitted histograms.

hypothesis. Moreover the normality of mean strain rate has been also assessed and is denoted on the diagram as H2'. The normal distribution of the mean estimate fails in an even larger regions and therefore must be deemed as coincidental. The log-normality does not fail in some region, but this result is not repeated with the Herschel–Bulkley data where log-normality assumption failed for every radial point.

If the hypothesis H1 was modified to pertain only to the fluctuating part of the rate of strain then the similar analysis would lead to Figure 5.11. The fluctuating part of the rate of strain does not fail the log-normality hypothesis in a large region away from the wall and this region was reproduced for both Herschel–Bulkley fluids. This shows that there may be a region where the log-normality of the fluctuating strain is an accurate description of the flow.

For the radial points that did not fail the test histograms, QQ plots were constructed. QQ plots are visual tests of normality which plot the quantiles of the standard normal distribution against the sample quantiles. QQ plots are a more general tool since they allow us to compare any two distributions and the equivalence of quantiles is the equivalence of distributions. If the distributions are the same, the values should align on the line.

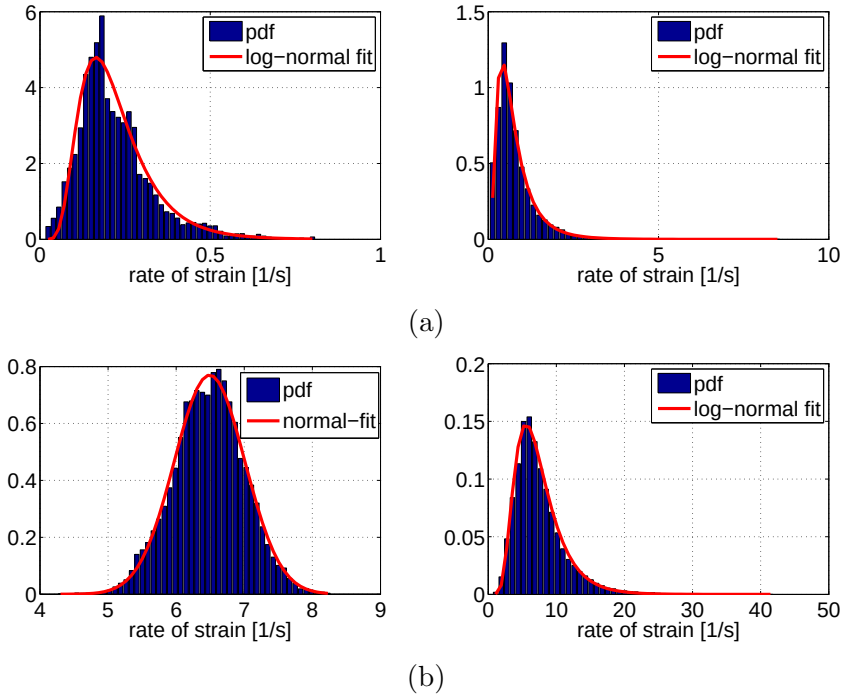

Figure 5.13: Probability density functions of strain rates of mean (left) and instantaneous (right) fields. (Rudman et al. (2004)).

For the purpose of histogram construction, values were collected for one radial point over all angles and over all cross-sections. The values of the histograms were normalised with respect to the area under the curve, hence giving an approximation of Probability Density Function (PDF). For these points the log-normal distribution approximates accurately the population, but since the result cannot be generalised to the bulk of the flow the log-normality will not be considered in further investigations.

5.4 CFD two-equation models

In this chapter the model based on the previous consideration is proposed and compared against other models for non-Newtonian fluid turbulence.

To the best of the author's knowledge the first study in the area of CFD modelling has been undertaken by Malin (1997) who incorporated non-Newtonian properties into low-Reynolds number models, showing first that a standard version of a Lam–Bremhorst low-Reynolds number was inadequate to describe velocity profiles and friction factors.

He introduced a simple modification of the damping function

$$f_\mu = [1 - \exp(-0.0165\mathrm{Re}_w)/n^{1/4}]^2/(1 + 20.5/\mathrm{Re}_t). \tag{5.53}$$

where n corresponds to power-law index in the consitutive law of Ostwald–de Waele fluid. Compare this form with Equation (4.39).

The model has been shown to improve friction factor and velocity profiles predictions although in the latter case the accuracy of the velocity profile result cannot be established easily because the results are plotted in physical coordinates and therefore the thin boundary layer is not visible clearly. As expected the model was able to reproduce laminar power-law velocity profiles for sufficiently low Reynolds numbers. The model was also tested against Herschel–Bulkley fluids. The runs reported in Malin (1998) prove to be sufficiently accurate in a number of flow cases. This model is unable to predict any of the elastic, unsteady effects and therefore it will not exhibit turbulent drag reduction.

Pinho (2003) develops a $k - \epsilon$ model by introducing a decomposition of viscosity into mean and fluctuating component in the same manner as turbulence theory decomposes velocities:

$$\nu = \overline{\nu} + \nu'. \tag{5.54}$$

With this assumption the derivation of kinetic energy equation is conducted. Then, based on a constitutive equation that is a modification of a GNF fluid to incorporate elastic effects an estimate for mean viscosity is given. Subsequently, an order of magnitude analysis eliminates most of the equation terms and the eventual transport equation for k and ϵ, based on low Reynolds number from Nagano and Hishida (1987) simplified to a channel flow, is given by:

$$0 = \frac{\partial}{\partial x_2}\left[\frac{\nu_T}{\sigma_k}\frac{\partial k}{\partial x_2} + \overline{\nu}\frac{\partial k}{\partial x_2}\right] - \overline{u_1 u_2}\frac{\partial \overline{u}}{\partial x_2} - \epsilon \tag{5.55}$$

$$0 = \frac{\partial}{\partial x_2}\left[\left(\overline{\nu} + \frac{\nu_T}{\sigma_\epsilon}\right)\frac{\partial \epsilon}{\partial x_2}\right] + f_1 C_{\epsilon 1}\frac{\epsilon}{k}C_\nu\frac{k^2}{\epsilon}\left(\frac{\partial \overline{u}}{\partial x_2}\right)^2 + C_{\epsilon 3}\frac{\epsilon}{\overline{\nu}}\frac{\partial \overline{\nu}}{\partial t} + \\ + C_{\epsilon 4}\frac{\nu_T}{\sigma_\epsilon \overline{\nu}}\frac{\partial \epsilon}{\partial x_2}\frac{\partial \overline{\nu}}{\partial x_2} \tag{5.56}$$

Moreover the classical turbulent viscosity damping function f_μ is decomposed into viscometric damping and elongation viscosity damping:

$$f_\mu = f_{\mu v} f_{\mu e} \tag{5.57}$$

The damping functions are derived in a similar way to Van Driest function and are given by:

$$f_{\mu v} = 1 - \left[1 + \left|\frac{1-n}{1+n} y^{+}\right|\right]^{|(1+n)/(1-n)|(1/A^{+})} \tag{5.58}$$

$$f_{\mu e} = 1 - \left[1 + \left|\frac{p-1}{3-p} y^{+}\right| C^{(1-p)/(2-p)}\right]^{-|(3-p)/(p-1)|(1/A^{+})} \tag{5.59}$$

$$\tag{5.60}$$

where p is a power index that accounts for elongation viscosity properties in the GNF constitutive equation

Friction factors and velocity profiles correlate favourably with experimental and previous computational data. However kinetic energy and dissipation are not quantitatively correct. Only the qualitative shift of turbulence production peak value was observed. The model has been recommended for low values of turbulence intensities.

A Finitely Extensive Nonlinear Elastic with Peterlin's approximation (FENE-P) is a molecular model that results in a constitutive equation of the Metzner–White type. So far it has been mostly used in DNS simulations but recently an attempt by Pinho et al. (2008) has proved to be successful for a low turbulent Reynold numbers. The model is based on and validated against recent DNS data. A similar derivation of damping function and model equations has been conducted but its presentation will be omitted since this study does not deal with drag reducing fluids.

5.4.1 Results

The main aim of the computational studies undertaken here was to predict the flow rate given the pressure gradient. For the experimental and DNS data presented here the latter is not readily available and has to be estimated from the wall shear-stress that is either reported Escudier et al. (2005) or can be extracted from the data Pinho (2003); Rudman et al. (2004).

Since the rate of strain at the wall and the rheological properties were given, it was possible to calculate the pressure gradient (see Pope (2000)):

$$\frac{\partial p}{\partial x} = -\frac{2}{R}\tau_w. \tag{5.61}$$

Two types of meshes were generated in GAMBIT. Both of them were 2D with axisymmetric boundary conditions imposed. The first mesh had dimensions corresponding to

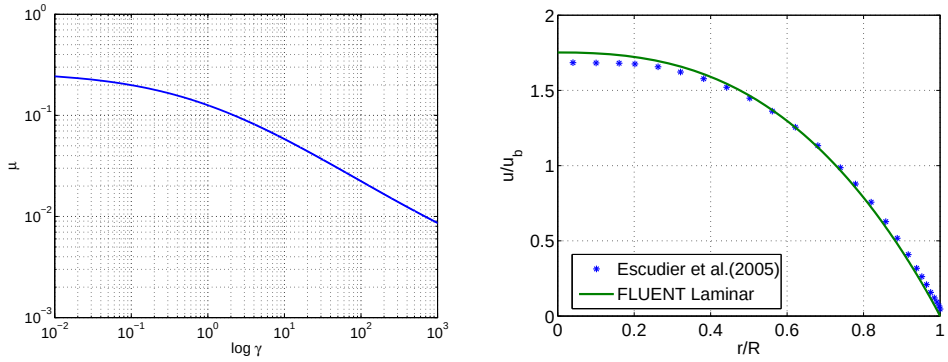

Figure 5.14: Left: Cross model with parameters fitted for 0.09% solution of CMC in water. Right: Laminar, steady calculation.

a 14m long pipe of with 105mm ID (compare Escudier et al. (2005)), whilst the other was a shorter section with a length equal to 4π diameters (compare Rudman et al. (2004)). In case of the former inlet/outlet boundary conditions were imposed. In case of the latter periodic boundary conditions were used.

In the vicinity of the wall a laminar sublayer will develop regardless of the constitutive law of the fluid. This stems from the fact that the inertial terms in the Navier-Stokes equation become negligible there. If we are to take full account of non-Newtonian rheology we have to solve the equation close to the wall up to the laminar sublayer.

The wall Reynolds number was known *a priori* and hence it was possible to specify the mesh size and refinement. The number of radial points varied from 64 to 128. All of the meshes were refined towards the wall with a growth ratio varying between 1.05 and 1.15. Since for experimental data the pressure gradient and therefore the wall shear-stress was known, it was possible to calculate wall viscosity and subsequently the wall coordinates. Wall coordinates allow us to establish the resolution required to capture the laminar sublayer.

In FLUENT we can choose between six k-ϵ low-Reynolds turbulence models. When a Lam–Bremohorst (LB) model is chosen a non-Newtonian turbulence modification appears in the Text User Interface. For the k-ω model, low-Reynolds number corrections can be also switched on.

Initially, the Lam–Bremhorst model with non-Newtonian modification was chosen. The fluid used for validation was a 0.09% aqueous solution of CMC from Escudier et al.

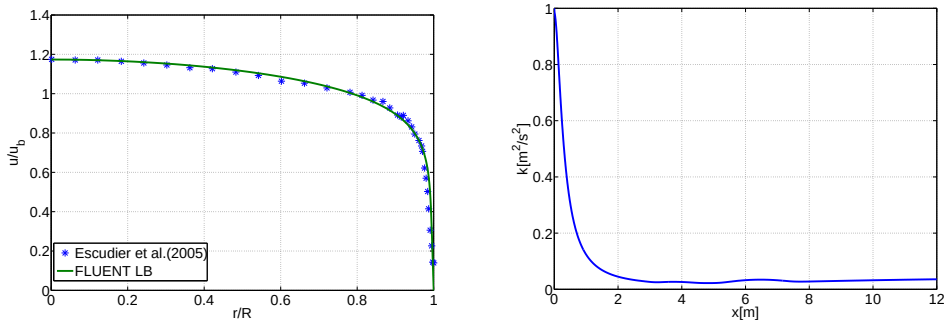

Figure 5.15: Left: Turbulent velocity profile in physical coordinates. Right: Turbulence intensity. The error of the turbulent intensity prediction was less than 5%.

(2005). This fluid was well described by the Cross model which is described in Section 4.2.2.

The results presented in Figure 5.15 show good agreement with the experimental data. The velocity profile in wall and physical coordinates as well as the ultimate estimate of the flow rate were within 5% of experimental data. Observe also that the specification of turbulent quantities did not much affect the flow field downstream. After two metres the turbulence intensity seems to stabilise around a value that is within 5% of the values reported in the experiment.

This positive agreement was also repeated for all of the shear-thinning fluids from Escudier et al. (2005). It is important to note that these fluids were well described by Carreau–Yasuda or Cross rheologies. These constitutive laws remove the singularity occurring in a classical power-law through limiting viscosities. The variation of viscosity occurs only close to the wall whilst in the rest of the pipe the low-shear limit is reached.

The simulation of a yield-stress fluid was more complicated due to the fact that the low-shear viscosities were not given in the Escudier experiment and therefore they became subject to arbitrary choice. Following Rudman and Blackburn (2006) the choice of cut-off parameters was such that the cut-off values were used only when the local strain rate was 10^4 times lower than the average. The straightforward application of the low Reynolds-number model on the full pipe mesh was completely unsuccessful. The turbulence intensity was vanishing downstream from the inlet and the resulting velocity profiles became laminar. The pressure drops were consequently underestimated. These

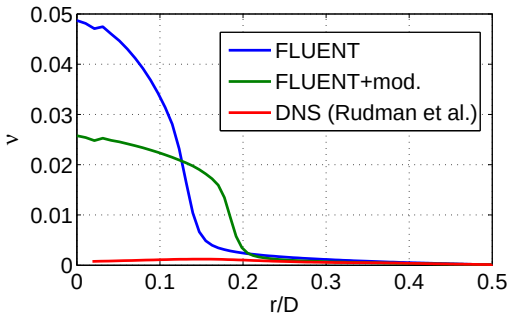

Figure 5.16: Viscosity profiles in FLUENT for Rudman et al. (2004) cases.

negative results gave rise to the theoretical studies presented at the beginning of this chapter.

5.4.1.1 Models with Turbulent Rate of Strain

We assume then that the rate of strain has the form:

$$\dot{\gamma} = \sqrt{2S_{ij}S_{ij} + \dot{\gamma}_t} \tag{5.62}$$

where the $\dot{\gamma}_t$ represents the effect of turbulence on the rate of strain. The form of this term is established based on dimensional analysis and the preceding considerations. Depending on the choice of the two-equation model, there are two pairs of quantities describing turbulence in the flow: k and ϵ or k and ω. Using these scales it it possible to construct a quantity with dimensions equal to the dimension of s_{ij}.

$$\gamma_t = f_\epsilon(k, \epsilon) = h_\epsilon\left(\mathrm{Re}_t\right) \frac{\epsilon^2}{k^2}, \tag{5.63}$$

$$\gamma_t = f_\omega(k, \omega) = h_\omega\left(\mathrm{Re}_t\right) \omega^2, \tag{5.64}$$

where an additional damping function was added. In the above expressions Re_t is the turbulent Reynolds number i.e. the Reynolds number based on turbulence quantities. This is to counteract the asymptotic behaviour of the wall of turbulence quantities. As outlined in Section 4.1.3 k tends to x_2^2 as we approach the wall whilst ϵ is of the order of 1. Therefore, if no damping is used than the above expressions will tend to infinity at the wall. This is why a damping function of the following form is used:

$$h_\epsilon\left(\mathrm{Re}_t\right) = h_\omega\left(\mathrm{Re}_t\right) = 1 - \exp\left(\mathrm{Re}_t\right). \tag{5.65}$$

The turbulence Reynolds number is expressed in the k-ϵ model for a power-law fluid as:

$$\mathrm{Re}_t = \frac{k^2}{\epsilon\nu}, \tag{5.66}$$

where the viscosity is taken from the previous iteration of the algorithm.
Simulations have been run for all available cases. Periodic boundary conditions have been adopted to simulate fully developed flow. When necessary a pressure drop has been calculated from the profile and given data. An initial guess was that of a Newtonian fluid with viscosity equal to the wall viscosity reported in corresponding publications. The results of these calculations are presented in Table 5.1. The simulations utilising DNS viscosity profiles show clearly the benefit of an accurate estimation of this quantity, both results were significantly improved with respect to the unmodified model. For the Pinho (2003) data most of the results were giving similar and accurate results and for the experimental Herschel–Bulkley data from Escudier et al. (2005) the results from the original model were much better. Two conclusions can be drawn from this result. Firstly, estimating the average velocity in the bulk of the fluid matters but only when the values of viscosity reach the low-shear cut-off and only if the cut-off value is comparable to the turbulent viscosity achieved at the centre. An accurate model of turbulent strain in the bulk of the fluid will not on its own improve the result. To suppose otherwise would be equivalent to believing that the viscous effects manifest themselves far from the boundary layer and although such a supposition would not be entirely unjustified for non-Newtonian fluids, the conclusion would further contradict the significance of convective terms that should dominate outside the boundary layer. A further investigation of viscosity profiles calculated from the proposed models shows that k-ω gave the closest approximation (see Figure 5.17). The viscosity profiles show good agreement with those obtained with DNS. These were the results for which the highest in pressure gradient prediction accuracy was obtained.

5.5 Concluding remarks

The analysis presented in this chapter establishes that the mean rate of strain can be as much as seven times higher than the mean velocity strain in some regions of the flow. For the instantaneous rate of strain this value can be even larger. Both, power-law and

Table 5.1: Flow-rate predictions showing improvements in accuracy for selected cases.

Source	Unmodified		Model	
	Predicted flow-rate [m/s]	Error	Predicted flow-rate [m/s]	Error
Pinho (2003)	3.16	0.06	3.18	0.06
	1.48	0.06	1.49	0.04
	1.3	0.03	1.31	0.02
Rudman et al. (2004)	0.7	0.3	0.88	0.12
	0.84	0.16	0.97	0.02
Escudier et al. (2005)	2.18	0.07	2.39	0.17

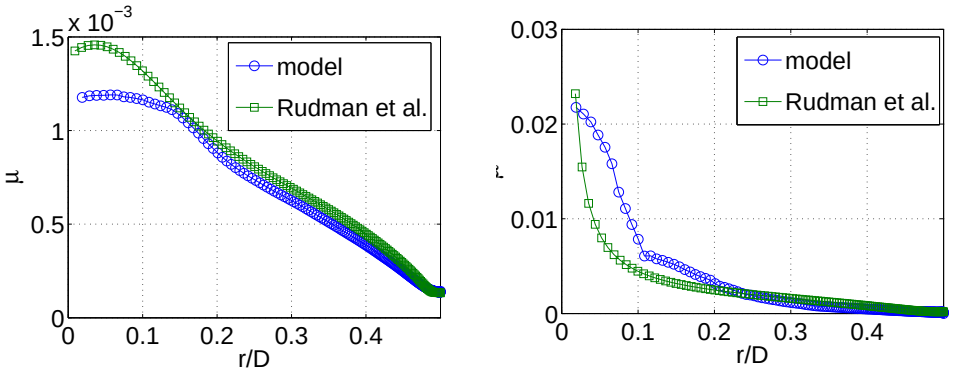

Figure 5.17: Viscosity profiles for $Re_W = 7000$ $\tau_Y = 0.24$ (left) $\tau_Y = 0.85$ (right). The viscosity of the flow is closely reproduced.

Herschel–Bulkley fluid exhibit this different, but in case of the latter the difference is more vital as it controls the yielded and unyielded regions that can appear throughout cross-section.

The investigations of the probabilistic information of the rate of strain conclude that the log-normality cannot be regarded as an accurate description. For the fluctuating rate of strain, however, there seems to be a fairly good match in some regions and this effect appears in both: power-law and Herschel–Bukley fluids. This finding is potentially useful for developing an effective molecular viscosity model.

The applicability of these findings in CFD calculations depends on the regularisation of the constitutive law. If the regularisation limits the maximum value of viscosity to be an order of magnitude smaller than the effective eddy viscosity than the proposed corrections will not take place. Otherwise, for the cases were regularisation does not play a leading role, this study shows that the predictions can be improved by as much as 18%.

Chapter 6

Modelling stratified flow

Stratified flow is one of the most common patterns in multiphase flows. The pattern forms when gravity dominates and leads to segregation. This occurs, when one fluid has a much larger density than the other.

Initial research in this area was focused on empirical correlations that allow the prediction of bulk quantities such as gas hold-up or pressure drops in long pipelines with or without inclination. This chapter surveys some of these correlations, concluding that none of them is universal, which shows that there is still some unknown dependency that affects the models.

This chapter also presents derivations of two velocity profiles. Similarly, to single phase flow, the laminar profile can be derived analytically without any additional closures. The interfacial shear-stress appears as an integration constant and it can be expressed in terms of known parameters. The resulting relationship between mass-flow-rate and pressure is not given explicitly. The turbulent profile has been proposed by Biberg (2007) and here even the interfacial-shear stress is not given explicitly. The mass-flow-rate to pressure relation can be extracted after solving the model equations in terms of the liquid height and shear-stress ratios.

With the correlations and analytical velocity profiles we can study the accuracy of CFD results. We employ the periodic boundary conditions described earlier and compare the results with unsteady simulations. It is argued that CFD-turbulence models are inadequate if they do not contain models of interfacial turbulence. DNS data supply additional evidence that the phase coupling, as well as turbulent effects, have a major

impact on bulk quantities and are required for scientific understanding and robust engineering predictions.

6.1 Empirical pressure drop correlations

The empirical correlations surveyed here were developed to solve a common engineering problem: estimate the gas phase volumetric fraction and the pressure drop in the pipe, if the superficial velocities of gas and liquid phases are known. The superficial velocity of phase P is the volumetric flow rate of phase P divided by cross-sectional area i.e.

$$U_{\mathrm{sP}} = \frac{1}{|A|} \int_A \alpha_P \mathbf{U} \cdot \, \mathrm{d}\mathbf{S}, \tag{6.1}$$

where α_P is the phase fraction and A is the cross-sectional area. This quantity takes into account the phase distribution and therefore it does not reflect the actual average velocity with which the phase is moving. The superficial velocity of phase P is the average velocity as if P were the only phase present in the cross-section. Superficial velocity can be directly computed from mass flow rate, which is often known *a priori*. The actual average velocity of the phase can be calculated only if the phase distribution is known. Then it can be calculated as the velocity averaged over a cross-sectional phase fraction.
Two situations are surveyed here:

1. Co-current, stratified flow: gas/Newtonian liquid.
2. Co-current, Stratified flow: gas/non-Newtonian liquid.

6.1.1 Stratified gas/Newtonian liquid

The first attempts to understand and predict friction factors in two-phase flows were undertaken by Lockhart and Martinelli (1949) and Martinelli and Nelson (1949). Both approaches begin with a friction factor correlation and assume that that the pressure drops computed from the parameters of both phases are equal.

$$\frac{dp}{dx} = \frac{2\rho f_P U_P^2}{\mu_P} \tag{6.2}$$

where P denotes the phase. The second assumption is the steady state for phase fraction: the flow under consideration comprises two co-current streams and the volume

fraction remains constant throughout the pipe. The relaxation of the second assumption was addressed by Martinelli and Nelson (1949). By defining hydraulic diameters as d_G and d_L certain area ratios were defined:

$$\kappa_P = \frac{4A_P}{\pi d_P^2} \tag{6.3}$$

where $A_P = \alpha_P A$. To predict friction factors the empirical formulae were utilised

$$f_P = C_P \left(Re_P\right)^{-m_P} \tag{6.4}$$

The parameter m_P adopts a value 1/4 or 1 if the phase P is respectively in the turbulent or laminar regime. The pressure is non-dimensionalised with the pressure drop that would occur if only one phase was transported through a pipe.

$$\phi_P^2 = \frac{\left(\frac{dp}{dx}\right)_{TP}}{\left(\frac{dp}{dx}\right)_P} \tag{6.5}$$

Simple algebraic transformations lead to

$$\alpha_G = 1 - \kappa_L^{(3-m_L)/(m_L-5)} \phi_L^{4/(m_L-5)} = \kappa_G^{(3-m_G)/(m_G-5)} \phi_G^{4/(m_G-5)} \tag{6.6}$$

which can be solved giving the pressure drops results. Usually for the sake of data presentation a Martinelli parameter is introduced.

$$X^2 = \frac{\phi_g^2}{\phi_l^2} = \frac{\left(\frac{dp}{dx}\right)_g}{\left(\frac{dp}{dx}\right)_l} \tag{6.7}$$

Comparison with experiments shows that the derived equations overestimate the real value of pressure drops. This over-prediction is due to the assumption of constant wall shear stress which is definitely an overly pessimistic approximation. Normally the phases will interact with each other and the stress on the smooth interface will be lower than the wall stress thus leading to friction reduction. Conversely a rough interface will lead to increased friction.

A modification worth mentioning taking the above issues into account is the one performed by Chisholm (1967), who applied some geometrical considerations to evaluate the effective wall shear stress. For a stratified flow he obtained:

$$\alpha_L^{1-0.5m_L} \left(\frac{A}{A - A_L}\right)^{1-0.5m_G} = \frac{X^2}{Z} \frac{(d_G')^{0.5(1+m_G)}}{(d_L')^{0.5(1+m_L)}} \tag{6.8}$$

$$\phi_L^2 = \frac{1}{d_G'} \left(1 + \frac{A_G}{A_L}\right)^{1-m_L} \left(\frac{A_G}{A_L Z^2} + 1\right) \tag{6.9}$$

where $d_P^{'}$ are phase hydraulic diameters non-dimensionalised with the hydraulic radius of a single phase flow and Z is another non-dimensional quantity defined by:

$$Z = \left(\frac{1 + \tau^{'} A_G / A_L}{1 - \tau^{'}} \right) \tag{6.10}$$

where $\tau^{'}$ is a non-dimensional stress.
Comparisons with more recent procedures presented by Brennen (2005) reveals that the above approaches can provide a robust engineering approximation.

6.1.1.1 Taitel and Dukler

The approach proposed by Taitel and Dukler (1976) begins with assuming stratified flow in a pipeline and then writing the momentum balance equations for both phases:

$$-A_l \frac{\mathrm{d}p}{\mathrm{d}x} - S_l \tau_{wl} + \tau_i S_i = 0 \tag{6.11}$$

$$-A_g \frac{\mathrm{d}p}{\mathrm{d}x} - S_g \tau_{wg} - \tau_i S_i = 0, \tag{6.12}$$

where A_P is the phase cross-sectional area, S_P is the phase wetted perimeter, S_i is the interface cross-sectional length, τ_{wP} is the wall shear-stress and τ_i is the shear-stress at the interface.
Now assuming that the pressure drop is constant and the same for both phases this can be simplified to one equation.

$$\tau_{wg} \frac{S_g}{A_g} - \tau_{wl} \frac{S_l}{A_l} + \tau_i S_i \left(\frac{1}{A_L} + \frac{1}{A_G} \right) = 0 \tag{6.13}$$

Subsequently friction factors are used to estimate wall shear stresses. Eventaully an implict procedure is developed that chooses the gas phase fraction so as to minimise the residuum of Equation (6.13).
Further details of the derivation and the MATLAB scripts developed to calculate the gas phase fraction and corresponding pressure drop can be found in Appendix B.

6.1.2 Stratified gas/non-Newtonian liquid

There is extensive literature on two-phase, non-Newtonian fluid friction factors. This interest can be explained by the fact that non-Newtonian fluids are typically fluids of high viscosities and their transport can pose serious engineering difficulties. Moreover,

certain mixtures of phases can exhibit non-Newtonian properties of their bulk quantitites e.g. bulk viscosity of slurries has yield stress and power-law behaviour. Treating one of the phases as non-Newtonian in stratified flow, allows us to study flows that can comprise more than two phases.
It is not entirely true that only high viscosity fluids can have non-Newtonian properties. Even water has its own non-trivial rheology which Newtonian behaviour merely approximates. However, in a highly viscous fluids these changes are easier to observe and are more significant from an engineering design standpoint.

6.1.2.1 Heywood

The analysis of non-Newtonian liquid–gas flows in horizontal pipes has been first conducted by Heywood and Charles (1979) as an extension of Newtonian liquid–gas case. The analysis was limited and did not encompass liquid turbulent flow. The liquid assumed to behave as in an open channel and gas as in a closed duct giving well-defined concepts of hydraulic diameters and friction factors.
The algebra eventually leads to:

$$\phi_L^2 = \frac{\hat{u}_L^n}{\hat{D}^{1+n}}, \tag{6.14}$$

where $\hat{D}$ is the hydraulic diameter non-dimensionalised with respect to pipe diameter and $\hat{u}$ is a velocity non-dimensionalised by a single phase liquid velocity under the same condition.
One of the main advantages of the formula shown is that it predicts drag reduction due to decreased wetted perimeter which is not the case with Martinelli correlations. Validation of the results was performed by comparison with computational results.

6.1.3 Farrooqi and Richardson

Farooqi and Richardson (1982) considered three-phase gas/liquid flows where, the liquid was additionally a mixture of a Newtonian and non-Newtonian fluid. The Lockhart–Martinelli predictions were, as usual, overestimating the results but were still within +/- 30%.
Their studies included the drag reduction phenomenon in shear thinning suspensions which has been reported to occur when air was injected into a laminar flow of liquid

suspension. The maximum drag reduction has been correlated with a ratio of the apparent viscosity to the apparent viscosity at $\mathrm{Re_{MR}} = 2000$. An empirical correlation of this maximum drag reduction has been obtained and is the following

$$\min \phi_L^2 = \begin{cases} \lambda^{0.205} & \text{if } 0.6 < \lambda < 1 \\ 1 - 0.0315\lambda & \text{if } 0.35 < \lambda < 0.6 \\ 1.9\lambda & \text{if } 0.05 < \lambda < 0.35 \end{cases}, \tag{6.15}$$

where $\lambda = (u_1/u_{tr})^{1-n}$ which according to power-law model is the same as mentioned above viscosity ratio.

The accuracy of the Heywood and Charles (1979) prediction has been also validated for power-law indices in the interval from 0.14 to 0.326 but inaccurate for greater n where it was over-predicting the actual values.

6.1.4 Dziubinski

Dziubinski (1995) attempted to develop a general correlation for intermittent two-phase flows in a pipe where one phase had non-Newtonian properties. His analysis was based on a loss coefficient which is of the form:

$$\Lambda = \frac{\tau_w \rho D^2}{\mu^2} = \frac{\tau_w}{\rho \overline{u_1}^2} \mathrm{Re}^2 = \frac{f}{8} \mathrm{Re}^2, \tag{6.16}$$

for Newtonian fluids and:

$$\Lambda = K(\frac{4n}{3n+1}) \mathrm{Re}_{\mathrm{MR}}^2, \tag{6.17}$$

for non-Newtonian fluids. By performing analogous steps as in the Newtonian case and by substituting friction factor correlations for laminar (Equation (4.78)) and turbulent flow:

$$f = 0.3164 \mathrm{Re}_{\mathrm{MR}}^{-1/4}, \tag{6.18}$$

Dziubinski reports the resulting formulae for loss coefficient which have a form:

$$\Lambda = 8\alpha_L C_L \mathrm{Re_{TP}} \quad \text{(laminar)} \tag{6.19}$$

$$C_L = \frac{1 + 1.036\ 10^{-4} \mathrm{Re}_{\mathrm{TP}}^{1.235}}{1 + 1.036\ 10^{-4} \mathrm{Re}_L^{1.235}} \tag{6.20}$$

$$\Lambda = 0.0131\alpha_L \left(\frac{3n+1}{4n}\right)^{-5} \exp 1.745 \frac{3n+1}{4n} - 0.634\alpha_L \mathrm{Re}_{\mathrm{TP}}^{7/4} \quad \text{(turbulent)} \tag{6.21}$$

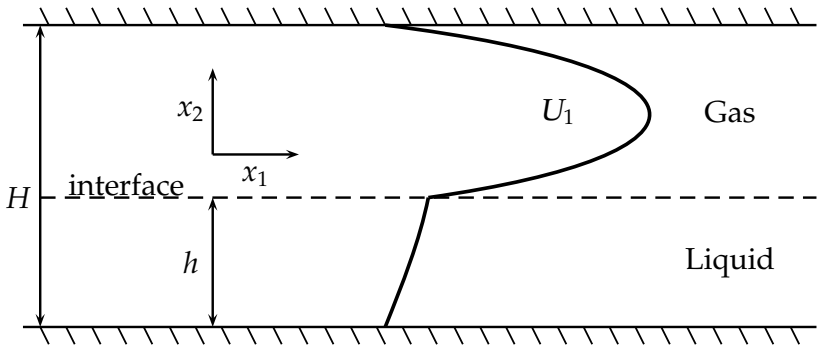

Figure 6.1: Sketch of the physical problem.

agree quite well with extensive experimental data giving an error of $+/-15\%$ and $+/-30\%$

Xu, Wu, Shi, Lao and Li (2007) extended the analysis of Heywood and Charles (1979) to inclined pipes. Two flow patterns were considered: stratified flow, which is more common in downward inclined pipe and slug flow which appears more often in upward sloped pipes. In the first case liquid, due to its high viscosity has been assumed to be laminar while in the second case both possibilities were considered. The analysis begins with a force balance equation accounting for buoyancy effects and interfacial stresses. Typical correlations relating Reynolds number and friction factors were substituted into the equations. Formulae for pressure drops for stratified and slug flow in inclined pipes were obtained. Comparison with experimental data has shown that proposed equations deviated 20% and 30% in case of stratified and slug flow respectively.

6.2 Analytical velocity profiles

In this section we present the derivations of velocity profiles for channel flow. These profiles are further considered in the solution of the pressure drop and holdup predictions.

It is often assumed that the origin of the coordinate system is at the interface. In some cases it can significantly simplify the analysis.

6.2.1 Laminar profiles

Laminar profiles have been derived by Bird et al. (1960), Biberg and Halvorsen (2000) and Sim (2006). Bird et al. derives the profiles for rectangular channel flow but under the assumption that the liquid pool height is known. This eliminates one of the unknowns. Subsequently they obtain explicit expressions for the physical velocities of both phases. Biberg and Halvorsen focuses on pipeline flow. Sim derives the profiles for channel flow with stationary and oscillating walls. However, he deals with the inverse problem i.e. he assumes the pressure drop and the liquid height to be known and obtains the formulas for average velocities which are than compared with results from numerical simulations.

In this section we deal with channel flow and we assume that only phase mass fluxes or superficial velocities are given. The problem under consideration is depicted in Figure 6.1. It involves two incompressible, Newtonian fluids, further denoted as g and l, flowing between two flat plates set H apart. At a distance h from the lower plate there is a phase interface over which fluid density and viscosity change but with velocity and shear-stresses assumed to be continuous. Gravity acts in $-x_2$ direction. The problem is essentially two-dimensional.

We adopt the assumption that the flow is fully developed which means that the velocity and the phase fraction profiles do not change with the axial coordinate x. Material properties of both phases are assumed to be constant. The equations of motion for case simplify to:

$$\frac{\partial p}{\partial x} = \frac{\partial}{\partial y}\left(\mu \frac{\partial U}{\partial y}\right) \tag{6.22}$$

$$\frac{\partial p}{\partial y} = \rho g. \tag{6.23}$$

The assumption of fully developed flow also means that the RHS of Equation (6.22) and RHS of Equation (6.23) depend only on the coordinate y. Integrating the latter between 0 and y gives:

$$p(x, y) = \rho g y + p(x, 0), \tag{6.24}$$

which leads to a conclusion that $\frac{\partial p}{\partial x}$ is a function of x only. Since the LHS of Equation (6.22) is a function of x and the RHS is a function of y, we conclude that both

sides of this equation must be constant. Therefore, the streamwise pressure gradient does not change with the axial coordinate:

$$\frac{\partial p}{\partial x} = \text{const.} \tag{6.25}$$

To solve this equation with respect to the pressure gradient and interface height h we assume that the velocity profiles are continuous over the interface:

$$\lim_{y \to h^+} U(y) = \lim_{y \to h^-} U(y) = u_i \tag{6.26}$$

and that viscosity can be expressed as

$$\mu = \begin{cases} \mu_g & y > h \\ \mu_l & y < h \end{cases} . \tag{6.27}$$

Solving this with the assumption that the interface is at level h and that the velocity profile is continuous gives a concatenation of two "mirror" Couette flows:

$$U = \begin{cases} \frac{\partial p}{\partial x} \frac{1}{2\mu_g} \left(y^2 - (H+h)y + Hh \right) + \frac{u_i}{H-h}(H-y) & y > h \\ \frac{\partial p}{\partial x} \frac{1}{2\mu_l} \left(y^2 - hy \right) + \frac{y}{h} u_i & y < h \end{cases} , \tag{6.28}$$

where u_i is the velocity at the interface. We further assume that the stress at the interface is also continuous so that we can put an equality between the left and right side limits:

$$\lim_{y \to h^+} \tau = \lim_{y \to h^-} \tau \tag{6.29}$$

and therefore

$$\lim_{y \to h^+} \mu_g \frac{\partial U}{\partial y} = \lim_{y \to h^-} \mu_l \frac{\partial U}{\partial y}, \tag{6.30}$$

which after substituting Equation (6.28) gives the interface velocity in terms of height and pressure gradient:

$$u_i = -\frac{\partial p}{\partial x} \frac{H}{2\mu_l} \frac{1}{\frac{1}{h} + \frac{\mu_g}{\mu_l} \frac{1}{H-h}} = -\frac{\partial p}{\partial x} \frac{H}{2} \frac{h(H-h)}{\mu_g h + \mu_l (H-h)} \tag{6.31}$$

We have now expressed the velocity profile in terms of pressure gradient and height. These are the unknowns which can be calculated only if additional conditions are imposed on the system. One way is to specify phase mass fluxes:

$$\frac{1}{H} \int_h^H U(y) \, \mathrm{d}y = U_{\mathrm{sg}} \qquad\qquad \frac{1}{H} \int_0^h U(y) \, \mathrm{d}y = U_{\mathrm{sl}}. \tag{6.32}$$

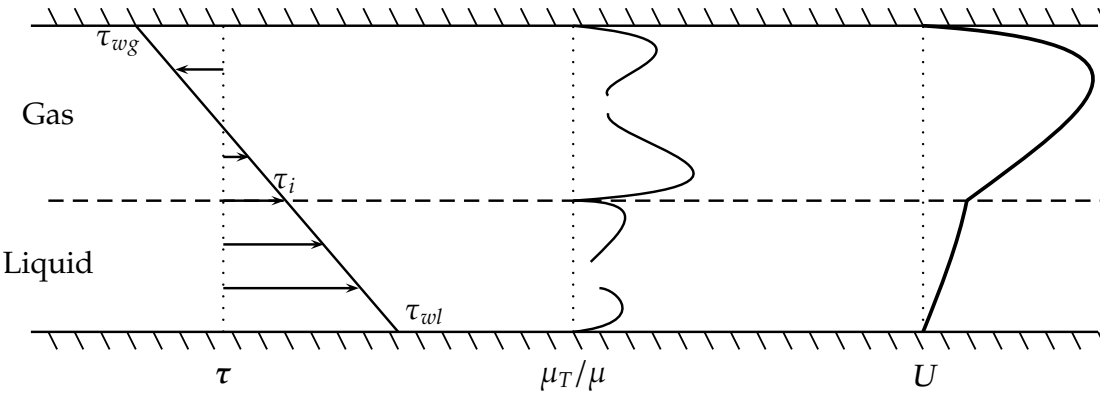

Figure 6.2: Turbulent profiles in steady state fully developed channel flow: shear stress (left), eddy viscosity (centre), mean velocity (right).

Substituting the velocity profile and subsequent integration gives a system of two non-linear equations

$$\begin{cases} \left(\frac{\partial p}{\partial x}\frac{1}{2\mu_g}\left(y^3/3-(H+h)y^2/2+Hhy\right)+\frac{u_i}{H-h}(Hy-y^2/2)\right)\Big|_h^H = U_{\text{sg}} \\ \frac{\partial p}{\partial x}\frac{1}{2\mu_l}\left(-1/6h^3\right)+\frac{h}{2}u_i = U_{\text{sl}} \end{cases}, \tag{6.33}$$

where the first equation has only been written symbolically for the sake of brevity. This system of equations can be ultimately solved numerically. The roots of these rational expressions will give $\frac{\partial p}{\partial x}$ and h, satisfying the constraints in Equation (6.32).
To solve this problem numerically a set of MATLAB scripts were written. The script use Newton's method for finding roots of a differentiable function and are further described in Appendix B.

6.2.2 Turbulent profiles

To investigate turbulent flow profiles we adopt the averaged Navier–Stokes equations. The derivation begins with a decomposition of instantaneous velocities into their mean and fluctuating components and applying the averaging operation to the system of equations. This leads to equations for mean velocity profiles containing the Reynolds stress term which has to be expressed in terms of known parameters. It is now convenient to assume that the origin of the coordinate system is at the interface.

Integration of Equation (6.22) will give a linear profile of shear-stress.

$$\tau_{xy} = \frac{\partial p}{\partial x} y + \tau_i. \tag{6.34}$$

This is depicted on Figure 6.2. Let h_P denotes the position of the wall wetted by phases P. Then we can express the wall shear stress by:

$$\tau_{wP} = \frac{\partial p}{\partial x} h_P + \tau_i. \tag{6.35}$$

Combining the two above expressions gives:

$$\tau_{xy} = \tau_i - (\tau_{wP} - \tau_i)\frac{y}{h_P}. \tag{6.36}$$

The shear stress can now be expressed as a sum of Reynolds stress and the stress coming from molecular viscosity:

$$\tau_{xy} = \mu \frac{\partial U}{\partial y} - \overline{\rho u v}. \tag{6.37}$$

The Reynolds stress terms is expressed by:

$$-\overline{\rho u v} = \mu_t \frac{\partial U}{\partial y}. \tag{6.38}$$

Biberg (2007) proposes an algebraic model of turbulence that reproduces log-layers at both wall regions. Both phases in the flow are analysed separetely and the the coupling between phases is ensured through continuity conditions at the interface and specification of turbulence levels. We will now focus on the model applicable within one phase and because of this the indices denoting the phase are temporarily dropped. The non-dimensional profile is expressed using two new parameters.

$$R = \frac{\tau_i}{\tau_w} \qquad\qquad Y = \frac{y}{h}. \tag{6.39}$$

Additionally, there is a parameter measuring the level of turbulence at the interface. For know we define the parameter as the rescaled interfacial eddy viscosity from Biberg (2011)

$$K = \frac{\mu_t\big|_{Y=0}}{\rho \kappa h u_i^*}, \tag{6.40}$$

where κ is the von Karman constant. Eddy viscosity at the interface, and therefore K, is not known *a priori*. Therefore, the closure of K is the key element of the model and will be discussed separately.

First let us consider the mixing length model. Prandtl originally expressed the eddy viscosity in the following way:

$$\mu_t = \rho l v_t, \tag{6.41}$$

where l is the mixing length and v_t, considering the momentum transfer between flow strata (see Schlichting (1955)), is further approximated by:

$$v_t = l\frac{\partial U}{\partial y}. \tag{6.42}$$

Substituting back into Equation (6.38) and then back into equation Equation (6.37) and then neglecting the viscous term we arrive at:

$$v_t = \sqrt{\frac{\tau_{xy}}{\rho}} \tag{6.43}$$

From this point onwards the derivation assumes that the profile at the wall follows the logarithmic distribution with respect to wall proximity:

$$U = \frac{u^*}{\kappa}\ln\left(1 - Y\right) + C_1, \tag{6.44}$$

where $u^* = \sqrt{\frac{\tau_w}{\rho}}$ and the constant C_1 is:

$$C_1 = \operatorname{sgn}\left(\tau_w\right)\frac{u^*}{\kappa}\left(\ln\left(\frac{u^* h}{\nu}\right) + \kappa B\right). \tag{6.45}$$

If we substitute Equation (6.44) into Equation (6.41) and use the auxillary expression in Equation (6.43) we arrive with

$$l = \kappa h(1 - Y)\sqrt{\left|\frac{\tau_{xy}}{\tau_w}\right|} \tag{6.46}$$

as Y approaches the wall. The conclusion from above derivation is that the mixing length must be of the form in Equation (6.46) in the vinicity of the wall to reproduce a logarithmic velocity profile. Using this intuition from mixing length theory the algebraic model of viscosity is decomposed in the following way:

$$l = \mathcal{L}\mathcal{F}, \tag{6.47}$$

where $\mathcal{L}$ is the turbulent length scale and $\mathcal{F}$ represents the effect of non-constant shear stress. The postulate on $\mathcal{F}$ is the following:

$$\lim_{Y\to 1}\mathcal{F}\left(Y\right) = \sqrt{\left|\frac{\tau_{xy}}{\tau_w}\right|}, \qquad \lim_{Y\to 0}\mathcal{F}\left(Y\right) = \sqrt{\left|\frac{\tau_{xy}}{\tau_i}\right|}. \tag{6.48}$$

Note that for $Y = 0$ or $Y = 1$, $\mathcal{F}(Y) = 1$.
According to Equation (6.46) $\lim_{Y\to 1} \mathcal{L}(Y) = \kappa h(1 - Y)$. This enforces the following set of conditions:

$$\mathcal{L}(1) = 0 \qquad\qquad \frac{\partial \mathcal{L}}{\partial Y}(1) = -\kappa h \tag{6.49}$$

On the side of the interface $\mathcal{L}$ must be related to the interfacial turbulence level K. The interface turbulence length scale l_i is obtained from K after rescaling by channel height which is the only dimensional quantity containing unit length scale.

$$l_i = \kappa h K \tag{6.50}$$

The condition $\lim_{Y\to 0} \mathcal{L}(Y) = l_i$ is now imposed. In terms of non-dimensional parameters this is expressed by:

$$\mathcal{L}(0) = \frac{\mu\big|_{Y=0}}{\rho v_t} = \kappa h K. \tag{6.51}$$

The second order polynomial which satisfies the required condition has the following form:

$$\mathcal{L} = \kappa h (1 - Y)(Y + K(1 - Y)). \tag{6.52}$$

The remaining terms in Equation (6.41) and approximation proposed Equation (6.47) can be treated together as one function:

$$\mathcal{U} = \mathcal{F} v_t \tag{6.53}$$

and interpolated using the third order rational polynomial:

$$\mathcal{U} = \frac{b_1 + b_2 Y + b_3 Y^2 + b_4 Y^3}{1 + b_5 Y + b_6 Y^2}. \tag{6.54}$$

The conditions for $\mathcal{U}$ are derived from Equation (6.48)

$$\mathcal{U}(Y \to 1) = \frac{1}{u^*}\frac{|\tau_{xy}|}{\rho}, \qquad\qquad \mathcal{U}(Y \to 1) = \frac{1}{u_i^*}\frac{|\tau_{xy}|}{\rho}, \tag{6.55}$$

where $u_i^* = \sqrt{\frac{|\tau_i|}{\rho}}$ is the interface friction velocity. Using the defined non-dimensional parameters and expressions for shear-stress we obtain

$$\tau_{xy} = \operatorname{sgn}(\tau_w)\, \rho u^{*2} (R(1 - Y) - Y), \tag{6.56}$$

Now substituting back to Equation (6.55) and taking first and second order derivatives it is possible to obtain six conditions.

$$\mathcal{U}\big|_{Y=1} = u^* \qquad \mathcal{U}_{,Y}\big|_{Y=1} = u^*(1+R) \qquad \mathcal{U}_{,YY}\big|_{Y=1} = 0 \tag{6.57}$$

$$\mathcal{U}\big|_{Y=0} = u^* \qquad \mathcal{U}_{,Y}\big|_{Y=0} = -u^*(1+1/R) \qquad \mathcal{U}_{,YY}\big|_{Y=0} = 0 \tag{6.58}$$

Solving for the polynomial constants gives:

$$\mathcal{U} = \frac{u^*\left(Y^3 + |R|^{5/2}\,(1-Y)^3\right)}{R^2(1-Y)^2 + R\,(1-Y)\,Y + Y^2}. \tag{6.59}$$

Combining all the interpolated expressions, the final form of the Biberg (2007) algebraic turbulence model is given by:

$$\frac{\mu_t}{\rho h u^*} = \frac{\kappa\,(1-Y)\,(Y + K\,(1-Y))\left(Y^3 + |R|^{5/2}\,(1-Y)^3\right)}{R^2\,(1-Y)^2 + R\,(1-Y)\,Y + Y^2} \tag{6.60}$$

With this algebraic viscosity model it is possible to obtain the velocity distribution by integrating Equation (6.38)

$$U = \int \frac{\tau_{xy}}{\mu_t}\,\mathrm{d}y \tag{6.61}$$

Using partial fractions the final velocity profile is given by

$$U = \mathrm{sgn}(\tau_w)\frac{u^*}{\kappa}\Delta + C \tag{6.62}$$

where

$$\begin{aligned}\Delta = {} & \ln(1-Y) + \frac{\left(K^3+R^3\right)\ln\left(Y + K\,(1-Y)\right)}{|R|^{5/2} - K^3} \\ & + \frac{(R+\sqrt{|R|}\,\sqrt[3]{|R|}\ln(Y + |R|^{5/6}(1-Y))}{3\left(K - |R|^{5/6}\right)} \\ & - \frac{(R+\sqrt{|R|})(K+2|R|^{5/6})\,\sqrt[3]{|R|}\ln\left(Y^2 - (1-Y)\left(Y - (1-Y)\,|R|^{5/6}\right)|R|^{5/6}\right)}{6\left(K^2 + |R|^{5/6}K + |R|^{5/3}\right)} \\ & + \frac{K\left(R+\sqrt{|R|}\right)\sqrt[3]{|R}}{\sqrt{3}\left(K^2 + |R|^{5/6}K + |R|^{5/3}\right)}\arctan\left(\frac{2\,(Y-1)\,|R|^{5/3} + (2Y-1)\,|R|^{5/6} + 2Y}{\sqrt{3}|R|^{5/6}}\right)\end{aligned} \tag{6.63}$$

where C is a function of the Reynolds number and can be given explicitly by recalling that at the wall the profile should reproduce Equation (6.44):

$$\lim_{Y\to 1} U = \frac{u^*}{\kappa}\ln\left(1-Y\right) + C_1. \tag{6.64}$$

Therefore the constant C is expressed by:

$$C = C_1 + \frac{u^*}{\kappa}\Psi(R, K) \tag{6.65}$$

where

$$\Psi = -\frac{K\left(R + \sqrt{|R|}\right)}{\sqrt{3}\left(K^2 + |R|^{5/6}K + |R|^{5/3}\right)}\tan^{-1}\left(\frac{1 + \frac{2}{|R|^{5/6}}}{\sqrt{3}}\right) \tag{6.66}$$

Using these profiles the expression for average velocity can be derived. This can be tied back to the original problem of predicting pressure drop and phase fraction, given superficial velocities. Unfortunately the expression for interface friction will not be given explicitly and has to be obtained numerically. An algorithm using a double bracketing root search algorithm is proposed in Biberg (2007). Biberg gives an algorithm for pipelines, but for the purpose of this thesis a channel version has been written.

The additional advantage with respect to the correlations given in the previous section is the ability to investigate the details of the flow i.e. velocity and viscosity profile. This can be used as a tool for the validation of CFD codes (this is pursued in the next section).

The above derivation introduces two unknown quantities: the non-dimensional turbulence levels at the interface K_g and K_l. Similarly to the laminar case, turbulent viscosity is not necessarily continuous over the interface. There is common agreement that the gas phase perceives the liquid phase as a moving wall. The eddies in the gas phase will usually have insufficient energy to significantly deform the liquid. On the liquid side, the interface fluctuations are inhibited by the stabilising presence of gravity (see Hunt (1984)).

Eventually two types of interfaces are distinguished: smooth and wavy interfaces. This classification mirrors closely the distinction between smooth and rough wall surfaces. Smooth interfaces are considered when the there is no deformation or the deformations are small in comparison with pipeline diameter. Wavy interfaces allow larger interface oscillations but the waves must be beyond the point of breaking. The effect of the perturbed interface is manifested by an increased roughness parameter in the flow model.

Smooth interface closures are given by:

$$K_g = \frac{8\nu_g}{|U_g - U_l|h_g}, \qquad K_l = 1. \tag{6.67}$$

The wavy interface closures are:

$$K_g = 0.065\frac{\rho_g(U_g - U_l)^2}{(\rho_l - \rho_g)\, g h_g}, \qquad K_l = 10\sqrt{\frac{\rho_g}{\rho_l}}\left|\frac{U_g - U_l}{U_l}\right|. \tag{6.68}$$

The constants in these expressions have been adjusted to fit the experimental data of Espedal (1998).

6.3 Comparison against CFD

Validation of the method proposed in the previous chapter has been conducted. Recall, that the problem specifies mass fluxes or superficial velocities as the only input to the calculation. Therefore, the height and actual velocities for the respective phases are unknown *a priori*. To facilitate comparisons the Reynolds number employed is based on superficial velocity.

$$\mathrm{Re}_G = \frac{U_{\mathrm{sg}} H}{\nu_G} \qquad \mathrm{Re}_L = \frac{U_{\mathrm{sl}} H}{\nu_L} \tag{6.69}$$

Two approaches have been compared: steady state calculations performed in OpenFOAM and unsteady calculations run in FLUENT. The OpenFOAM model uses the periodic boundary conditions described in the previous chapter whilst the FLUENT model uses a full length channel 50 inlet diameters in length with split velocity inlet and pressure outlet boundary conditions. The channel inlet was split using User Defined Functions and constant velocities, reflecting the specified superficial velocity have been imposed. In some cases the split has been moved down (towards the liquid side), to decrease the initial change in liquid height. Because OpenFOAM is a three dimensional finite volume code and the problem addressed here is two-dimensional, a periodic patch is applied on the faces with a normal aligned with the third dimension.

Because FLUENT performs a full channel simulation, the computational times are not comparable. Unsteady simulations are at a disadvantage as they need to solve the problem in spatial and temporal domains until the steady state is reached. They also require a finer mesh as they need to resolve the effect of the inlet and outlet boundary conditions which constrains the choice of time steps in explicit VOF, since large time steps in comparison with the width of spatial discretisation will results in a high Courant number and unstable behaviour. The comparison aims only at reproducing the fully developed flow conditions and comparing the profiles with analytical or experimental

results. In principle, it can be expected that FLUENT full simulation will reproduce the experimental data more faithfully since it resolves the inlet and outlet effects.

6.3.1 Laminar profiles

An implicit solution of equation Equation (6.33) was implemented in MATLAB in order to calculate the profiles in Equation (6.28) and obtain the characteristics of the flow for given superficial velocities. The code is documented and appended to this document. To demonstrate the effects of both Reynolds numbers on the flow profiles, three different liquid Reynolds number have been chosen and a range of gas Reynolds numbers have been examined. First, a purely analytical examination have been carried out to gauge the effects of Reynolds numbers on characteristics of the flow. The results are depicted in Figure 6.3. Subsequently four typical velocity profiles have been chosen to compare against CFD calculations. OpenFOAM calculations are compared against analytical solutions. The number of outer loop iterations in periodic boundaries has been set to 3×10^3. PISO algorithm was used to account for pressure velocity coupling and no solution of momentum equation has been performed (no predictor step). Convergence in the inner loops for the solution of the pressure equation was set to 10^{-10} residual tolerance. PCG method was used to solve the pressure equation and Diagonal Incomplete Cholesky was used as the preconditioner. The cell count in the transverse direction was set initially to 20 and then was increased up to 60. On the last increase the difference in estimated pressure gradients was less than 5% of the actual value and therefore further refinement has been abandoned.

Discrepancy between pressure the calculated and analytical pressure gradient was less than 5% and the profiles remain in close correspondence. The profiles were normalised with physical gas velocity so that the area under the gas profile is one. This allows to compare shapes rather than particular values. The number of outer iterations before reaching convergence was an average less than 2×10^3 whilst the number of iterations was on average 2.33.

From the solution of Equation (6.33) an asymptote at $\mathrm{Re}_G = 0$ is clearly visible. As anticipated an increase in liquid Reynolds number is much more pronounced than the increase in gas Reynolds number. Two profiles after rescaling with gas velocities are actually identical.

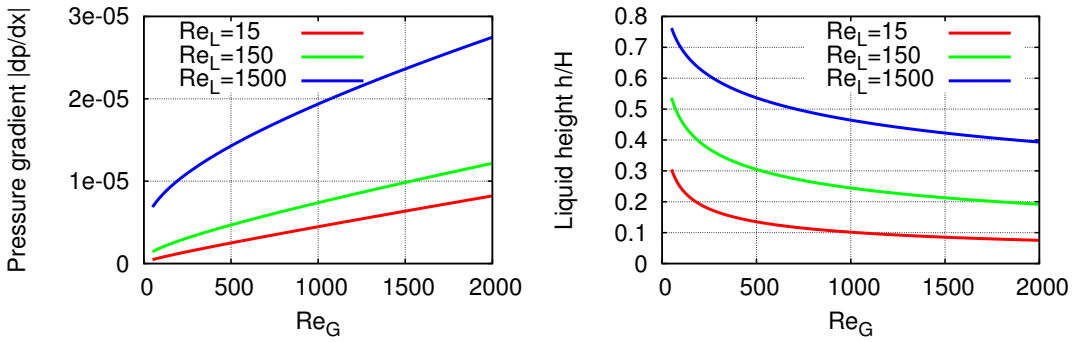

Figure 6.3: The behaviour of liquid height and pressure gradient with respect to Reynolds number in laminar flow.

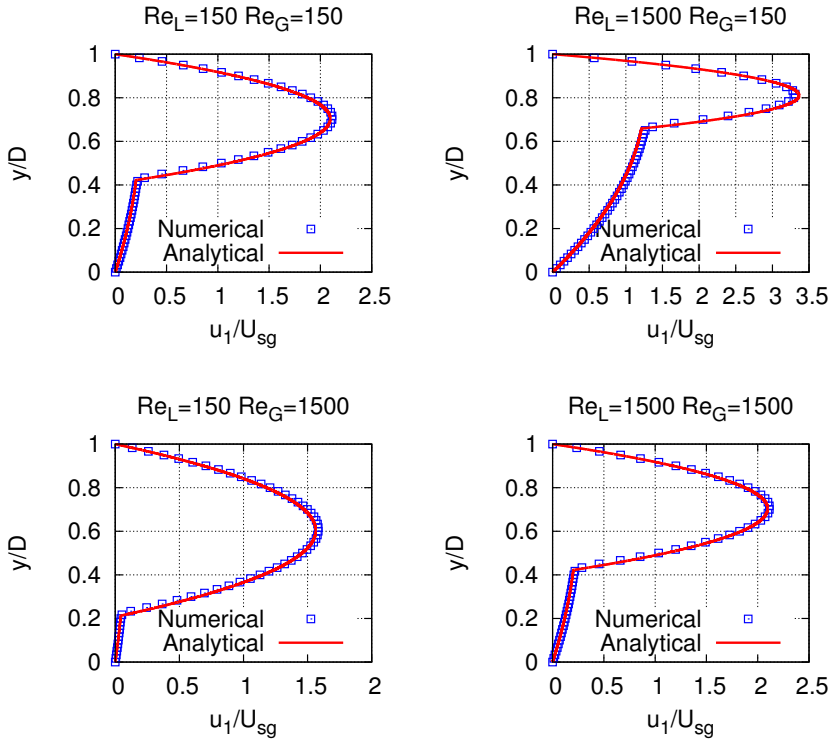

Figure 6.4: Typical velocity profiles obtained with OpenFOAM: Profiles on the left have $\mathrm{Re}_G = 150$ on the right $\mathrm{Re}_G = 1500$. Profiles at the top have $\mathrm{Re}_L = 150$ and at the bottom: $\mathrm{Re}_L = 1500$.

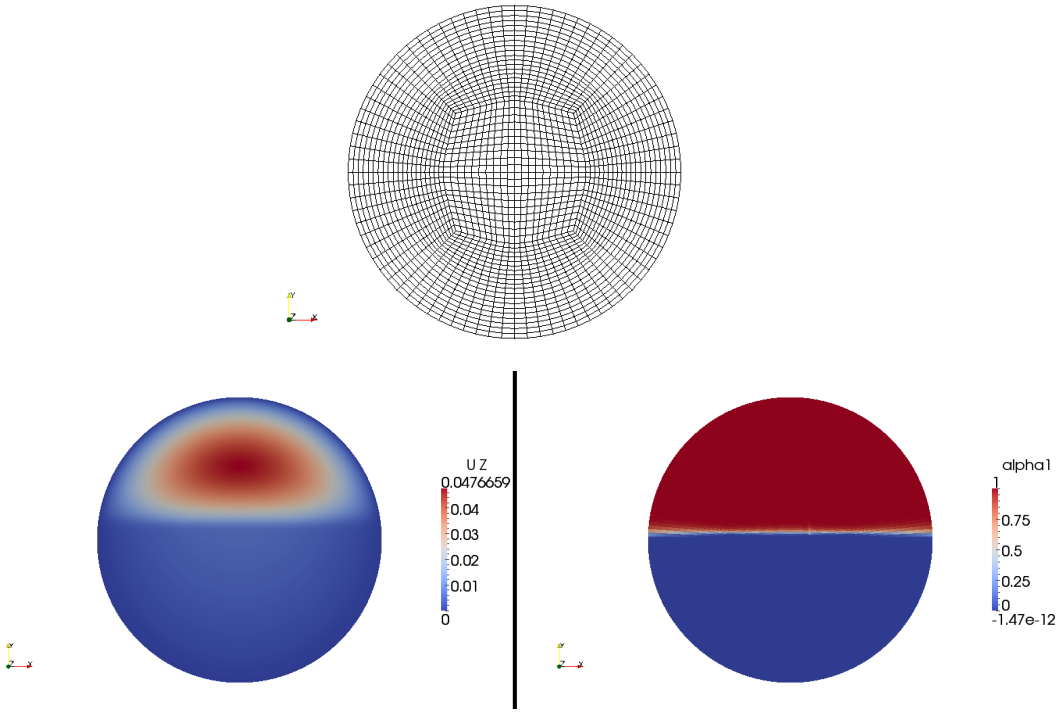

Figure 6.5: Top: the grid employed, Bottom: The normal velocity distribution and the phase fraction distribution.

The results obtained for the 3D model of a pipeline are shown in Figure 6.5. A script was first developed in order to create meshes for the 3D problem. Note that in Figure 6.5 the grid is divided into three regions in the cross-section: the central quadrilateral and an outer and inner circles. The script allows the specification all the dimensions of the problem i.e. the diameter, the length of the section, the concaveness of the middle section and the ratio of each cross-sectional section diameter to the diameter of the whole pipe.

The results in Figure 6.5 are the results of for the laminar model with $\mathrm{Re}_L = 1500$ and $\mathrm{Re}_G = 600$. Other Reynolds number were covered as well and it was discovered that the method correctly conserves the specified mass fluxes. The method creates a "smeared" interface at the place where the interface connects with the wall. This may be caused by the cells being rotated in such a way the surface normals are no longer aligned with the direction of the consecutive corrections.

Both, the Superbee scheme and the artificial flux method (described in Section 3.1.1)

were used. The differences between these approaches was small in comparison with the cell size.

To obtain these results, the surface tension term in Equation (3.6) had to be suppressed. The inclusion of this term renders the method unstable. The reason for this unstable behaviour have not been investigated since the study was focusing on turbulent flow where the surface tension is expected to play a very minor role. The validation of the method for 3D cases would require further investigations.

6.3.2 Turbulent profile

The RANS equations as described in Section 3.1.3 are adopted as a model of turbulent. Therefore, only the mean velocity field is calculated. The influence of fluctuating components is modelled through Reynolds stresses that are closed by the Boussinesq hypothesis and eddy viscosity is expressed by k and ω for which additional transport equations are solved. For the results presented in this section a two-equation k-ω model was used with various turbulence interface corrections. At the end of this section results from the MATLAB code implementing the Biberg model are also presented.

Discretsation and the linear solvers are the same as in laminar cases. Additional transport equations are solved with Preconditioned Biconjugate Gradient with Incomplete LU decomposition. Mesh refinement was performed until the resulting pressure gradient difference was lower than 5%.

Results using a standard RANS turbulence model are shown in Figure 6.7. All of these models consistently predict the pressure gradient to be higher than experiment e.g. FLUENT calculations for $\mathrm{Re}_G = 1.32 \times 10^4$ and $\mathrm{Re}_L = 8.04 \times 10^4$ were giving an average pressure gradient in the fully developed region of 741 Pa, whereas the experimental value for this point was 285 Pa.

This effect is caused by an overly dissipative solution. The effective viscosity calculated in these cases exhibits a maximum around the interface which results from the large velocity gradient in the k-equation production term. Two-equation models are known to produce artificially high effective viscosity in regions of large normal strain (see Pope (2000)). This is shown in Figure 6.6. Qualitative and quantitatively similar results were obtained with OpenFOAM which leads to a conclusion that the problem is related to the model that is being used.

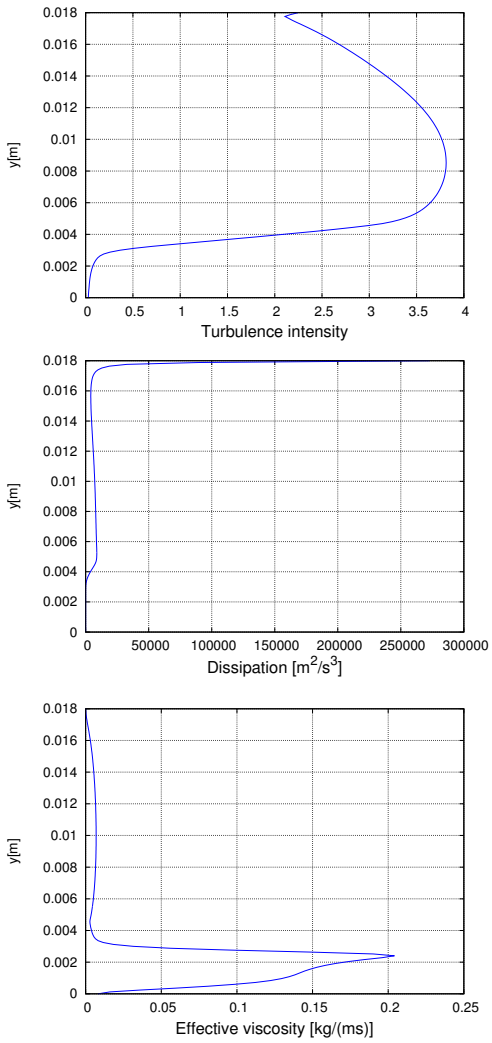

Figure 6.6: FLUENT results for turbulent quantities from top to bottom: turbulence intensity, turbulence dissipation and effective viscosity.

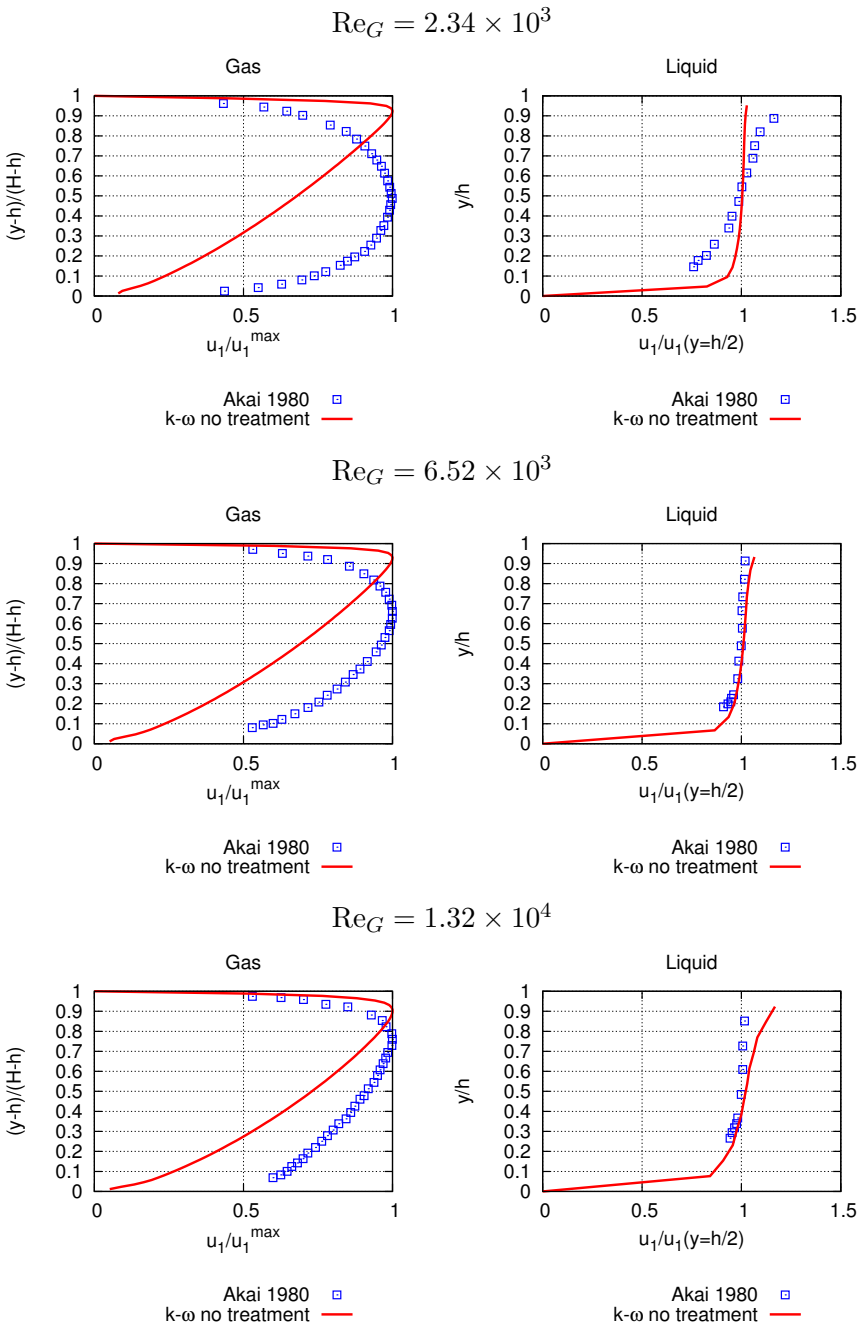

Figure 6.7: Standard turbulence models against Akai et al. (1981). Velocity profiles on the gas (left) and liquid (right) sides. Top: $\mathrm{Re}_G = 2.34 \times 10^3$ Centre: $\mathrm{Re}_G = 6.52 \times 10^3$, Bottom: $\mathrm{Re}_G = 1.32 \times 10^4$.

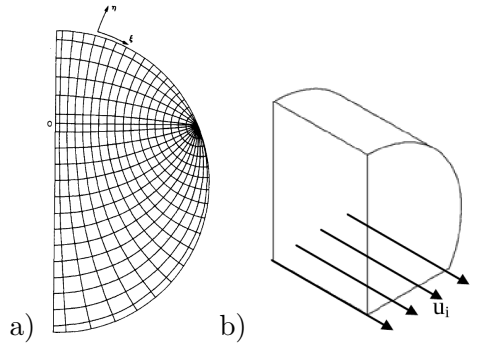

Figure 6.8: a) Curvilinear mesh (Issa (1988)) b) Single phase with moving wall (Holmås and Biberg (2007)).

Various interface treatments are employed to attenuate this artificial dissipation of RANS models. To date, there has been no effort to derive RANS models specifically for VOF multiphase model. Instead, single phase models have been used with various *ad-hoc* corrections.

Akai et al. (1981) use one of the low-Re k-ϵ models. The authors are using a finite difference method where the coordinate system is so defined as to have one direction normal to the interface and with the origin at the interface. This provides a clear distinction between liquid and gas phases and allows them to specify boundary conditions for k and ϵ, where empirical correlations obtained from Akai et al. (1980) are used. It also limits the solution to steady steady flows with flat interfaces in channels. The liquid pool height is obtained via scaling of coordinates.

Issa (1988) uses low and high Re k-ϵ models. The liquid pool height is obtained by fitting a special curvilinear mesh that fills the circular cross-section and has one chord denoting the interface position (see Figure 6.8). Therefore only flat interfaces can be obtained and only steady solutions can be considered. Subsequently, Issa imposes mass fluxes and chooses the position of the chord as to minimise the residuals in mass flux constraints.

In the VOF framework Egorov (2004) (ANSYS CFX) and Ghorai and Nigam (2006) (FLUENT) both use high Reynolds number models to simulate long channels. It is reported that the standard models in these commercial packages fail to predict the experimental data correctly. Then, Ghorai and Nigam modified the profiles around the interface by imposing log-layers. This is only of limited applicability as a logarithmic

profile does not necessarily emerge at the interface (see Biberg (2007)). Holmås and Biberg (2007) use the k-ω model. Only the gas phase is simulated - the liquid is modelled as a moving wall. Egorov includes an additional dissipation term in the equation for specific dissipation ω:

$$\frac{\partial \rho\omega}{\partial t} + \nabla \cdot \mathbf{U}\rho\omega = \rho C_{1\omega} \frac{\omega}{k} \overline{u_i u_j} \frac{\partial U_i}{\partial x_j} - \rho C_{2\omega}\omega^2 + \frac{\partial}{\partial x_j}\left[(\mu + \sigma\mu_T)\frac{\partial \omega}{\partial x_j}\right] + \underbrace{\rho \frac{|\nabla\alpha|}{\max|\nabla\alpha|} C_{2\omega}\omega_i^2}_{\text{interface treatment}} \tag{6.70}$$

where ω_i has a form of the wall value for ω if viscous sublayer is resolved, that is:

$$\omega_i = B\frac{\mu_P}{\rho_P C_{2\omega}(\Delta n)^2}. \tag{6.71}$$

In this formula ρ_P and μ_P are the density and viscosity respectively of a given phase, Δn is width of the cell and B is an adjustable constant. The main difficulty with this approach lies with the adjustable constant. Egorov argues that it is mesh dependent but there can also exist an additional parametric dependency related to the specific problem. Figure 6.9 shows only the pressure gradient predictions for Bruno (1988) air/water cases. The same meshes are employed, but two different liquid Reynolds numbers and a range of gas Reynolds number are investigated. Two different values of B are required in order to obtain the estimates for pressure gradients that are close to experimental values. This suggests that the slip velocity might be a relevant parameter in the scaling of B. When the choice of B is lower than the optimal value for a given set of experiments, then we clearly see a diverging behaviour as the slip velocity increases. Physically, B might be tied to interface "roughness". It increases the specific dissipation at the interface.

Additional difficulty in estimating ω_i is the width of the cell Δn. In general, with an unstructured mesh and with an arbitrary interface shape this may pose a significant difficulty. In this study, advantage was taken of the fact that the flows are stratified, with the normal to the interface parallel to the gravity direction. Moreover, a structured rectangular shape grid is employed and therefore the spatial dimensions of each cell can be calculated by iterating over all faces and taking a projection of the difference of cell and surface centroids onto a unit vector of a specific axis.

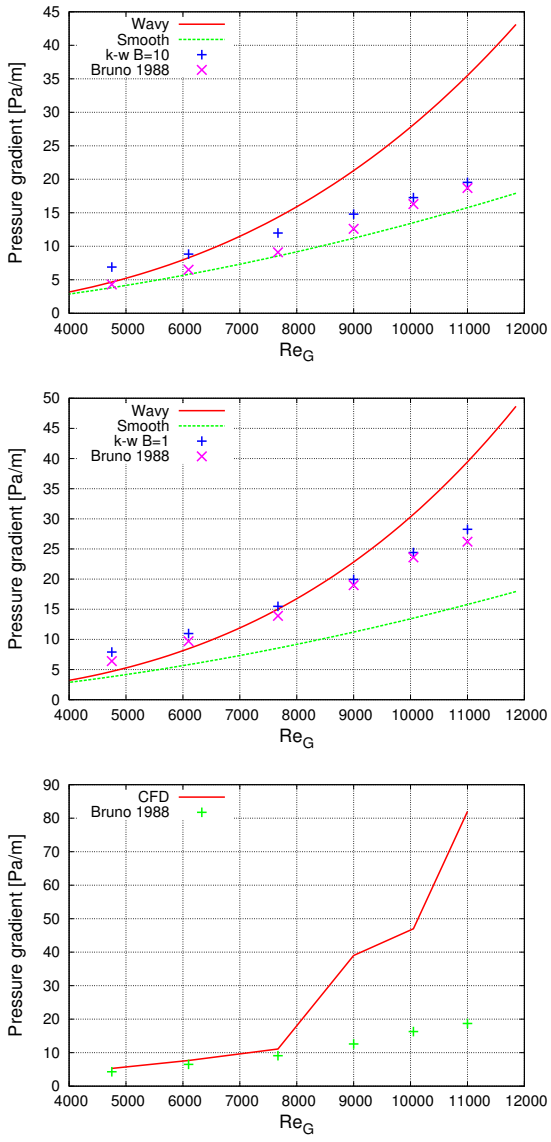

Figure 6.9: Egorov (2004) type correction: pressure gradient predictions. Smooth and wavy lines are plotted according to Biberg (2007) model. Top: $\mathrm{Re}_L = 255$ Centre $\mathrm{Re}_L = 745$, Bottom: $\mathrm{Re}_L = 255$ but with constant $B = 1$.

In their LES work Lakehal and Liovic (2011); Liovic and Lakehal (2007) develop a special treatment that dampens the sub grid scale effective eddy viscosity. Two algorithms are developed that calculate the distance to the interface and the interface shear velocity. With these two quantities an interface distance in shear-based units y^+_{int} can be obtained. Subsequently a van Driest type formula is used with different coefficients for the polynomial in the exponent. For the gas side the damping is given by:

$$f(y^+_{\text{int}}) = 1 - \exp\left(a_{1G}y^+_{\text{int}} + a_{2G}(y^+_{\text{int}})^2 + a_{3G}(y^+_{\text{int}})^3\right), \tag{6.72}$$

whereas on the liquid side:

$$f(y^+_{\text{int}}) = 1 - \exp\left(a_{1L}y^+_{\text{int}} + a_{2G}(y^+_{\text{int}})^2\right), \tag{6.73}$$

where a_{iP} are coefficients obtained from previous DNS studies (see the survey of recent DNS in Section 6.5).

Finally, Lo and Tomasello (2010), working with RANS equations of the k–ω model, review various approaches, including constant multiplicative damping of the effective viscosity at the interface:

$$\mu_T^{'} = \begin{cases} C^{'}\mu_T & 0 < \alpha < 1 \\ \mu_T & \text{otherwise} \end{cases} \tag{6.74}$$

where $C^{'}$ is a constant and α is VOF indicator function.

Lo and Tomasello (2010) propose another correction which again requires the calculation of interface distance. The distance to the interface is estimated based on the scaling laws of specific dissipation ω. It has been pointed out by Masson and Gleize (2004) that according to asymptotic analysis the following scaling is approximately correct for log-layers and the viscous sublayer:

$$\frac{1}{\omega}\frac{\partial\omega}{\partial y} \sim \frac{1}{y}. \tag{6.75}$$

and therefore a reciprocate of the function

$$F_{\text{int}}(\omega) = N\frac{1}{\omega}\frac{\partial\omega}{\partial y} \tag{6.76}$$

is proportional to the interface distance. N is an adjustable parameter. Using this additional information that we obtain from solving turbulence transport equations it is possible to define y^+_{int} as

$$y^+_{\text{int}} = \frac{\rho_P u_\tau}{F_{\text{int}}(\omega)\mu_P}. \tag{6.77}$$

Source	Mechanism	Coefficients
Egorov (2004)	Equations (6.70) and (6.71)	$B = 2500$ (depends on slip velocity)
Lo and Tomasello (2010)	Equation (6.74)	$C^{'} = 0.01$
Lo and Tomasello (2010)	Equation (6.78)	$C^{'} = 0.1$, $A_{+} = 2500$, $A_{+} = y^{+}_{\text{lim}} = 500$
Lakehal and Liovic (2011)	Equation (6.72), Equation (6.73)	$a_{1G} = -0.00013$, $a_{2G} = -0.00036$, $a_{3G} = -1.08 \times 10^{-5}$, $a_{1L} = -0.0014$, $a_{2L} = -0.00064$

Table 6.1: VOF turbulence interface damping mechanisms.

Moreover, this modification also allows switching between low and high Reynolds number formulations making the k-ω model insensitive to wall refinement. This approach has some drawbacks and its further developed in Masson and Gleize (2004). For our purposes it is also important to note that Lo and Tomasello (2010) conclude with simple van Driest damping in the vicinity of the interface:

$$\mu_T^{'} = \begin{cases} C^{'}\left(1 - \exp\left(\frac{y^{+}_{\text{int}}}{A^{+}}\right)\right) & y^{+}_{\text{int}} < y^{+}_{\text{lim}} \\ \mu_T & \text{otherwise} \end{cases} \tag{6.78}$$

where coefficients $C^{'}$, y^{+}_{lim} and A^{+} are adjusted to fit the experimental data.
Interface treatments used in concatenation with VOF boundaries are summarised in Table 6.1. Constant coefficients that have been reported in the original papers are also shown there.
Another treatment that is proposed in the current study combines the approach of Egorov with automatic switching between low and high Reynolds number approaches proposed by Menter (1994) for k-ω model. The aim was to remove the sensitivity to near wall refinement that appeared in RANS turbulence models. The motivation to use this method in this study is to remove mesh-dependant constants in Egorov model. Menter uses a composite value of ω expressed in the following form:

$$\omega_w = \sqrt{\omega^2_{\text{Lam}} + \omega^2_{\text{Log}}} \tag{6.79}$$

where ω_w is the value at the wall, ω^2_{Lam} ω^2_{Log} are the values coming from an analytical approximation of the logarithmic and the laminar sublayer in turbulent boundary layer of the k-ω model:

$$\omega_{\text{Lam}} = \frac{6\nu_w}{C_\mu \Delta y^2}, \qquad \omega_{\text{Log}} = \frac{\sqrt{k}}{\sqrt[4]{C_\mu}\kappa \Delta y}, \tag{6.80}$$

where Δy is the distance from the wall.
In the laminar expression for turbulence we identify Equation (6.71) from Egorov model. So eventually the model for the interface:

$$\omega_i = \hat{B}\sqrt{\hat{\omega}^2_{\text{Lam}} + \hat{\omega}^2_{\text{Log}}} \tag{6.81}$$

where

$$\hat{\omega}_{\text{Lam}} = \frac{6\nu_w}{C_{2\omega}(\Delta n)^2}, \qquad \hat{\omega}_{\text{Log}} = \frac{\sqrt{k}}{\sqrt[4]{C_{2\omega}}\kappa \Delta n}, \tag{6.82}$$

and the parameteric dependency was retained due to unsatisfactory results of initial attempts.
The results are shown in Figure 6.10, they were obtained with the value of $\hat{B} = 100$ which in a much stronger damping of turbulence than in the case of Bruno (1988) cases. This might be caused by the higher density ratio as in Akai et al. (1981) cases we are dealing with mercury as opposed to water. The choice of the value was preceded b the fine tunning process and within 20% variation of the mesh size the predictions were consistent. Care must be taken in chooshing the mesh size since the limitations are imposed not only by interface modelling but also by the wall function modelling.
Last but not least, the Biberg model is employed. The prediction of pressure gradient and liquid height is shown on Figure 6.11 where pressure gradient prediction of a CFD turbulence model is also depicted. Moreover, velocity profiles are plotted in Figure 6.12. Only the wavy cases have been examined. The coefficients in Equation (6.68) is changed to 0.013 (original value×1.5), to better reflect the data at large pressure gradients.

6.4 Non-Newtonian fluid and two-phase flow

The periodic boundary conditions together with the k-ω turbulence model presented in the preceding section were used in order to analyse the velocity profile as a function of the power-law index in the constitutive law describing the viscosity of the liquid phase.

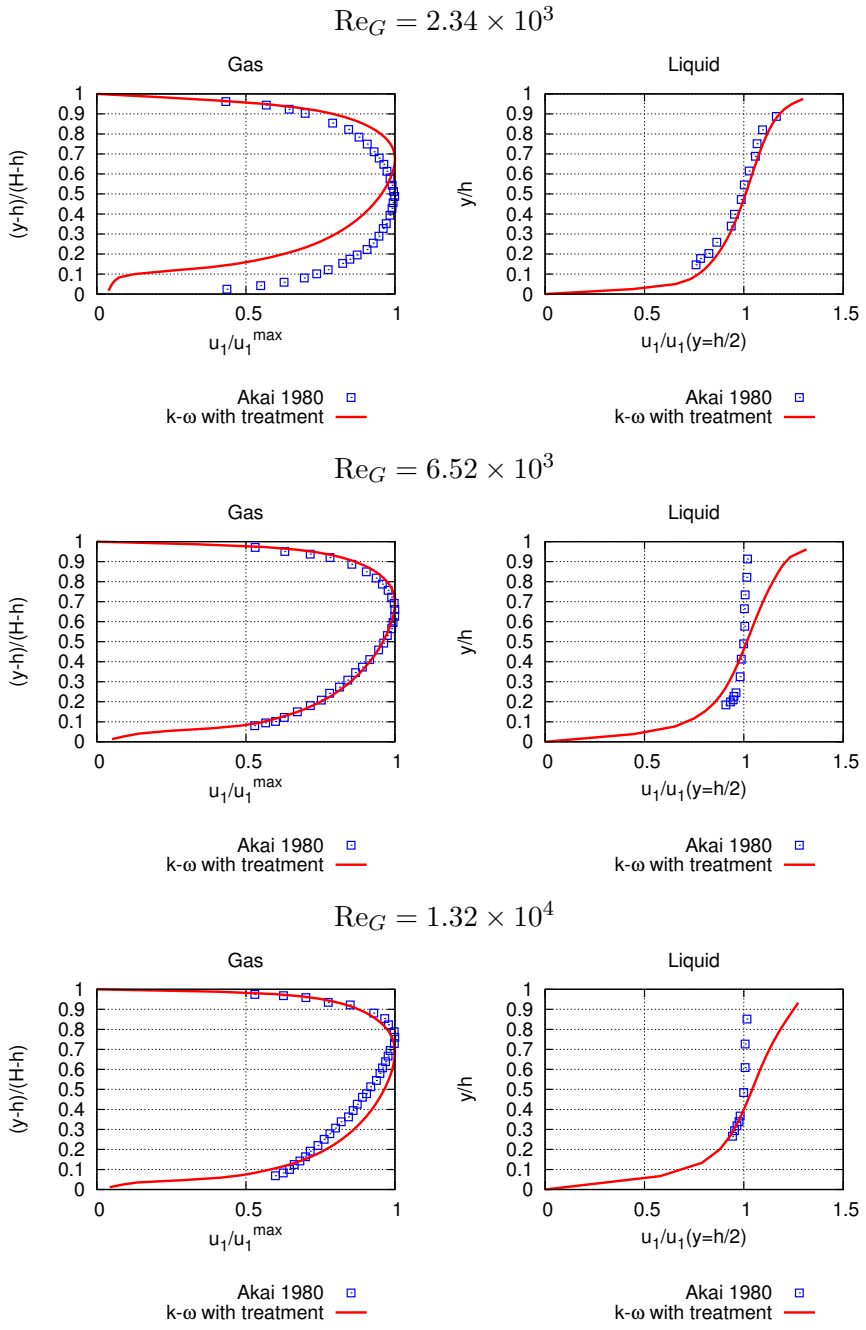

Figure 6.10: Modified turbulence models against Akai et al. (1981). Velocity profiles on the gas (left) and liquid (right) sides. Top: $\mathrm{Re}_G = 2.34 \times 10^3$ Centre: $\mathrm{Re}_G = 6.52 \times 10^3$, Bottom: $\mathrm{Re}_G = 1.32 \times 10^4$.

.

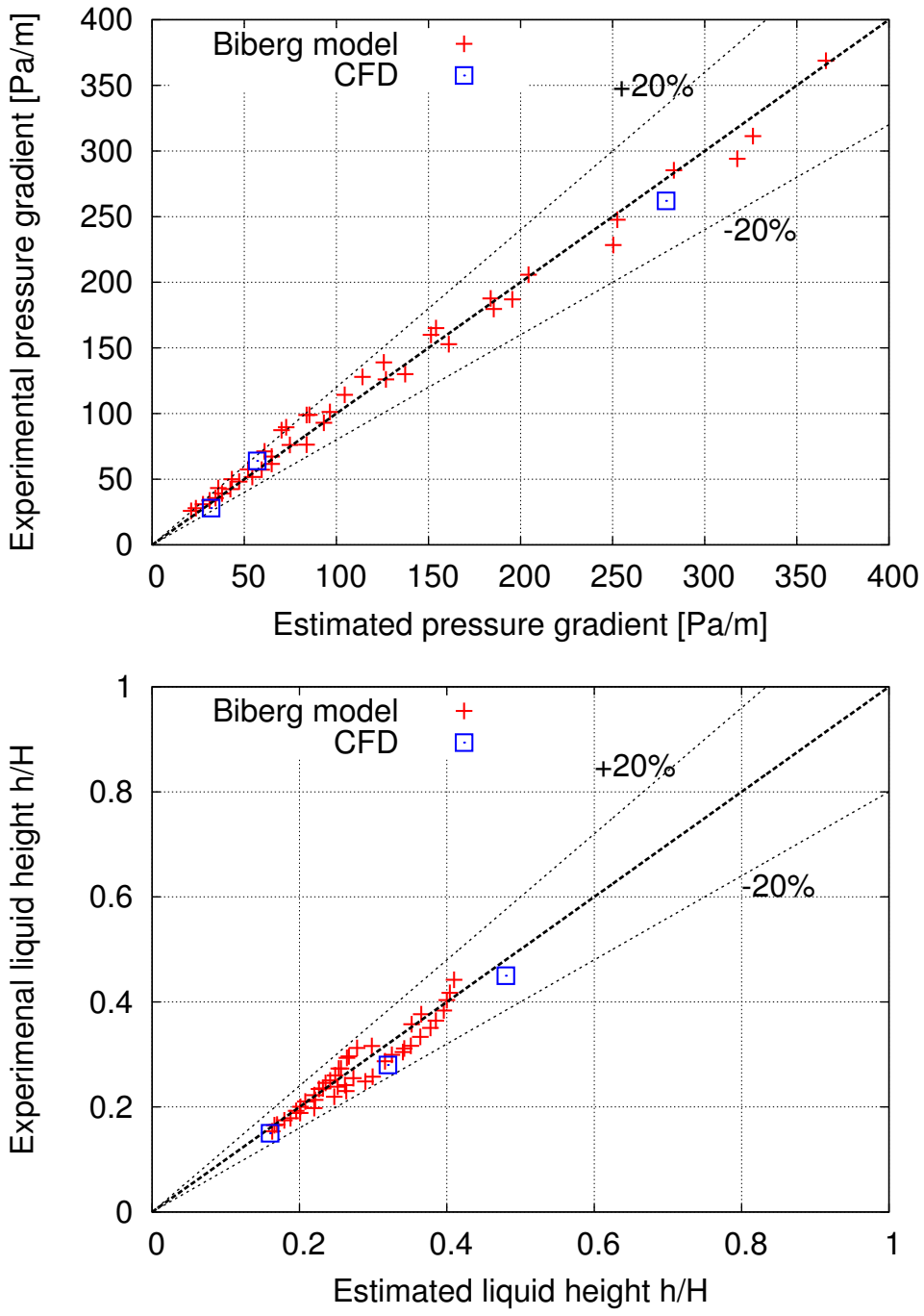

Figure 6.11: Estimated against experimental pressure gradients and liquid height.

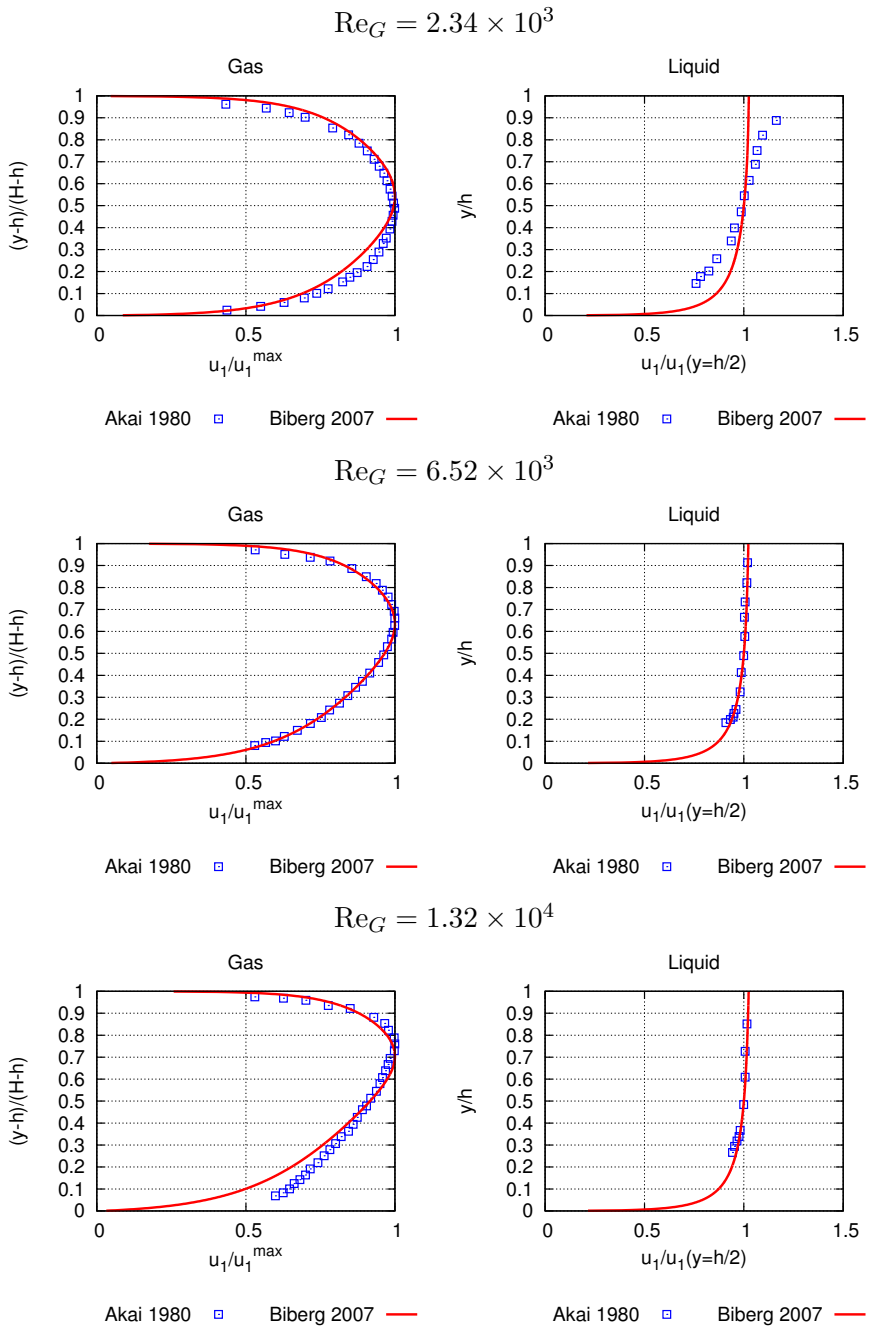

Figure 6.12: Biberg model against Akai et al. (1981). Velocity profiles on the gas (left) and liquid (right) sides. Top: $\mathrm{Re}_G = 2.34 \times 10^3$ Centre: $\mathrm{Re}_G = 6.52 \times 10^3$, Bottom: $\mathrm{Re}_G = 1.32 \times 10^4$.

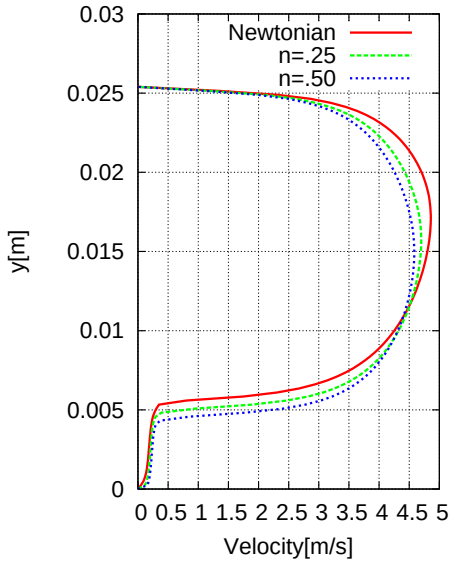

Figure 6.13: The influence of non-Newtonian property on the velocity profile of the two-phase flow.

The cases developed on Bruno (1988) were used as a base Newtonian fluid, since for these cases it was possible to obtain a good approximation of pressure gradients. For the non-Newtonian behaviour the Cross-model, described in Chapter 4, was used in order to avoid problems with zero-shear singularity.

A typical change of the velocity profile is shown in Figure 6.13. Despite the effective viscosity being dominated by the eddy viscosity (derived Boussinesq hypothesis) the change is clearly visible. Liquid laminar viscosity at the interface decreases with decreasing n and the profile on the gas side becomes less skewed. Additionally, it should be noted that with the increase of the power-law index the phase fraction of the gas phase increased. Since the Lockhart–Martinelli parameter is positive for these flows the correlations, developed through analysis and experimental investigations by Xu et al. (2007), confirm this prediction.

6.5 Recent DNS and LES results

The numerical investigation of interface flows can be divided into simulations with shear-free surfaces (free surface) and with sheared surfaces. The literature from the

last two decades exhibits a steady progress in the numerical investigations of these flows.

Lam and Banerjee (1992) apply no-slip and free-slip boundary conditions in their DNS. They observed that the nature of the boundary was less significant compared with the magnitude of shear applied on the boundary. Despite the fact that vortex structures behave differently at each boundary i.e. vortices can attach to a free-slip boundary, but they cannot attach to a no-slip boundary, turbulent streaks appear on both sides and their characteristics are related to $\tilde{S} = S|\overline{u_1 u_3}\,|/\epsilon$. Lam and Banerjee conclude with a criterion for turbulent streak formation based on $\tilde{S}$.

Handler et al. (1993); Nagaosa (1999); Pan and Banerjee (1995); Shen et al. (1999); Tsai (1998) study free-surface flows numerically. These papers focus on coherent structures on the liquid side, just below the interface. Two types of characteristic structures that are identified to occur are splats/antisplats and swirls. Splats are structures deflected by the interface, whilst swirls are attached vortices with vorticity aligned with the normal to the interface. Various correlations between these events are examined. Most importantly, the contribution to Reynolds stress is assessed through quadrant analysis. It is found that swirls, if not disturbed by interface movement, are relatively long lived and can interact with each other. Additionally, Nagaosa and Handler (2003) studied heat flow at the phase boundary.

Subsequently, sheared interfaces between fluids of high density ratios have been studied by Lombardi et al. (1996). Continuity of velocity profiles and shear stresses was adopted as the interface boundary condition and free slip boundaries were imposed on the domain boundaries parallel to the interface. Periodic boundaries have been applied on other boundaries with the streamwise boundary having a specified pressure gradient. Both the statistical and instantaneous structure of turbulence are reported in their paper. The statistics of turbulence on the gas side, compared with wall bounded flow, are not altered significantly whereas on the liquid side the mean velocity profile normalised with interface friction velocity is markedly different from the Nikuradse log law. Also the turbulent energy budget is different: the production peak is increased and shifted towards the boundary. Turbulent diffusion has a completely different trend (with the peak value at the interface): the dissipation rates are higher. Reynolds stresses on the liquid side are non zero and show a positive trend as y^+ decreases.

Instantaneous coherent structures were studied as well. The objective was to evaluate the robustness of the Lam and Banerjee (1992) criterion and to establish whether turbulent events are correlated on both sides. It has been confirmed that at least 20% of events are correlated across the interface although this estimate might be overly pessimistic due to the strict spatial coherence criterion that was adopted. The coupling was dominated by gas ejection–liquid ejection type events, but also gas sweep–liquid ejection had a significant contribution. Coupled events comprised 60% of the Reynolds stress.

Gas turbulence over wavy walls and slightly deformable interfaces has been studied by De Angelis et al. (1997), Fulgosi et al. (2003) and Lin et al. (2008) . In the first paper two sine waves have been imposed using coordinate transformation, whilst in the remaining two an advection equation for liquid elevation has been solved for Froude and Weber numbers that secure a non-breaking interface. All these studies confirm that the structure of turbulence is altered in the near-interface region. Particularly in the case of a slightly deformable interface it has been observed that the turbulent as well as dissipation at the interface are dampened, although, unlike the wall boundary, turbulent kinetic energy has a non zero value at the interface. In the Reynolds stress budget it can be seen that the redistribution of energy is mostly affected. The mean velocity profile on the gas side differs from the flat interface case significantly. Similarly to the flat interface case Reynolds stresses on the liquid side increase towards the interface.

Finally, breaking waves are studied with LES approach by Lakehal and Liovic (2011). The authors use VOF method to track the interface. Subgrid scale turbulence is modelled with Smagorinsky model and a van Driest type damping of eddy viscosity at the interface is used. To this end an algorithm for interface distance reconstruction and calculation of shear velocity is also employed, these data extraction algorithms are all described in Liovic and Lakehal (2007). In the exponent the damping uses a third order polynomial on the gas side and a second order polynomial on the liquid side with coefficients extracted from Fulgosi et al. (2003). With this model the authors study wave breaking events and its interactions with turbulence and mean flow. Averaged velocity profiles are reported and the turbulent kinetic energy budget is plotted. Interestingly, during wave breaking events pressure diffusion terms and turbulent transport terms around become significant contributors to the turbulent kinetic energy budget.

All of these studies are of immense importance in the development of RANS models as they provide relevant statistics such as: mean profiles, Reynolds stresses, turbulence kinetic energy budget etc. Based on these data the constants in interpolation functions or damping terms can be adjusted. The changes in turbulent kinetic energy budget, especially the increased role of turbulent transport and pressure diffusion might mean that the gradient diffusion hypothesis which approximates these terms in the standard two-equation RANS formulation might no longer be valid.

6.6 Concluding remarks

The test cases performed show that the periodic CFD code based on the method presented in Chapter 3 can correctly predict stratified flows in laminar and turbulent regime, although in the latter case significant modelling difficulties were encountered. The development of better models is ongoing research.

From a commercial standpoint the CFD modelling of stratified flows in long pipelines is long-term research. This is mainly because simpler models and 1D codes are available that give robust estimates under these conditions e.g. the Biberg model. Therefore there is no direct incentive to supply such models but in the long run the future CFD modelling of multiphase flows must be able to predict these flows correctly. This would justify the use of CFD in more complex flow regimes, unsteady and local modelling of complex geometries cases where simpler models or 1D codes working with averaged equations might not work.

This long term goal is being advanced in the research community through DNS and, more recently, LES studies. The statistical structure of the boundary layer around the interface has been recently revealed and hence the multiphase community is in an analogous situation to the one formerly encountered in single phase research i.e. with the new data available there is an opportunity to develop better turbulence models. This avenue is explored in this study and leads to significant improvements

As for the method, the laminar results presented for two-dimensional flows are in agreement with the theoretical result. The three-dimensional version still requires some refinements in order to incorporate all the relevant physics.

On the turbulence modelling side, there is not enough evidence to stipulate that constants in Egorov model and its variation introduced above are mesh-dependant. The

most likely interpretation is a missing dependency on the physical parameters describing the flow. The situation seems to be analogous to wall modelling in RANS, where it was crucial to understand the local behaviour and introduce an approximation that captures the effect of it on the bulk flow. With the new contribution in DNS studies it should be soon possible to develop an equivalent of a wall-function that would be suitable for stratified flows in turbulent regimes.

Chapter 7

Summary

The research presented in this thesis addresses CFD modelling of single phase flow of non-Newtonian fluid and two-phase flow of Newtonian fluids. The standard turbulence models were examined and refined to account for non-Newtonian properties and interphase momentum and turbulence transfers. Although initial efforts to combine these sets of developments into a composite model, that is described in Chapter 1, were carried out in Section 6.4 a justification of the RANS results is difficult due to uncertainties with modelling the interfacial turbulence. The main contributions are therefore the improved models for non-Newtonian fluids, the implementation of periodic boundary conditions for two-phase flows and improved models of turbulence for stratified flows.

The last chapter of this thesis is divided as follows. In Section 7.1 all the results are collected and the main conclusions are drawn. Section 7.2 outlines possibilities for further refinements and developments.

7.1 Conclusions

- The standard wall function approach is not rheology-sensitive and does not agree well with the experimental friction factor curves available in the literature. To account for the non-Newtonian boundary layer different log-layer interpolation must be imposed leading to development and implementation of new wall functions. These non-Newtonian wall functions presented in this thesis can correctly reproduce the translation of friction factor curve and give more accurate predictions

of friction factors. The maximum improvement achieved was 35

- The mean rate of strain of instantaneous velocity field is larger than the rate of strain of the mean velocity field. This hypothesis was evaluated with the use of statistical inference methods and successfully passed all the tests. The analysis of DNS data shows that although the averaged rate of strain of the instantaneous field and the rate of strain of the averaged velocity field can be twice as large (and instantaneous values can be even 10 times larger), the corresponding change in viscosity results in molecular viscosity that is still much smaller than the effective viscosity caused by turbulent flow. Simple regularisations of the zero-shear singularity are usually sufficient for the accurate prediction of pipe flows. For some cases an improved model based on dimensional analysis and order of magnitude estimates gives improved predictions for power-law fluids.

- A new analysis presented in Chapter 5 which tests the hypothesis that under certain self-similarity assumptions the rate of strain of the fluctuating field has a log-normal distribution. This could lead to accurate models for effective molecular viscosity in turbulent flow. Statistical analysis of DNS data establishes that this assumption is valid only in a narrow region of the flow.

- For stratified, two-phase flow in a pipeline or channel a simulation on a full geometry can be approximated with a simulation of a pipe section. The geometry must be periodic in the streamwise direction. The problem is closed by applying periodic boundary conditions on both ends and by specifying mass fluxes for both phases. A novel solution procedure for periodic boundary is proposed. The procuedure gives correct liquid height, pressure gradient and velocity profiles for fully developed laminar flow in a channel. For the purpose of this validation an analytical expression for laminar case has been derived.

- The standard RANS models for two-phase flow become predict too high turbulence viscosity in the vicinity of the interface. This results in the prediction of pressure gradients are typically larger by around one order of magnitude than those reported in experimental investigations. A similar phenomenon was observed for LES models. DNS studies, on the other hand, reveal that turbulence around a flat interface behaves like turbulence in the vicinity of a moving wall.

Several corrections based on this observation are assessed in this study and a new approach was proposed. Improved predictions of pressure gradients and liquid heights were obtained.

- The Biberg model was implemented and applied for the cases obtained from the literature review. With an adjustment of turbulence level at the interface the Biberg model reproduced the pressure gradients, liquid heights and gave a very close approximation of velocity profiles. This demonstrates the necessity of modelling the turbulence level at the interface.

7.2 Suggestions for future work

- Low- and high-Reynolds number approaches to the turbulence level at the interface. The research carried out shows that the modelling of turbulence in the vicinity of the interface cannot be neglected and may lead to large discrepancies if not addressed. Ultimately the goal is to develop and implement a two-equation RANS model that would correctly predict the behaviour of turbulence statistics for two-phase stratified flow. The main challenge here is to describe correctly the behaviour of the flow at the interface. This would require advances in the fundamental understanding of phase interactions and gives an opportunity for original contributions in the theory of two-phase turbulence. Similarly to the wall modelling, wall function and damping function will arise as modelling tools which will act as mathematical models of local behaviour.

- Combine the presented approaches into a composite model. The composite model must be validated against experimental data. This can be carried out only when the uncertainties caused by the interface modelling are eliminated (in Newtonian cases). If this condition is not met, it will not be clear whether the results are an effect of the fluid rheology or the interface turbulence model.

- The development of a thermal boundary condition for two-phase flow. Inclusion of thermal calculations would enable us to investigate important two-phase flow scenarios that arise in long fluid conduits e.g. hydrate formation. Initial attempts

have been performed and are reported in Appendix C. Different types of thermal conditions necessitate different implementation of periodicity. A validation against DNS or experimental data will provide further insights and direction of development. It seems natural to expect similar difficulties in modelling the heat transfer at the interface.

- A two-layer implementation of wall function for non-Newtonian fluids. A two-layer wall function could further explore possible advantages of the known rheology. This could potentially make the model more accurate on a wider range of cases including complex flows.

- $\overline{v^2}$-f model for non-Newtonian fluids. Turbulence models may be formulated using different quantities characterising turbulence. The model based on the variance of the normal velocity component i.e. $\overline{v^2}$ has gained some acceptance. This model is described by quantities that have known and finite values at the wall. Moreover, these quantities are of direct use for the purpose of turbulent rate of strain estimates and could therefore be used to give an effective molecular viscosity model that accounts for the strain caused by the turbulent flow.

- The Biberg model with non-Newtonian fluids. The Biberg model does not integrate the momentum balance equations up to the laminar layer, but imposes a logarithmic profile in the vicinity of the wall and used friction factor expresions to obtain wall shear-stresses. It appears straightforward to change the logarithmic form to account for non-Newtonian behaviour and formulate a model for two-phase stratified flow with the liquid component having non-Newtonian properties.

This study was focused on RANS models and numerical techniques for non-Newtonian fluids and two-phase flows. Although many problems still remain open to further investigation, the presented contributions bring us several steps forward in the search for robust predictive tools and more accurate multiphase CFD. Due to diversity of the flow phenomena involved, both, the numerical and physical models, suffer from certain limitations and it is unlikely that any one methodology will prove to be applicable within the whole range of physical parameters that is of practical use. In this respect,

it is the author's hope that the novel work presented here, as well as other findings, will assist multiphase modellers in further development of this field.

References

Akai, M., Inoue, A. and Aoki, S. (1981), 'The prediction of stratified two-phase flow with a two-equation model of turbulence', *International Journal of Multiphase Flow* **7**(1), 21–39. ix, x, 128, 129, 134, 135, 137

Akai, M., Inoue, A., Aoki, S. and K., E. (1980), 'A co-current stratified air-mercury flow with wavy interface', *International Journal of Multiphase Flow* **6**(3), 173–190. 129, 192

Anderson, J. (1995), *Computational fluid dynamics: basics and applications*, McGraw-Hill Inc., US. 34

Anscombe, F. and Glynn, W. J. (1983), 'Distribution of the kurtosis statistic b_2 for normal statistics', *Biometrika* **70**(1), 227–234. 94

Arafin, S., George, A. and R.N., S. (2006), 'Equation of state of crude oil through temperature dependent ultrasonic measurements', *Chemical Engineering Science* **3**(7), 307–313. 181

Astarita, G. and Marrucci, G. (1974), *Principles of Non-Newtonian Fluid Mechanics*, McGraw-Hill Inc., US. 62

Batchelor, G. (1967), *An Introduction to Fluid Mechanics*. 34, 35

Beale, S. (2007), 'Use of streamwise periodic boundary conditions for problems in heat and mass transfer', *ASME Journal of Heat Transfer* **129**(4), 601–605. 42, 44

Biberg, D. (2007), 'A Mathematical Model For Two-Phase Stratified Turbulent Duct Flow', *Multiphase Science and Technology* **19**(1), 1–48. x, 107, 117, 120, 121, 130, 131

Biberg, D. (2011), Remarks on interfacial turbulence level. Private communication. 117

Biberg, D. and Halvorsen, G. (2000), 'Wall and interfacial shear stress in pressure driven two-phase laminar stratified pipe flow.', *International Journal of Multiphase Flow* **26**(10), 1645–1673. 114

Bird, B., Armstrong, R. and Hassager, O. (1987), *Dynamic of Polymeric Liquids*, John Wiley and Sons, New York. 66, 179

Bird, R., Stewart, W. and Lightfoot, E. (1960), *Transport Phenomena*, John Wiley & Sons. 114

Brennen, C. E. (2005), *Fundamentals of Multiphase Flow*, Cambridge University Press, New York. vii, 8, 110

Bruno, A. (1988), A Study of Interfacial Waves in Gas-Liquid Flows, PhD thesis, University of Notre Dame. xi, 130, 134, 138, 192, 193

Chhabra, R. P. (2006), *Bubbles, Drops, and Particles in Non-Newtonian Fluids*, CRC Press, London. 4, 63

Chhabra, R.P. amd Richardson, J. (2008), *Non-Newtonian Flow and Applied Rheology: Engineering Applications*, 2 edn, Butterworth-Heinemann, Oxford. 7

Chisholm, D. (1967), 'A theoretical basis for the lockhart-martinelli correlation for two-phase flow', *International Journal of Heat and Mass Transfer* **10**(12), 1767–1778. 109

Chung, B., Vaidya, A. and Wulandana, R. (2006), 'Stability of steady flow in a channel with linear temperature dependent viscosity', *International Journal of Applied Mathematics and Mechanics* **2**(7), 24–33. 181

Chung, T. J. (2002), *Computational fluid dynamics*, Cambridge University Press. 13

Clapp, R. (1961), Turbulent heat transfer in pseudoplastic non-newtonian fluids, *in* 'International Development in Heat Transfer', Vol. Part III, New York. viii, 68, 70, 72, 74, 75

Colebrook, C. (1939), 'Turbulent flow in pipes, with particular reference to the transition region between smooth and rough pipe laws', *Journal of the Institution of Civil engineers* **11**(4), 133:156. 56

D'Agostino, R. B. (1970), 'Transformation to normality of the null distribution of g_1', *Biometrika* **57**(3), 679–681. 94

D'Agostino, R. B., Belanger, A. and D'Agostino, Jr., R. B. (1990), 'A suggestion for using powerful and informative tests of normality', *The American Statistician* **44**(4), 316–321. 93

Darwish, M. (2010), Multphase Flows Numerics Workshop, *in* 'International Conference on Numerical Analysis and Applied Mathematics', AIP. 17

De Angelis, E., Casciola, C. M., L'vov, V. S., Piva, R. and Procaccia, I. (2002), 'Drag Reduction by Polymers in Turbulent Channel Flows: Energy Redistribution Between Invariant Empirical Modes', *Physical Review E - Statistical, Nonlinear and Soft Matter Physics* **67**(5 Pt 2), 056312. 65

De Angelis, V., Lombardi, P. and Banerjee, S. (1997), 'Direct numerical simulation of turbulent flow over a wavy wall', *Theoretical and Computational Fluid Dynamics* **9**(2), 2429. 140

de Berg, M., van Kreveld, M., Overmars, M. and Schwarzkopf, O. (2000), *Computational Geometry: Algorithms and Applications*, second edn, Springer-Verlag. 87

Dodge, D. and Metzner, A. (1959), 'Turbulent flow of non-newtonian systems', *AIChE Journal* **5**(2), 189–204. viii, 51, 67, 70, 72, 73, 74, 75

Doraiswamy, D. (2002), 'The origins of rheology: a short historical excursion', *Rheol. Bull.* **71**(7). 5

Dziubinski, M. (1995), 'A general correlation for two-phase pressure drop in intermittent flow of gas and non-newtonian liquid mixtures in a pipe', *Chemical Engineering Research and Design* **73**(5), 528–534. 112

Egorov, Y. (2004), Contact condensation in stratified stream-water flow, Technical report, ECORA. x, 129, 130, 131, 133

El-Emam, N., Kamel, A., El-Shafei, A. and El-Batrawy, A. (2003), 'New equation calculates friction factor for turbulent flow on non-newtonian fluids', *Oil and Gas Journal* **101**(36), 74. 67, 69, 70

Escudier, M. P., Poole, R. J., Presti, F., Dales, C., Nouar, C., Desaubry, C., Graham, L. and Pullum, L. (2005), 'Observations of asymmetrical flow behaviour in transitional pipe flow of yield-stress and other shear-thinning liquids', *Journal of Non-Newtonian Fluid Mechanics* **127**(2-3), 143–155. 100, 101, 102, 104, 105, 190, 191, 194

Escudier, M. and Presti, F.and Smith, S. (1999), 'Drag reduction in the turbulent pipe flow of polymers', *J. Non-Newtonian Fluid Mech* **81**, 197213. 191

Espedal, M. (1998), An Experimental Investigation of Stratified Two-Phase Pipe Flow at Small Inclinations, PhD thesis. 122

Farooqi, S. I. and Richardson, J. F. (1982), 'Horizontal flow of air and (liquid newtonian and non-newtonian)in a smooth pipe part ii: Average pressure drop', *ICHEME* **60**, 323–333. 111, 190

Ferziger, J. and Perić, M. (2002), *Computational Methods for Fluid Dynamics*, Springer. 13, 27, 40

Frantz, J. (2008), 'g3data', `http://www.frantz.fi/software/g3data.php`. 192

Fulgosi, M., Lakehal, D., Banerjee, S. and Angelis, V. (2003), 'Direct numerical simulation of turbulence in a sheared air-water with a deformable interface', *Journal of Fluid Mechanics* **482**, 319–345. 47, 140

Gaskell, P. H. and Lau, A. K. C. (1988), 'Curvature-compensated convective transport: SMART, A new boundedness- preserving transport algorithm', *International Journal for Numerical Methods in Fluids* **8**(6), 617–641. 18

Ghorai, S. and Nigam, K. (2006), 'CFD modeling of flow profiles and interfacial phenomena in two-phase flow in pipes', *Chemical Engineering and Processing* **45**(1), 55–65. 129

Gurvich, A.S. adn Yaglom, A. (1967), 'Breakdown of eddies and probability ditributions for small-scale turbulence', *Physics of Fluids* **10**, 59–65. 85

Handler, R. A., Swean, T. F., Leighton, R. I. and Swearingen, J. D. (1993), 'Length scales and the energy balance for turbulence near a free surface', *AIAA Journal* **31**(11), 1998–2007. 139

Hestens, M. and Stiefel, E. (1952), 'Methods of conjugate gradients for solving linear systems', *Journal of Research of the National Bureau of Standards* **49**(6), 409–436. 25

Heywood, N. I. and Charles, M. E. (1979), 'The stratified flow of gas and non-newtonian liquid in horizontal pipes', *International Journal of Multiphase Flow* **5**(5), 341–352. 111, 112, 113

Hinze, J. (1959), *Turbulence: an introduction to its mechanism and theory*, McGraw-Hill series in mechanical engineering, McGraw-Hill. 83

Hirt, C. and Nichols, B. (1981), 'Volume of fluid (VOF) method for the dynamics of free boundaries1', *Journal of Computational Physics* **39**(1), 201–225. 17

Holmås, K. and Biberg, D. (2007), Comparison of the Biberg analytical depth-integrated two-phase stratified flow model with CFD simulations, *in* '13th International Conference on Multiphase Production Technology'. ix, 129, 130

Hrenya, C., Bolio, E., Chakrabarti, D. and Sinclair, J. (1995), 'Comparison of low-reynolds k–ϵ turbulence models in predicting fully developed pipe flow', *Chemical Engineering Science* **50**(12), 1923–1941. 162

Hunt, J. (1984), *Turbulence structure and turbulent diffusion near gas-liquid interfaces*, pp. 67–82. 121

Issa, R. I. (1988), 'Prediction of turbulent, stratified, two-phase flow in inclined pipes and channels', *International Journal of Multiphase Flow* **14**(2), 141–154. ix, 129

Kawamura, H. (1998), 'DNS of turbulent heat transfer in channel flow with low to medium-high Prandtl number fluid', *International Journal of Heat and Fluid Flow* **19**(5), 482–491. 44

Kozuka, M., Seki, Y. and Kawamura, H. (2009), 'DNS of turbulent heat transfer in a channel flow with a high spatial resolution', *International Journal of Heat and Fluid Flow* **30**(3), 514–524. 44

Lakehal, D. and Liovic, P. (2011), 'Turbulence structure and interaction with steep breaking waves', *Journal of Fluid Mechanics* **674**, 522–577. 132, 133, 140

Lam, C. K. G. and Bremhorst, K. (1981), 'Modified form of the k- epsilon model for predicting wall turbulence', *Journal of Fluids Engineering, Transactions of the ASME* **103**(3), 456–460. Cited By (since 1996): 317. 59, 190

Lam, K. and Banerjee, S. (1992), 'On the condition of streak formation in a bounded turbulent flow', *Physics of Fluids A* **4**(2), 306–320. 139, 140

Landau, L. and Lifshitz, E. (1987), *Fluid Mechanics*, 2nd edn, Pergamon Press, Oxford. 34, 35, 178, 179

Launder, B. E. and Spalding, D. B. (1974), 'The numerical computation of turbulent flows', *Computer Methods in Applied Mechanics and Engineering* **3**(2), 269–289. 61

Leonard, B. (1991), 'The ULTIMATE conservative difference scheme applied to unsteady one-dimensional advection', *Computer Methods in Applied Mechanics and Engineering* **88**(1), 17–74. 16

Lin, M.-Y., Moeng, C.-H., Tsai, W.-T., Sullivan, P. P. and Belcher, S. E. (2008), 'Direct numerical simulation of wind-wave generation processes.', *Journal of Fluid Mechanics* **616**(-1), 1–30. 140

Liovic, P. and Lakehal, D. (2007), 'Multi-physics treatment in the vicinity of arbitrarily deformable gas–liquid interfaces.', *Journal of Computational Physics* **222**, 504–535. 132, 140

Lo, S. and Tomasello, A. (2010), Recent progress in CFD modelling of multiphase flow in horizontal and near-horizontal pipes, *in* '7th North America Multiphase Technology', Banff, Canada. 132, 133

Lockhart, R. and Martinelli, R. (1949), 'Proposed correlation of data for isothermal two phase two-compnent flow in pipes.', *Chem. Eng. Progress* **47**, 39–48. 108

Lombardi, P., De Angelis, V. and Banerjee, S. (1996), 'Direct numerical simulation of near-interface turbulence in coupled gas-liquid flow', *Physics of Fluids* **8**(6), 1643–1665. 47, 139

López, J., Hernandez, J., Gomez, P. and Faura, F. (2004), 'A volume of fluid method based on multidimensional advection and spline interface reconstruction', *Journal of Computational Physics* **195**(2), 718–742. 17

Lumley, J. (1964), 'Turbulence in non-newtonian fluids', *Physics of Fluids* **7**(3), 335–337. 65

Malin, M. (1997), 'Turbulent pipe flow of power-law fluids', *International Communications in Heat and Mass Transfer* **24**(7), 977–988. 98, 190

Malin, M. (1998), 'Turbulent pipe flow of herschel-bulkley fluids', *International Communications in Heat and Mass Transfer* **25**(3), 321–330. 99, 190

Martinelli, R. and Nelson, D. (1949), 'Prediction of pressure drop during forced circulation boiling of water', *Trans. ASME* **70**, 695–702. 108, 109

Marušić-Paloka, E. and Pažanin, I. (2009), 'Non-isothermal fluid flow through a thin pipe with cooling', *Applicable Analysis* **?**(?), 1–21. (to appear). 182, 186

Masson, E. and Gleize, V. (2004), Wall-distance free k-w turbulence model for compressible unsteady flows., *in* P. Neittaanmaki, T. Rossi, K. Majawa and O. Pironneau, eds, 'European Congress on Computational Methods in Applied Sciences and Engineering', ECCOMAS, 2004. 132, 133

MATLAB (2010), *version 7.10.0 (R2010a)*, The MathWorks Inc., Natick, Massachusetts. 171

Menter, F. (1994), 'Two-equation eddy-viscosity turbulence models for engineering applications', *AIAA Journal* **32**, 269–289. 133

Metzner, A. and Reed, J. (1955), 'Flow of non-newtonian fluids - correlation of the laminar, transition, and turbulent-flow regions', *AIChE Journal* **1**(4), 434–440. 67

Monin, A. and Yaglom, A. (1975), *Statistical Fluid Mechahnics*, Vol. 2, MIT Press, Cambridge. 84

Murthy, J. and Mathur, S. (1997), 'Periodic Flow And Heat Transfer Using Unstructured Meshes', *International Journal for Numerical Methods in Fluids1* **25**(6), 659–677. 42, 43, 44, 45

Muzaferija, S., Peric, M., Sames, S. and Schellin, T. (1999), A Two-Fluid Navier-Stokes Solver to Simulate Water Entry, *in* 'Twenty-Second Symposium on Naval Hydrodynamics', pp. 638–634. 18

Nagano, Y. and Hishida, M. (1987), 'Improved form of the k model for wall turbulent shear flows', *J. Fluid Eng.* p. 109156. 99, 191

Nagaosa, R. (1999), 'Direct numerical simulation of vortex structures and turbulent scalar transfer across a free surface in a fully developed turbulence', *Physics of Fluids* **11**(6), 1581. 139

Nagaosa, R. and Handler, R. A. (2003), 'Statistical analysis of coherent vortices near a free surface in a fully developed turbulence', *Physics of Fluids* **15**(2), 375–394. 139

Nikuradse, J. (1932), 'Gesetzmäßigkeiten der turbulenten Strömung in glatten Rohren. ', *Forschungsheft-Arb. Ing.-Wessen* **356**. 56, 76

Nikuradse, J. (1933), 'Strömungsgesetze in rauhen Rohren', *Forschungsheft-Arb. Ing.-Wessen* **361**. 56

Noh, W. and Woodward, P. (1976), SLIC (simple line interface calculation), *in* '5th International Conference on Numerical Methods in Fluid Dynamics', pp. 330–340. 17

Novikov, E. (1969), Scale similarity for random field, *in* 'Dokl. Akad. Nauk SSSR', Vol. 184, pp. 1072–1075. 85

Ozkan, F., Wenka, A. and Soyhan, H. S. (2007), 'Critical evaluation of CFD codes for interfacial simulation of bubble-train flow in a narrow channel', *International Journal for Numerical Methods in Fluids* **55**(6), 537–564. 18

Pan, Y. and Banerjee, S. (1995), 'A numerical study of free-surface turbulence in channel flow', *Physics of Fluids* **7**(7), 1649. 139

Panton, R. (1996), *Incompressible Flow*, 2nd edn. 34

Papanastasiou, T. (1987), 'Flows of materials with yield', *J. Rheol.* **31**, 385. 64

Patankar, S. (1980), *Numerical Heat Transfer and Fluid Flow*, Taylor & Francis. 13, 16, 17, 41

Patankar, S., Liu, C. and Sparrow, E. (1977), 'Fully Developed Flow and Heat Transfer in Ducts Having Streamwise-Periodic Variations of Cross-Sectional Area.', *ASME Journal of Heat Transfer* **99**(2), 180–186. 43

Patankar, S. and Spalding, D. (1972), 'A Calculation Procedure For Heat, Mass A nd Momentum Transfer In Three-Dimensional Parabolic Flows', *International Journal of Heat and Mass Transfe* **2**(10), 1787–1806. 42, 43

Phan-Thien, G. (2008), *Understanding Viscoelasticity: Basics of Rheology*, Springer, US. 66

Pilliod, J. (2004), 'Second-order accurate volume-of-fluid algorithms for tracking material interfaces*1', *Journal of Computational Physics* **199**(2), 465–502. 17

Pinho, F. T. (2003), 'A gnf framework for turbulent flow models of drag reducing fluids and proposal for a k-? type closure', *Journal of Non-Newtonian Fluid Mechanics* **114**(2-3), 149–184. 86, 99, 100, 104, 105, 190, 191, 194

Pinho, F. T., Li, C. F., Younis, B. A. and Sureshkumar, R. (2008), 'A low reynolds number turbulence closure for viscoelastic fluids', *Journal of Non-Newtonian Fluid Mechanics* **154**(2-3), 89–108. 65, 100

Pope, S. B. (2000), *Turbulent Flows*, Cambridge Press. 55, 100, 126

Prosperatti, A. and Tryggvason, G. (2006), *Computational Methods for Multiphase Flow*. 27

Rhyne, L. (2010), Personal communication. 190, 191

Rodi, W. and Mansour, N. (1993), 'Low-reynolds number k–ϵ modelling with the aid of direct simulation data', *Journal of Fluid Mechanics* **250**, 509–529. 162

Roe, P. (1985), Some contributions to the modelling of discontinuous flows, *in* B. Engquist, S. Osher and R. C. Somerville, eds, 'Large Scale Computations in Fluid Mechanics', Lectures in Applied Mathematics, American Mathematical Society, pp. 163–193. 19

Rudman, M. and Blackburn, H. M. (2006), 'Direct numerical simulation of turbulent non-newtonian flow using a spectral element method', *Applied mathematical modelling* **30**(2006), 1229–1248. 102, 190, 191

Rudman, M., Blackburn, H. M., Graham, L. J. W. and Pullum, L. (2004), 'Turbulent pipe flow of shear-thinning fluids', *Journal of Non-Newtonian Fluid Mechanics* **118**(1), 33–48. viii, ix, 86, 87, 88, 90, 93, 98, 100, 101, 103, 105, 191, 194

Rusche, H. (2002), Computational Fluid Dynamics of Dispersed Two-Phase Flows at High Phase Fractions, PhD thesis, Imperial College. 13, 26

Schlichting, H. (1955), *Boundary-Layer Theory*, McGraw-Hill, Inc., New York. 118

Shen, L., Zhang, X., Yue, D. K. P. and Triantafyllou, G. S. (1999), 'The surface layer for free-surface turbulent flows', *Journal of Fluid Mechanics* **386**, 167–212. 139

Sim, W.-G. (2006), 'Stratified Steady and Unsteady Two-Phase Flows Between Two Parallel Plates', *Journal of Mechanical Science and Technology* **20**(1), 125–132. 114

Smith, E., Robert, R. and McCready, M. (2010), Atomization of Stratified Turbulent Flow, *in* '7th International Conference on Multiphase Flow', Tampa. 192

Sureshkumar, R., Beris, A. N. and Handler, R. A. (1997), 'Direct numerical simulation of the turbulent channel flow of a polymer solution', *Physics of Fluids* **9**(3), 743–755. 65

Szilas, A., Bobok, E. and Navratil, L. (1981), 'Determination of turbulent pressure loss of non-newtonian oil flow in rough pipes', *Rheologica Acta* **20**(5), 487–496. 68, 69

Taitel, Y. and Dukler, A. (1976), 'A theoretical approach to the Lockhart–Martinelli correlation for stratified flow', *International Journal of Multiphase Flow* **2**(6), 591–595. 110, 173

Tennekes, H. and Lumley, J. (1972), *A First Course in Turbulence*, The MIT Press, USA, pp. 59–103. 53, 54, 55, 80, 82

Tiselj, I., Bergant, R., Mavko, B., Bajsic, I. and Hetsroni, G. (2001), 'DNS of Turbulent Heat Transfer in Channel Flow With Heat Conduction in the Solid Wall', *Journal of Heat Transfer* **123**(5), 849. 44

Toms, B. (1949), Some observations on the flow of linear polymer solutions through straight tubes at large reynolds numbers, *in* 'Proceedings of the International Congress on Rheology', Vol. 2, p. 135. 5, 65

Toro, E. (2009), *Riemann Sovers and Numerical Methods for Fluids Dynamics*, Springer. 13, 16

Tsai, W. T. (1998), 'A numerical study of the evolution and structure of a turbulent shear layer under a free surface', *Journal of Fluid Mechanics* **354**, 239–276. 139

Ubbink, O. and Issa, R. (1999), 'A Method for Capturing Sharp Fluid Interfaces on Arbitrary Meshes', *Journal of Computational Physics* **153**(1), 26–50. 18

Vaithianathan, T. (2003), 'Numerical approach to simulating turbulent flow of a viscoelastic polymer solution', *Journal of Computational Physics* **187**(1), 1–21. 65

Wilcox, D. (1988), 'Re-assessment of the scale-determining equation for advanced turbulence models', *AIAA Journal* **26**(11), 1299–1310. 36

Wilcox, D. (2006), *Turbulence Modeling for CFD*, Birmingham Press, San Diego, California. 61, 162

Xu, J., Wu, Y., Shi, Z., Lao, L. and Li, D. (2007), 'Studies on two-phase co-current air/non-newtonian shear-thinning fluid flows in inclined smooth pipes', *International Journal of Multiphase Flow* **33**(9), 948–969. 113, 138

Youngs, D. L. (1982), *Time-Dependent Multi-Material Flow with Large Fluid Distortion*, Academic Press, pp. 273–285. 17

Declaration

I herewith declare that I have produced this paper without the prohibited assistance of third parties and without making use of aids other than those specified; notions taken over directly or indirectly from other sources have been identified as such. This paper has not previously been presented in identical or similar form to any examination board.

The work was conducted from 2008 to 2012 under the supervision of Professor Chris Thompson at Applied Mathematics and Computing Group.

Cranfield University,

Appendix A

Low-Re models test

A. LOW-RE MODELS TEST

Standard k-ϵ model uses special interpolation schemes at the wall, called wall functions. These allow to perform the calculations on more coarse meshes, saving the computational time, but limiting the applicability of the model.
Low-Reynolds number models (for good survey papers see Rodi and Mansour (1993), Hrenya et al. (1995), Wilcox (2006)) integrate turbulence equations up to the viscous layer without the use of wall functions. Instead they use special damping terms in order to secure the right asymptotic behaviour of turbulence quantites.
2D calculations in FLUENT have been performed using two meshes: 32x128, 64x128. These meshes are rescaled so that the height of the mesh is 1m and the length is 10m. Axis boundary conditions are applied on the bottom edge of the mesh. Velocity inlet is used and the velocity is set to $1\frac{\mathrm{m}}{\mathrm{s}}$. Pressure boundary is used as outlet and wall bc is set on the top edge of the mesh. Solver is set for axisymmetric problems.
Density is normalised to 1 and the Reynolds number is varied by changing the viscosiy. Three different Reynolds numbers have been chosen for comparison:

1. Re = 100
2. Re = 1000
3. Re = 5000

All of the k-ϵ models are used in this study and compared against laminar viscosity model. Results are presented on figures A.1, A.2, A.3, A.4.

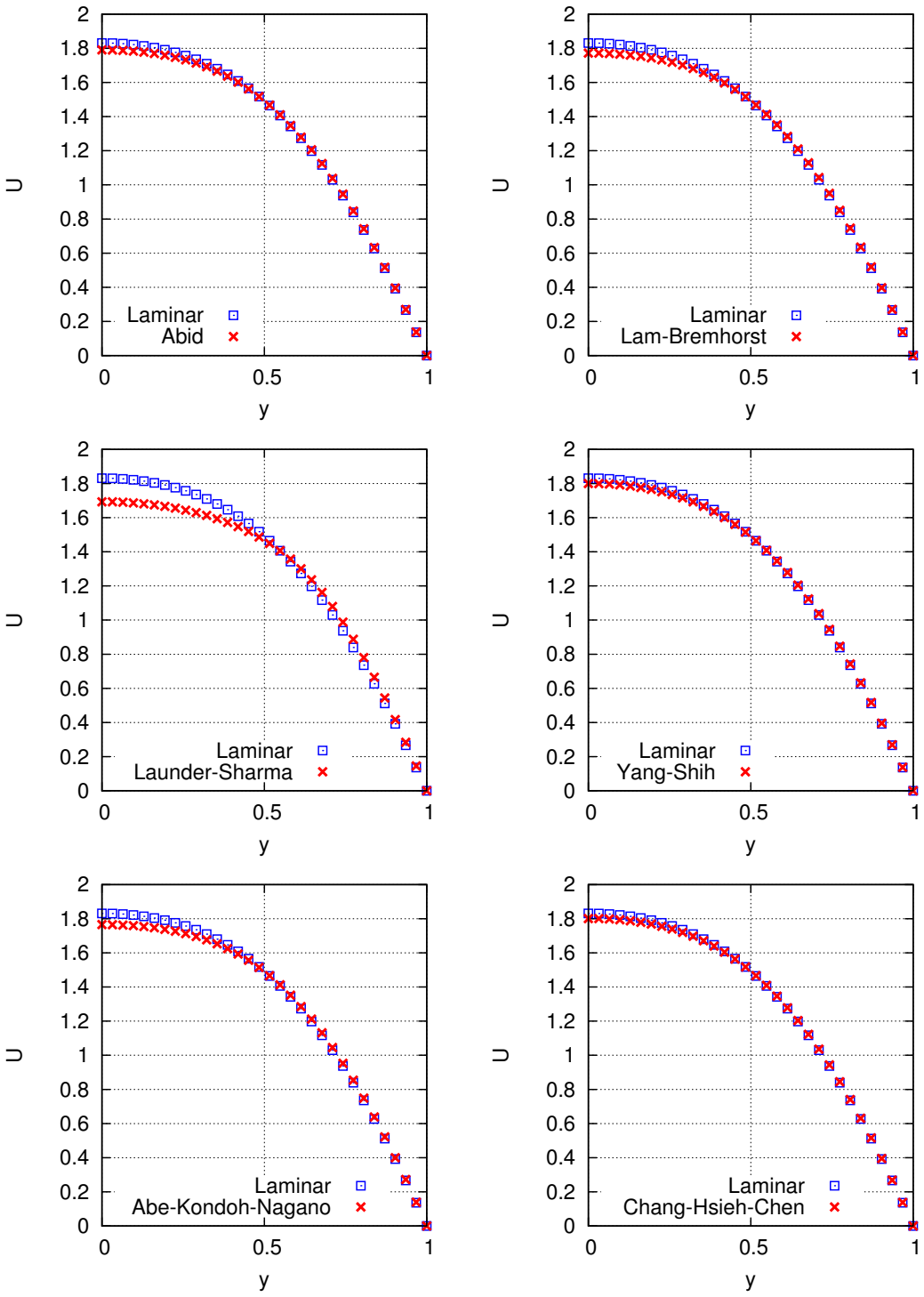

Figure A.1: Laminar profiles. Coarse mesh Re = 100

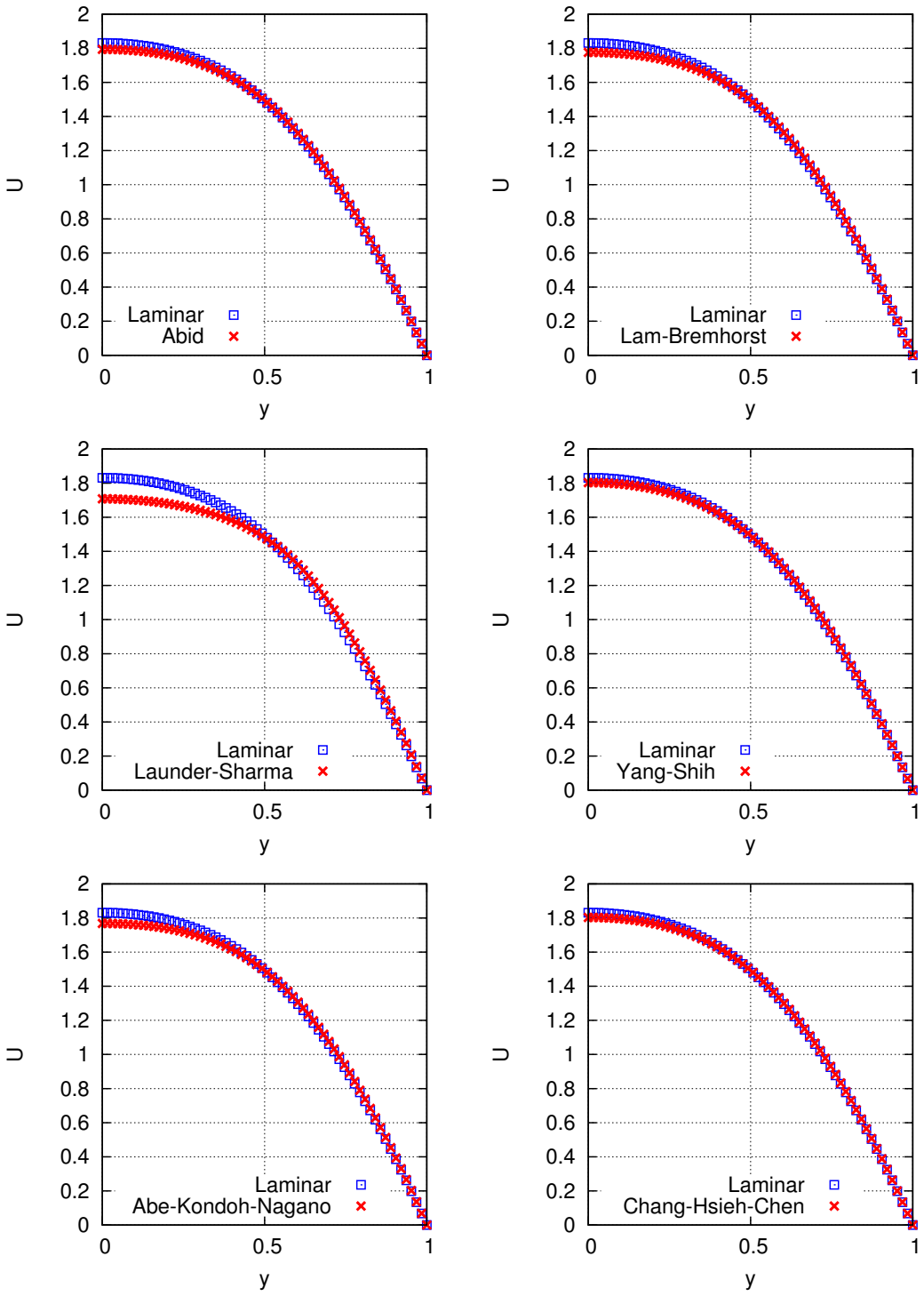

Figure A.2: Laminar profiles. Fine mesh Re = 100

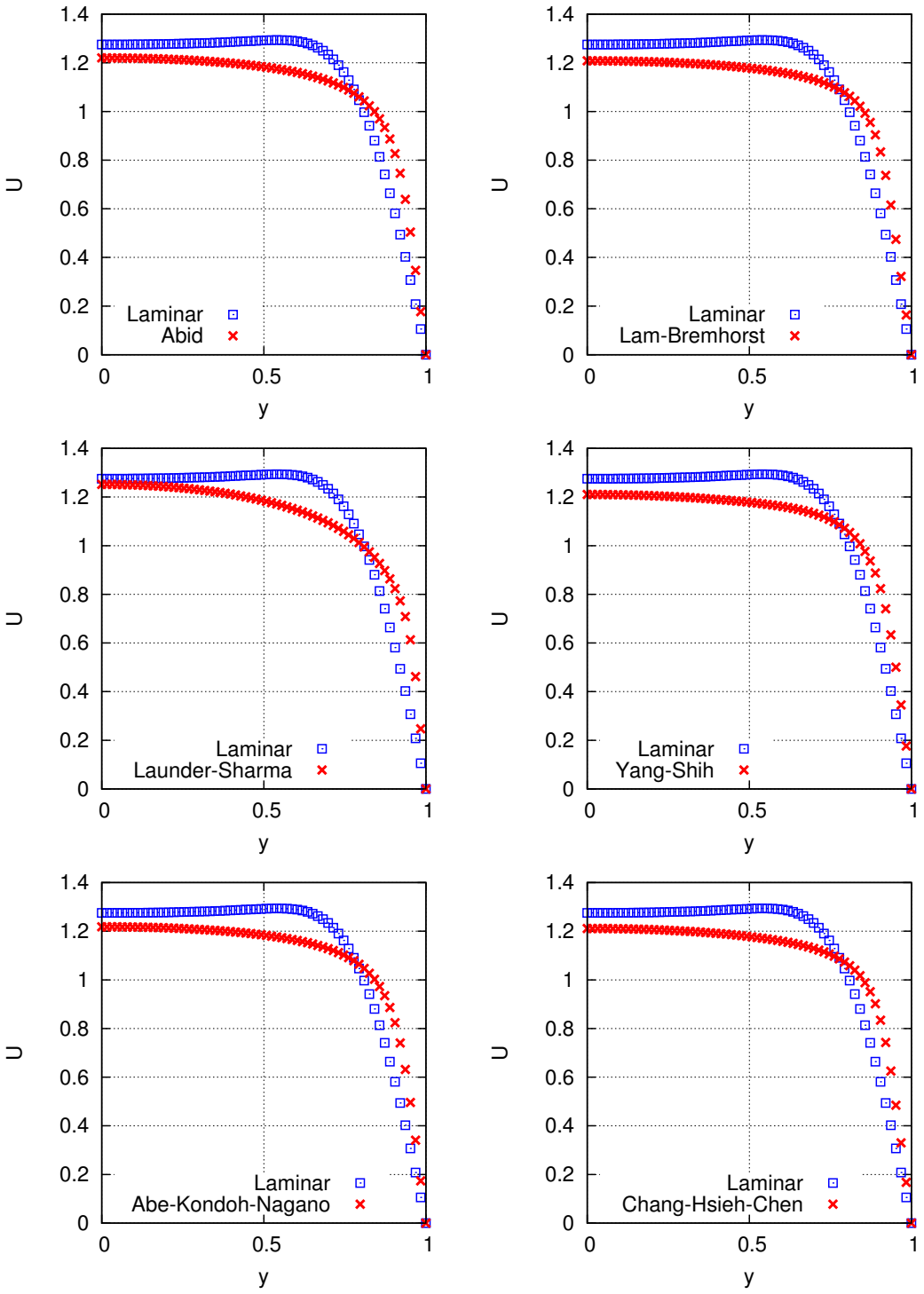

Figure A.3: Transitional profiles: fine mesh Re = 1000

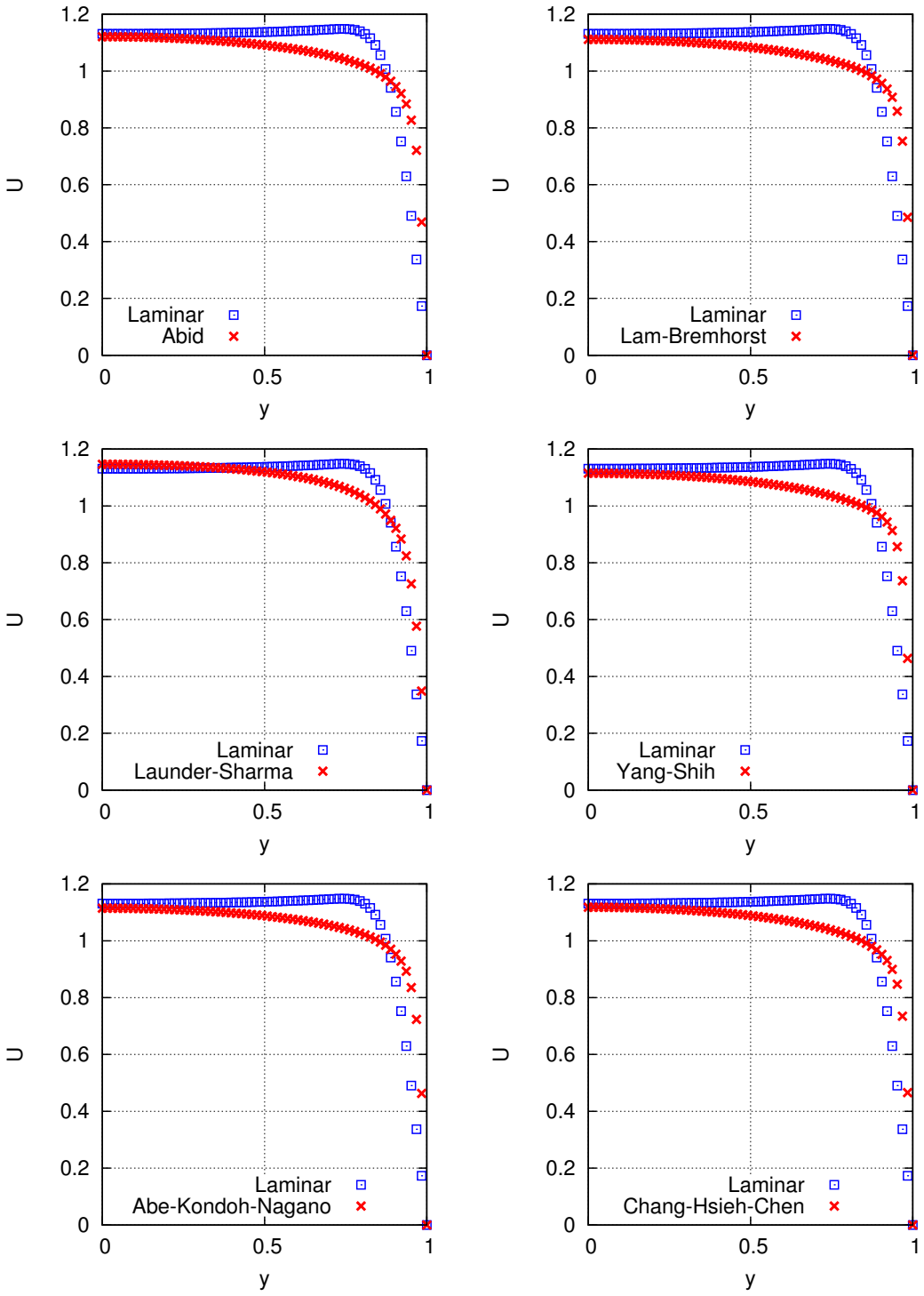

Figure A.4: Turbulent profiles. Fine mesh Re = 5000

All of the models correctly predict laminar profiles for low Reynolds numbers. As we go into transition laminar model "breaks" but low-Re still gives reasonable profiles. Turbulent profiles are also correctly predicted.
Further mesh refinement studies could be performed and the detailed study of transition region could be examined. This however has been covered by the existing literature (see below) and will not be pursued here.

Appendix B

Holdup and pressure drop correlations

File name	Comment
`eq1.m`	Gives a residual of Equation (6.33).
`Uprofile.m`	Calculates the velocity profile from Equation (6.28).
`interfaceVelocity.m`	Calculates the interface velocity from Equation (6.31)
`getPD.m`	Was used to create Figure. It contains an example of usage.

Table B.1: File list for laminar two-phase calculation profile and pressure drop calculation.

B.1 Laminar flow in a channel

The derivation of the velocity profile in a stratified channel flow is shown in Section 6.2.1. This section contains only a description of the files that are attached with the dissertation.

The files are to be used with MATLAB. The standard procedure is to use MATLAB in built functions for solving function handles. As for version 7.1 the default MATLAB method for solving a set of non-linear equations is Trust-Region Dogleg Method. Trust-Region Methods define a model function at each step and use the model function in order to choose the direction. Trust regions are introduced in order to limit the search space performed on the model function. If the model function gives a good approximation of the original function the trust region can be expanded. Contrariwise if the model function does not give a good approximation then the region is contracted. Simple thresholding is used in order to control this mechanism. The goal of this approach is to improve the robustness of the method, especially in cases where the initial guess is far from optimum and in regions where Jacobian might might be singular.

Matlab uses quadratic function as a model function. Instead of iterating a standard Newton method given by

$$F(x_k + d) = F(x) + J(x_k)d \tag{B.1}$$

where F is the function, x_k is the current search point, d is the direction and J is the Jacobian, MATLAB minimizes

$$m(d) = \frac{1}{2}F(x_k)^T F(x_k) + d^T J(x_k)^T F(x_k) + \frac{1}{2}d^T J(x_k)^T J(x_k)d \tag{B.2}$$

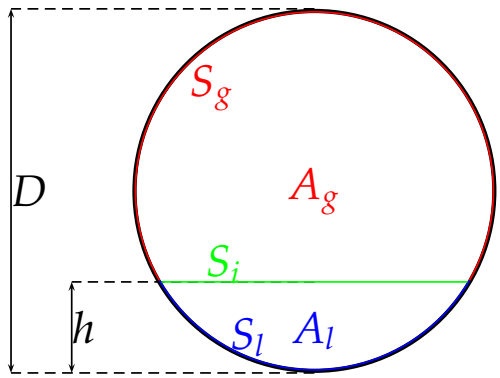

Figure B.1: Notation required for Taitel–Dukler method of calculating pressure gradients

on a trust region given such that $\|Dd\| < \Delta$, where D is the diagonal scaling and Δ is the region radius (nomenclature taken from MATLAB (2010)). Table B.1 is a list of files that were used to calculate laminar profiles.

B.2 Pipe flow with Taitel–Dukler correlation

Figure B.1 explains the notation used in Taitel–Dukler methodology. For a fully developed pipeline flow the momentum balance simplifies to:

$$-A_l \frac{\mathrm{d}p}{\mathrm{d}x} - S_l \tau_{wl} + \tau_i S_i = 0, \tag{B.3}$$

$$-A_g \frac{\mathrm{d}p}{\mathrm{d}x} - S_g \tau_{wg} - \tau_i S_i = 0, \tag{B.4}$$

where A_g is the area occupied by the gas, A_l is the area occupied by the liquid, whilst S_g and S_l are the wetted perimeters of gas and liquid respectively. S_i is the interface area. Since the pressure gradients is equal these two equations can be combined into one

$$\tau_{wg} \frac{S_g}{A_g} - \tau_{wl} \frac{S_l}{A_l} + \tau_i S_i \left(\frac{1}{A_L} + \frac{1}{A_G} \right) = 0 \tag{B.5}$$

The wall shear stresses are expressed in terms of friction factors:

$$\tau_{wg} = f_l \frac{\rho_l u_l^2}{2}, \qquad \tau_{wl} = f_g \frac{\rho_g u_l^2}{2}, \qquad \tau_{wi} = f_i \frac{\rho_g (u_g - u_l)^2}{2}. \tag{B.6}$$

The additional assumption is that $u_g \gg u_l$ and that $f_g \sim f_i$ so the interface shear stress becomes equal to gas wall shear-stress. The quantities describing the area are normalised with D^2 whilst the quantities described in length units are normalised with D. With some simple algebraic transformation the following formula can be derived:

$$\frac{f_l}{f_g}\frac{\rho_l \hat{u}_l^2}{\rho_g \hat{u}_g^2}\frac{\hat{S}_l}{\hat{A}_l}\hat{u}_l^2 + \left(\frac{\hat{S}_g}{\hat{A}_g} + \frac{f_i}{f_g}\left(\frac{\hat{S}_i}{\hat{A}_l} + \frac{\hat{S}_i}{\hat{A}_g}\right)\right)\hat{u}_l^2 = 0. \tag{B.7}$$

The Blasius equation is used for friction factors. It is expressed by:

$$f_g = C_g\left(\frac{u_g D_g}{\nu_g}\right)^{-n_g} \qquad f_g = C_l\left(\frac{u_l D_l}{\nu_l}\right)^{-n_l}, \tag{B.8}$$

where D_l and D_g are the hydraulic diameters. The parameters are chosen depending on the regime in which the phases are flowing. For laminar flow we have $C_P = 16$ and $n_P = 1$, where $P = g, l$, whilst for turbulent flow $C_P = 0.046$ and $n_P = 0.2$. The hydraulic diameters are expressed as $D_l = 4A_l/S_l$ and $D_g = 4A_g/(S_g + S_i)$. Subsisting this to the Equation (B.7)

$$-X^2\frac{(\hat{u}_l D_l)^{-n_l}}{(u_g D_g)^{-n_g}}\frac{\hat{S}_l}{\hat{A}_l}\hat{u}_l^2 + \left(\frac{\hat{S}_g}{\hat{A}_g} + \frac{f_i}{f_g}\left(\frac{\hat{S}_i}{\hat{A}_l} + \frac{\hat{S}_i}{\hat{A}_g}\right)\right)\hat{u}_l^2 = 0. \tag{B.9}$$

where X is the Lockhart–Martinelli parameter. Using trigonometry all the quantities can be expressed in terms of liquid height h.

$$\hat{A}_l = \frac{1}{4}\left(\pi - \arccos(2\hat{h}-1) + (2\hat{h}-1)\sqrt{1-(2\hat{h}-1)^2}\right) \tag{B.10}$$

$$\hat{A}_g = \frac{1}{4}\left((2\hat{h}-1)\sqrt{1-(2\hat{h}-1)^2}\right) \tag{B.11}$$

$$\hat{S}_l = \pi - \arccos(2\hat{h}-1) \tag{B.12}$$

$$\hat{S}_g = \arccos(2\hat{h}-1) \tag{B.13}$$

$$\hat{S}_i = \sqrt{1-(2\hat{h}-1)^2} \tag{B.14}$$

$$\hat{u}_l = \frac{\hat{A}}{\hat{A}_l} \tag{B.15}$$

$$\hat{u}_g = \frac{\hat{A}}{\hat{A}_g} \tag{B.16}$$

These relations can be subsisted into Equation (B.9) and Equation (B.9) can be then implicitly solved for $\hat{h}$. Note that the Lockhart-Martinelli paramter is the only input to this procedure.

File name	Comment
`getFrictionFactor.m`	Blasius expression for calculation of friction factors.
`bisection.m`	The implementation of bisection method. This serves the implicit solution of Equation (B.9)
`getDimensionless.m`	Calculates all non dimensional parameters given by equations Equations (B.10) to (B.16)
`dimensionlessPressureDrops.m`	Calculates the dimensionless pressure drop with Equation (B.17).
`eq7.m`	This is the residual of Equation (B.9) for a given set of input paramters. In Taitel and Dukler (1976) this equation was references as Eq. 7.
`circularSegmentArea.m`	Calculation of a circular segment area.
`taitel.ods`	OpenOffice spreadsheet for calculating Lockhart–Martinelli parameter for a give flow case.

Table B.2: File list for Taitel–Dukler scripts.

After the solution of Equation (B.9) the non-dimensional pressure gradient can be recovered from

$$\phi_g^2 = \frac{1}{4}\hat{u}_g^2 \frac{(\hat{u}_g D_g)^{-n_g}}{\hat{A}_g}\left(\hat{S}_g + \frac{f_i}{f_g}\hat{S}_i\right). \tag{B.17}$$

Figures B.2 and B.3 show the results for a range of Lockhart–Martinelli paramters calculated from the Taitel–Dukler method that was implemented in MATLAB. Moreover, a file list is given in Table B.2

B.3 Biberg model

Biberg model is described in section 6.2.2. To solve the equations of the model two bisection algorithm is requires i.e. the root search algorithm invokes another root search to evaluate the function. The model is solved in terms of R_g and h. Table B.3 gives a summary of the functions implemented. Apart from MATLAB scripts, Maxima files have been written in order to cross-check the results of the functions that are implemented at various stages of calculation procedure.

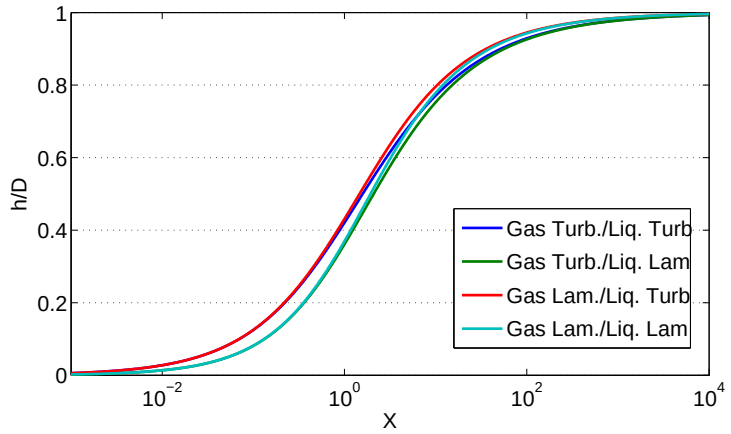

Figure B.2: Non-dimensional height as a function of Lockhard–Martinelli parameter.

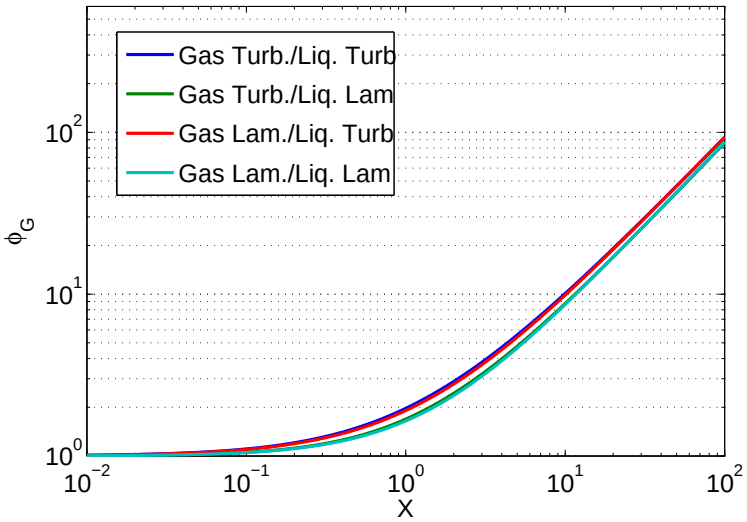

Figure B.3: Non-dimensional gas pressure gradient as a function of Lockhard–Martinelli parameter.

File name	Comment
`bisection.m`	Implementation of the bisection method.
`calcKgKlRl.m`	Calculation of gas and liquid interface turbulence level, and R_l.
`Eq39.m`	The dimensionless eddy viscosity profile for a single fluid.
`Eq48.m`	The dimensionless velocity profile for a single fluid.
`Eq51.m`	The dimensionless velocity profile translation Ψ.
`Eq59.m`	The dimensionless mean velocity for a single fluid.
`lambdaWall.m`	Wall friction factor.
`profiles.m`	The function calculating the profiles given liquid height and R_g.
`stratFlowFric.m`	OpenOffice spreadsheet for calculating Lockhart–Martinelli parameter for a give flow case.
`stratFlow.m`	The main function of this collection. It calculates the profiles, pressure gradient, liquid height, shear-stresses and other flow parameters, given superficial velocities, fluid properties and channel or pipeline dimensions.
`test.m`	A script containing example usage.

Table B.3: File list for Taitel–Dukler scripts.

Both versions i.e. channel and pipeline were implemented.

Appendix C

Heat transfer modelling

The general equation of heat transfer for a single phase flow is given by Landau and Lifshitz (1987):

$$\frac{\partial}{\partial t}\left(\frac{1}{2}\rho|\mathbf{U}|^2+\rho e\right)=\nabla\cdot\left(\rho\mathbf{U}\left(\frac{1}{2}\rho|\mathbf{U}|^2+\rho h\right)-k\nabla T\right), \tag{C.1}$$

where e is internal energy per unit mass, h is specific enthalpy and k is a coefficient of thermal conductivity. The terms on the right hand side represent respectively: the convective and conductive heat transfer. Viscous heating effect has been neglected.
With the help of thermodynamic relations the continuity and momentum equations Equation (C.1) can be expressed in terms of enthalpy alone. First, the left hand side can be rewritten as follows:

$$\frac{\partial}{\partial t}\left(\frac{1}{2}\rho|\mathbf{U}|^2+\rho e\right)=\frac{1}{2}|\mathbf{U}|^2\frac{\partial\rho}{\partial t}+\rho\mathbf{U}\cdot\frac{\partial\mathbf{U}}{\partial t}+\frac{\partial\rho}{\partial t}e+\rho\frac{\partial e}{\partial t}. \tag{C.2}$$

Now, some of the time derivatives can be expanded with the use of the momentum and continuity equations:

$$\begin{aligned}\frac{\partial}{\partial t}\left(\frac{1}{2}\rho|\mathbf{U}|^2+\rho e\right)=&-\frac{1}{2}|\mathbf{U}|^2\nabla\cdot\rho\mathbf{U}-\rho\mathbf{U}\cdot\nabla\frac{1}{2}|\mathbf{U}|^2-\mathbf{U}\cdot\nabla p\\&+e\nabla\cdot\rho\mathbf{U}+\rho\frac{\partial e}{\partial t},\end{aligned} \tag{C.3}$$

where the stress tensor has been neglected under the assumption that it is small compared with other terms. To remove time derivatives of e the relation $\mathrm{d}e = T\,\mathrm{d}s - p/\rho^2\,\mathrm{d}\rho$, where s stands for entropy, is used. This gives:

$$\frac{\partial e}{\partial t}=T\frac{\partial s}{\partial t}+\frac{p}{\rho^2}\frac{\partial\rho}{\partial t}=T\frac{\partial s}{\partial t}+\frac{p}{\rho^2}\nabla\cdot\rho\mathbf{U}. \tag{C.4}$$

Now, using the definition of enthalpy $h = e + p/\rho$, e can be removed from the above equation to give:

$$\begin{aligned}\frac{\partial}{\partial t}\left(\frac{1}{2}\rho|\mathbf{U}|^2+\rho e\right)=&-\left(\frac{1}{2}|\mathbf{U}|^2+h\right)\nabla\cdot\rho\mathbf{U}-\rho\mathbf{U}\cdot\nabla\frac{1}{2}|\mathbf{U}|^2-\mathbf{U}\cdot\nabla p\\&+\rho T\frac{\partial s}{\partial t}.\end{aligned} \tag{C.5}$$

The entropy is removed with the aid of relation $\mathrm{d}h = T\,\mathrm{d}s + \mathrm{d}p/\rho$:

$$\begin{aligned}\frac{\partial}{\partial t}\left(\frac{1}{2}\rho|\mathbf{U}|^2+\rho e\right)=&-\left(\frac{1}{2}|\mathbf{U}|^2+h\right)\nabla\cdot\rho\mathbf{U}-\rho\mathbf{U}\cdot\nabla\frac{1}{2}|\mathbf{U}|^2+\rho\frac{\partial h}{\partial t}\\&-\frac{Dp}{Dt},\end{aligned} \tag{C.6}$$

where a symbol of material derivative $\frac{D}{Dt}$ has been used to simply the notation. Now adding and subtracting $\rho\mathbf{U}\cdot\nabla h$ the equation can be simplified to:

$$\frac{\partial}{\partial t}\left(\frac{1}{2}\rho|\mathbf{U}|^2+\rho e\right)=-\nabla\cdot\left(\rho\mathbf{U}\left(\frac{1}{2}|\mathbf{U}|^2+h\right)\right)+\rho\frac{\partial h}{\partial t}+\rho\mathbf{U}\cdot\nabla h-\frac{Dp}{Dt}, \tag{C.7}$$

which after substitution in Equation (C.1) gives:

$$\rho\left(\frac{\partial h}{\partial t}+\mathbf{U}\cdot\nabla h\right)=\nabla\cdot k\nabla T+\frac{Dp}{Dt}. \tag{C.8}$$

For an incompressible fluid the energy equation can be simplified (see Landau and Lifshitz (1987) and solved for temperature only. At constant pressure the thermodynamic relationship gives:

$$\left(\frac{\partial h}{\partial T}\right)_p=c_p, \tag{C.9}$$

where c_p is the specific heat capacity. Using chain rule we obtain:

$$\frac{\partial h}{\partial t}=\left(\frac{\partial h}{\partial T}\right)_p\frac{\partial T}{\partial t}. \tag{C.10}$$

This means that Equation (C.8) can be transformed to:

$$\rho c_p\left(\frac{\partial T}{\partial t}+\mathbf{U}\cdot\nabla T\right)=\nabla\cdot k\nabla T \tag{C.11}$$

which can be used in the context of two-phase flow if no phase transitions are expected.

C.1 Temperature effect on viscosity

The standard approach to fluid dynamic problem is to assume that all material parameters are constant. The discussion above relates the changes of viscosity in terms of strain rate or more general the relation between stress and strain rates. In this section we will look at variation of viscosity function with relation to temperature.

According to Bird et al. (1987) the variation of these density and viscosity is much more pronounced pronounced than variation of any other. The literature supplies us with several expressions relating temperature to viscosity. Most of them are purely empirical however after exposition of the models of strain rate and stress it is obvious that correlating temperature history would be also possible (and in fact was postulated by Oldroyd!).

Piecewise-polynomial

$$\begin{aligned} &\text{for} \quad T \in [T_{\min,1}, T_{\max,1}] \quad T = a_{1,1} + a_{1,2}T + \dots \\ &\qquad\qquad\qquad\qquad \vdots \\ &\text{for} \quad T \in [T_{\min,k}, T_{\max,k}] \quad T = a_{k,1} + a_{k,2}T + \dots \end{aligned} \tag{C.12}$$

Power-law

$$\frac{\mu}{\mu_0} = a\left(\frac{T}{T_0}\right)^b \tag{C.13}$$

Exponential-law

$$\frac{\mu}{\mu_0} = a\exp\left(b\frac{T}{T_0}\right) \tag{C.14}$$

Sutherland's law based on kinetic theory

$$\mu = \frac{aT^{3/2}}{T+b} \tag{C.15}$$

It is now worth spending a while to develop a non-dimensional governing equations of flows with temperature related viscosity.

C.1.1 Governing equations

We confine our attention to steady flows. Variations of density are assumed to be negligible with the exception of buoyancy term where we assume that temperature variation can lead to small differences in density approximated by a first order Taylor expansion (Boussinesq approximation).
We assume a temperature dependant viscosity. Possible constitutive laws relating temperature to viscosity are given at the end of this section.

$$\frac{\partial u_j}{\partial x_j} = 0 \tag{C.16}$$

$$\rho u_j \frac{\partial u_i}{\partial x_j} = -\frac{\partial p}{\partial x_i} + \frac{\partial}{\partial x_j}\left(\mu(T)\dot{\gamma}_{ij}\right) + \rho g_i \beta (T - T_\infty) \tag{C.17}$$

$$\rho C_p u_j \frac{\partial T}{\partial x_j} = \frac{\partial}{\partial x_j} k \frac{\partial T}{\partial x_j} + \frac{1}{2}\mu(T)\left(\frac{\partial u_i}{\partial x_j}\frac{\partial u_j}{\partial x_i}\right) \tag{C.18}$$

where ρ density, $\mu(T)$ is a temperature dependant viscosity, k is a conductivity, C_p is heat capacity, β is heat expansion coefficient and $\dot{\gamma}_{ij}$ is strain rate given by:

$$\dot{\gamma}_{ij} = \frac{1}{2}\left(\frac{\partial u_j}{\partial x_i} + \frac{\partial u_i}{\partial x_j}\right) \tag{C.19}$$

The boundary conditions we would like to impose on this system are the following:

$$k\frac{\partial T}{\partial n} = h(T_\infty - T),\ \boldsymbol{u} = 0 \qquad \text{at the wall} \tag{C.20}$$

$$T = T_0 \quad \text{at the inlet} \tag{C.21}$$

where h is the heat transfer coefficient and T_∞ is the temperature of the surrounding of the pipe. The form of this condition corresponds to so called Newton's cooling law. We assume that it is much lower than temperature of the pipe by imposing $T_\infty = \mathcal{O}(\epsilon)$. Therefore we can say that Neumann boundary conditions were applied for the pipe wall and Dirichlet boundary conditions at the inlet. For this problem formulation existence and uniqueness of weak solution has been proved under certain circumstances (see e.g. Chung et al. (2006)).

One of the possible non-diemnsionalisation can be given by:

$$\hat{u_i} = \frac{u_i}{U_0}, \qquad \hat{x_i} = \frac{x_i}{R}, \quad \hat{p} = \frac{Rp}{\mu_0 U_0}, \quad \hat{T} = \frac{T - T_\infty}{T_0 - T_\infty}. \tag{C.22}$$

With these variables and with a little bit of terms rearrangement to form non-dimensional groups we obtain:

$$\frac{\partial \hat{u}_i}{\partial \hat{x}_i} = 0, \tag{C.23}$$

$$\mathrm{Re}\,\hat{u}_j\frac{\partial \hat{u}_i}{\partial \hat{x}_j} = -\frac{\partial \hat{p}}{\partial \hat{x}_i} + \frac{\partial}{\partial \hat{x}_j}\left(\frac{\mu(T)}{\mu_0}\dot{\hat{\gamma}}_{ij}\right) + \frac{\mathrm{Gr}}{\mathrm{Re}}\hat{T}, \tag{C.24}$$

$$\mathrm{Pé}\,\hat{u}_j\frac{\partial \hat{T}}{\partial \hat{x}_j} = \frac{\partial \hat{T}}{\partial x_i \partial x_i}\hat{x}_i + \frac{1}{2}\mathrm{Br}\left(\frac{\mu(T)}{\mu_0}\right)\left(\frac{\partial \hat{u}_i}{\partial \hat{x}_j}\frac{\partial \hat{u}_j}{\partial \hat{x}_i}\right), \tag{C.25}$$

and the non-dimensional numbers are:

$$\mathrm{Re} = \frac{\rho U_0\, R}{\mu_0} \quad \mathrm{Gr} = \frac{g\beta R^3(T_\infty - T_0)\rho^2}{\mu_0^2}, \quad \mathrm{Pé} = \frac{\rho C_p R U_0}{k}, \quad \mathrm{Br} = \frac{\mu_0 U_0^2}{k(T_\infty - T_0)}, \tag{C.26}$$

where reference scales denoted by subscript zero are chosen based on the problem or information we are seeking. To describe the average behaviour in the cross-section we take U_0 as bulk velocity, μ_0 as bulk viscosity and R the radius of a pipe.

It is clear from these equations that the buoyancy contribution compared to momentum transport can be measured by the ratio:

$$\frac{\mathrm{Gr}}{\mathrm{Re}^2} = \frac{g\beta R(T_\infty - T_0)}{U_0^2} \tag{C.27}$$

The value of temperature expansion coefficient was based on Arafin et al. (2006)

C.1.2 Reference scale

The presented equations pose several problems related to scaling. Because of the non-trivial rheology of the fluid in question it is uncertain if reference scales should refer to the process scales (e.g. wall temperature) or to rheology of the fluid (e.g. temperature required to achieve reference viscosity).
The choice of temperature non-dimensionalization was arbitrary and related to the the process values, but for completeness and perhaps future use let us also present other possibilities:

$$\begin{aligned} \Delta T_1 = T_\infty - T_w, \quad \Delta T_2 = \frac{\Delta p}{\rho C_p} \\ \Delta T_3 = \frac{\mu U_0^2}{\rho k}, \quad \Delta T_4 = \left| \frac{\mu}{\partial \mu / \partial T} \right|_{T=T_0}. \end{aligned} \tag{C.28}$$

ΔT_1 is the process temperature difference scale referring to boundary conditions. ΔT_2 is an adiabatic temperature of the process. ΔT_3 is the temperature required to balance viscous heating and conduction terms and ΔT_4 is a temperature difference required to make a substantial change to viscosity. Notice that it still requires a value of reference temperature.

C.1.3 Main analytical results

An asymptotic analysis for the above case for negligible viscous heating has been conducted in Marušić-Paloka and Pažanin (2009). Additionally it has been assumed that the temperature of the surrounding T_∞ and conduction parameter k varies with axial coordinate x_1. The analysis has been performed in the limit of a thin pipe. The parameter ϵ of the expansion was the thickness of the pipe, while the length of the pipe was assumed to be of the order of one. This result is equally valid for a long pipe with small ratio of thickness to length. The variables have normalised in order to eliminate pressure and heat capacity from the equation.

$$\begin{aligned} T_\epsilon(\mathbf{x}) = \theta_0(x_1) + B_0\left(\frac{x_1}{\epsilon}, \frac{x'}{\epsilon}\right) + H_0\left(\frac{x_1 - l}{\epsilon}, \frac{x'}{\epsilon}\right) \\ \epsilon\left(\theta_1(x_1) + B_1\left(\frac{x_1}{\epsilon}, \frac{x'}{\epsilon}\right) + H_1\left(\frac{x_1 - l}{\epsilon}, \frac{x'}{\epsilon}\right)\right) + \epsilon^2\theta_2\left(x_1, \frac{x'}{\epsilon}\right) \end{aligned} \tag{C.29}$$

where $x^{'} = (x_2, x_3)$ are the cross-section coordinates of the pipe. B_n and H_n are the n'th order corrections to the boundary layer due to outlet and inlet boundary conditions. and θ_n are the terms of the expansions which are the unique solutions of the boundary value problems for the following ODEs:

$$\begin{cases} \left(k\theta_0^{'}\right)^{'} - 2\gamma\theta_0 = 0,\ \gamma = \frac{h}{\epsilon} = \mathcal{O}(1) \\ \theta_0(0) = \frac{1}{\pi}\int_B T_\infty(y^{'}), \theta_0(l) = \frac{1}{\pi}\int_B T_\infty(y^{'}),\ y^{'} = x^{'}/\epsilon) \end{cases} \tag{C.30}$$

$$\begin{cases} \left(k\theta_1^{'}\right)^{'} - 2\gamma(T_\infty - \gamma\theta_1) = 0, \\ \theta_1(0) = \frac{k^{'}(0)}{\pi k(0)}\int_0^\infty s\int_B \frac{\partial B_0}{\partial y^{'}}(s,\cdot)\,\mathrm{d}s, \theta_0(l)\frac{k^{'}(l)}{\pi k(l)}\int_{-\infty}^0 s\int_B \frac{\partial H_0}{\partial y^{'}}(s,\cdot)\,\mathrm{d}s, \end{cases} \tag{C.31}$$

where $\theta_2 = -\frac{1}{4}\frac{\left((k(x_1)\theta_0^{'}\right)^{'}}{k(x_1)}|y^{'}|^2$. Prime denotes the derivative with respect to axial coordinate x_1. Parameter γ in Equation (C.30) confines our attention to the only non-trivial case namely the one when the variation of temperature is present throughout the pipe. If this condition is not satisfied the temperature is either dominated by inlet boundary condition with almost no heat transfer through the wall or the liquid is cooled very quickly so that no variation of temperature and therefore the viscosity gradient are not negligible.

The approximation for velocity and pressure are given by:

$$u_\epsilon(\mathbf{x}) = \frac{1}{2\mu(\theta_0)}\left(1 - \frac{|x^{'}|^2}{\epsilon^2}\right)\left(f_1(\bar{W}) - P_0^{'}\right)\mathbf{e_1} \tag{C.32}$$

$$p_\epsilon(x_1) = -C_1\int_0^{x_1}\mu(\theta_0(\xi))\,\mathrm{d}\xi + \int_0^{x_1} f_1(\bar{W}(\xi))d\xi + q_0 \tag{C.33}$$

where $\bar{W}(x_1) = \theta_0(x_1) - \frac{1}{l}\int_0^l \theta_0(\xi)d\xi$ and

$$C_1 = \left(q_0 - q_l + \int_0^{x_1} f_1(\bar{W}(\xi))\,\mathrm{d}\xi\right)\left(\int_0^{x_1}\mu(\theta_0(\xi))\,\mathrm{d}\xi\right)^{-1}$$

The error analysis of the above solution leads to the following results:

$$V^{-1/2}\|T - T_\epsilon\| = \mathcal{O}(\epsilon\sqrt{\epsilon}) \tag{C.34}$$

$$V^{-1/2}\|\epsilon^{-2}u_1 - u_\epsilon\| = \mathcal{O}(\epsilon), V^{-1/2}\|\epsilon^{-2}p_1 - p_\epsilon\| = \mathcal{O}(\epsilon) \tag{C.35}$$

where V is the volume of the pipe and the symbol $\|\cdot\|$ should be understood as $L^2(\mathbb{R})$ norm.

C.2 Periodicity in heat transfer

In a subsea pipeline we usually face a problem of transporting hot material in a cold environment. The material transported cools down as it progresses through the pipe. There are two types of heat transfer mechanism involved. One comes from convection caused by the hot material moving through the domain. The second mechanism removes the heat through the pipe wall releasing it to the environment. The third possible mechanism would be viscous heating but in this case it is assumed to be negligible.
As the temperature of the material approaches ambient temperature less and less heat is being released and therefore the assumption of constant heat flux is invalid. Imposition of the wall temperature is also dubious since sufficiently close to the inlet the temperature will be dominated by inlet fluid temperature and initial sections might not contain any region where the temperature is equal to temperature of the environment. For the momentum equations the periodic boundary conditions are specified as in Chapter 3. Only the treatment of temperature will be considered here.
Obviously, the heat transfer does not admit a periodic solution. In the subsea pipeline example we see that the surrounding will remove the heat from the pipeline. Each adjacent cross-section will contain less thermal energy. However the evolution of the thermal profile might still be periodic under suitable rescaling. In other words the temperature will be different but the shape of temperature profile might be the same. In order to examine this resemblance we need to introduce some local reference quantity. For this purpose the mass averaged temperature is considered here. Depending on the choice of wall boundary conditions, different rescaling have to be used. Three posibilities for wall boundary conditions are:

- Fixed wall temperature or Dirichlet condition for temperature

$$T\big|_{x=\text{wall}} = T_w, \tag{C.36}$$

  where T_w is a wall temperature that needs to be specified.

- Fixed wall heat flux or Neumann condition for temperature

$$k\frac{\partial T}{\partial n} = q_w, \tag{C.37}$$

  where q_w is the wall heat flux that needs to be specified.

- Newton's Cooling law or Robin condition for temperature

$$k\frac{\partial T}{\partial n} = \beta(T - T_a), \tag{C.38}$$

  where T_a is an ambient temperature and β is a heat transfer coefficient that needs to be specified.

Moreover, the mass averaged temperature at the cross-section is defined

$$T_b(x) = \frac{\int_{B(x)} T\rho\mathbf{u}\cdot\ \mathrm{d}\mathbf{S}}{\int_{B(x)} \rho\mathbf{u}\cdot\ \mathrm{d}\mathbf{S}}, \tag{C.39}$$

where $B(x)$ is the set of points in the cross-section located at x, where x is the streamwise coordinate.

Only the fixed wall temperature will be considered here. The normalisation for this case takes the form:

$$\theta = \frac{T - T_w}{T_b(x) - T_w}. \tag{C.40}$$

Introducing a non-dimensional bulk temperature streamwise gradient as:

$$\lambda(x) = \frac{1}{T_b(x) - T_w}\frac{\partial T_b}{\partial x}, \tag{C.41}$$

the temperature equation can be recast into the non-dimensional form as follows:

$$u_1\frac{\partial\theta}{\partial x} + u_2\frac{\partial\theta}{\partial y} - \alpha\left(\frac{\partial^2\theta}{\partial x^2} + \frac{\partial^2\theta}{\partial y^2}\right) = \lambda\left(2\alpha\frac{\partial\theta}{\partial x} - u_1\theta\right) + \alpha\theta\left(\lambda^2 + \frac{\partial\lambda}{\partial x}\right), \tag{C.42}$$

where $\alpha = k/(\rho c_p)$ is the thermal diffusivity coefficient.

The problem that now appears is the new variable i.e. function λ. To obtain λ Equation (C.42): is first solved for θ with a guessed λ. Next, the advantage is taken of the fact that for every cross-section a quantity

$$\Omega(x) = \frac{\int_{B(x)} \rho u_1\theta\ \mathrm{d}x}{\int_{B(x)} \rho u_1\ \mathrm{d}x} \tag{C.43}$$

should be exactly one. The solution of Equation (C.42) does not have to satisfy this constraint. Therefore, after solving Equation (C.42) for θ, Ω is calculated for each section and the following variable transformation is employed:

$$\theta(x,y)^* = \frac{\theta(x,y)}{\Omega(x)}. \tag{C.44}$$

Afterwards θ^* is substituted into Equation (C.42) as θ and the same equation is solved now for λ. The procedure iterates until the steady state is reached.

C.3 Results

The parameters of the momentum equation solver were set in the same way as in . In this study a constant temperature wall was set to 277 K. The inlet bulk temperature is used as an additional constraint for the inlet temperature. Four different inlet temperatures are set: 299 K, 307 K, 347 K.

Figure C.1 and Figure C.2 show the results that were obtained with the method described above. The self-similarity of the solution, which was the underlying assumption of the method, is clearly manifested in the temperature profiles. The magnitude of the change between various inlet temperatures seems to be consistent, however the peak temperature in the cross-section is much higher than expected. Further testing is required in order to prove the efficiency of the method or in order to identify possible flaws in the methodology. The asymptotic solution by Marušić-Paloka and Pažanin (2009) in previous section is a viable route for a thorough validation.

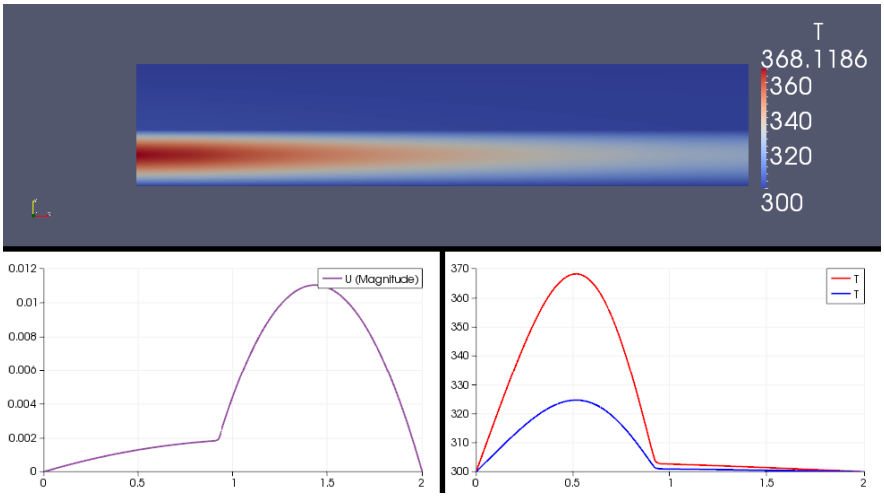

Figure C.1: Top: temperature variation in a 10 diameter long channel section. Bottom left: laminar velocity profile. Bottom right: temperature at the outlet and the inlet of the section. Self-similar solution was obtained.

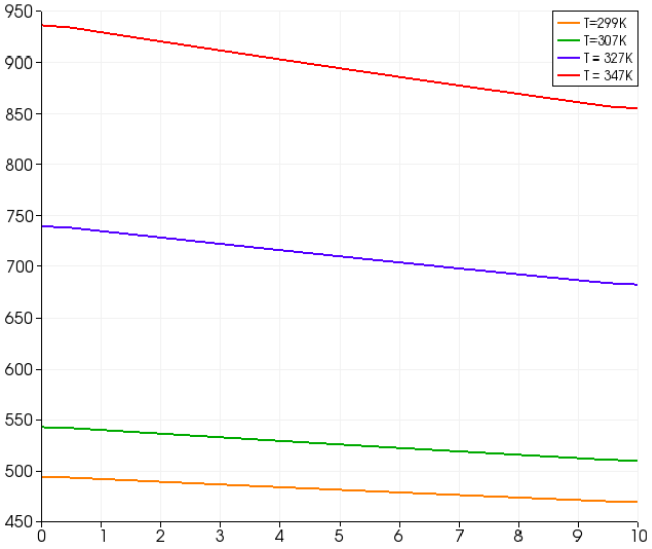

Figure C.2: Comparison of maximum temperature for different inlet bulk temperatures.

Appendix D

Data collected from the literature review

D. DATA COLLECTED FROM THE LITERATURE REVIEW

Table D.1: Form and content of obtained data sets

Source	Type	Content
Farooqi and Richardson (1982)	Tables	friction factors, two-phase flow
Pinho (2003)	CSV	1D velocity field, turbulence scalar fields, wall coordinates
Rudman and Blackburn (2006)	CSV	3D velocity field, 3D viscosity field, 3D Reynolds stress field for a given pressure drop
Rudman and Blackburn (2006)	Graphs	1D velocity field, turbulence scalar fields
Escudier et al. (2005)	xls	rheology and 1d velocity fields
Rhyne (2010)	Tables	two-phase flow, friction factors, superficial velocities, animations

During the last year literature review a following set of relevant data has been identified.

1. Farooqi and Richardson (1982) has conducted an experimental investigation to establish the effect of non-Newtonian rheology in liquid/gas flow. The flow in stratified regime with gas being either laminar or turbulent and liquid remaining only in laminar state. The data comprise fluids rheology, flow rates and corresponding pressure drops.

2. Malin (1997) and Malin (1998) were, to the best of author's knowledge, the first simulations of turbulent flows taking non-Newtonian properties into account. Malin uses power-law and Herschel–Bulkley fluids. Lam and Bremhorst (1981) turbulence model was used as a base, low-Reynolds number model. The modification he introduces power-law index in damping function. The data he published comprises velocity profiles, in physical coordinates though, Moody diagrams and

turbulence kinetic energy profiles. The simulations incorporate axisymmetric boundary conditions on the mesh with 120 radial cells.

3. Escudier and Presti (1999): these experimental data comprise viscoelastic drag reducing fluid. In a laminar shear flow the fluids were well described by a Cross model. The measurements of extensional viscosity have been performed. Reynolds numbers 10^4 - $5\,10^5$ were achieved. Wall coordinate velocity profiles have been published.

4. Pinho (2003): is a presentation of low Reynolds-number model for viscous and viscoelastic non-Newtonian effects. The rheology model used in a study is based on the assumption that viscous and elastic response are both power-law function of shear rate magnitude and displacement magnitude respectively. Nagano and Hishida (1987) model was used as a base. Profiles of velocity, turbulence kinetic energy, dissipation and molecular viscosity were plotted in wall-coordinates.

5. Rudman et al. (2004), and Rudman and Blackburn (2006): direct numerical Simulations undertaken in these study used power-law and Herschel–Bulkley fluid. To facilitate the development of transitionally invariant flow the periodic boundary conditions were imposed on inlet and outlet. The Reynolds numbers, based on wall viscosity, were around 5-7 10^4. DNS calculations allowed to publish an extensive survey of various results spanning velocity/viscosity profiles, turbulence kinetic energy, dissipation, Reynolds's stresses etc.

6. Escudier et al. (2005): experimental data of reporting the profiles of fully developed turbulent flows. The pipeline cross-section had 100mm of internal diameter. The measurements were taken 12m from the inlet. Flow regimes spanned laminar, turbulent and transitional regimes. In case of the latter one the axisymmetric velocity profiles have been reported. The kinds of fluids span Newtonian, Carreau-Yasuda fluids, Herschel–Bulkley fluids.

7. Rhyne (2010): is a set of tables describing two-phase flows in a pipeline under varying pressure drops and inclinations. Tables have been supplemented with films showing the flow regimes.

8. Akai et al. (1980): experimental data describing the co-current flow of air and mercury flow in a square channel. The channel was 18mm high and 48mm wide. The distance between the inlet section and the measurement devices was 3m. The reported results comprised flow rates and corresponding pressure gradients, velocity profiles as well as the profiles of turbulent kinetic energy in both gas and liquid phases.

9. Bruno (1988): the original thesis has not been obtained, but the data set extracted from Smith et al. (2010) was used instead. It contains sixteen different pairs of liquid and gas Reynolds number and their corresponding pressure gradients. This is shown in Table D.2

Most of the above data have been obtained by the means of private correspondence or directly from the publication through a specialised data extraction tools. Obviously, when the private correspondence has been involved the data came in many different forms (consult the Table D.1).
To extract the data from published graphs a program g3data (see Frantz (2008)) was used. It is an open source software for Linux system that allows a user to import a graph, define the frame of reference, read the coordinates of any point, and export the values to a CSV file. Additionally a magnifying tool is provided to facilitate an accurate extraction of points.

Table D.2: Bruno (1988) 1“ channel data

Re_G	Re_L	Pressure gradient [Pa/m]
11000	745	26.2
10050	745	20.5
9000	745	19.0
7670	745	13.9
6100	745	9.7
4750	745	6.4
11000	255	18.7
10050	255	16.3
9000	255	12.6
7670	255	9.1
6100	255	6.5
4750	255	4.3

Table D.3: Flow values and rheology of used data sets

Source	Pressure gradient [Pa/m]	Bulk velocity [m/s]	Consistency index [$m^2 s^{n-2}$]	Power-law index	Yield stress [Pa]
Pinho (2003)	0.99	3.38	2.5e-05	0.8	
	0.17	1.56	2.5e-05	0.6	-
	0.09	1.35	5.0e-05	0.4	
Rudman et al. (2004)	12.22	1.0	4.23e-01	0.6	0.28
	10.044	1.0	2.95e-01	0.6	0.85
	12.871	1.0	3.32e-01	0.75	-
Escudier et al. (2005)	-	0.360 - 0.61	0.001	0	0
	-	0.0398 - 0.258	0.0082	0	0
	-	0.53 - 2.03	2.5e-05	0.53	4.42
	-	2.0 - 3.34	2.31	0.51	9.8
	-	2.25 - 8.58	3.64	0.423	2.39